

JOURNAL OF NUCLEAR MATERIALS

A JOURNAL ON METALLURGY, CERAMICS AND SOLID
STATE PHYSICS IN THE NUCLEAR ENERGY INDUSTRY

EDITORS:

R. W. CAHN — BIRMINGHAM, ENGLAND
J. P. HOWE — CANOGA PARK, U.S.A. — P. LACOMBE — PARIS, FRANCE

CONTENTS

J. J. STOBO, Alpha-beta cycling of uranium	97
B. E. SCHANER, Metallographic determination of the UO_2 - U_4O_9 phase diagram	110
D. S. EVANS, G. V. RAYNOR and R. T. WEINER, The lattice spacings of thorium-lanthanum alloys.	121
R. M. BERMAN, M. L. BLEIBERG and W. YENISCAVICH, Fission fragment damage to crystal structures	129
LOWELL T. LLOYD, Recrystallization of deformed alpha-uranium single crystals	141
R. M. WALKER, On the production of displaced atoms by thermal neutrons	147
Mme J. LEHMANN, Processus des transformations dans les alliages uranium-molybdène de faibles teneurs en molybdène	152
D. W. AYLMORE, S. J. GREGG and W. B. JEPSON, The high temperature oxidation of beryllium. Part I. In dry oxygen	169

Letters to the Editors — Lettres aux Rédacteurs

C. Y. ANG and E. W. BURKHAMMER, Sintering of high density uranium dioxide bodies.	176
A. PORTNOFF-PORNEUF, Aspects fractographiques du bioxyde d'uranium fritté.	181
A. PORTNOFF-PORNEUF, Clivage du bioxyde d'uranium.	186
R. G. ROBINS, Growth habit of electrodeposited uranium dioxide single crystals	189
W. S. BLACKBURN, α - β thermal cycling of uranium	191
A. BEL, R. DELMAS et B. FRANÇOIS, Le frittage des oxydes d'uranium	192
K. A. PEAKALL and J. E. ANTILL, Oxidation of uranium dioxide in air at 350-1000° C.	194
Book Review	196



NORTH-HOLLAND PUBLISHING COMPANY — AMSTERDAM

EDITORIAL ADVISORY BOARD -- CONSEIL DES REDACTEURS

S. AAS (Kjeller, Norway)
 K. F. ALDER (Lucas Heights, Australia)
 P. ALBERT (Vitry, France)
 G. W. ARDLEY (Whetstone, U.K.)
 J. E. BURKE (Schenectady, U.S.A.)
 R. CAILLAT (Saclay, France)
 G. CHAUDRON (Vitry, France)
 H. CHISWIK (Argonne, U.S.A.)
 A. T. CHURCHMAN (London, U.K.)
 A. S. COFFINBERY (Los Alamos, U.S.A.)
 A. H. COTTRELL (Cambridge, U.K.)
 R. L. CUNNINGHAM (Ottawa, Canada)
 C. DECROLY (Bruxelles, Belgium)
 M. D'HONT (Mol, Belgium)
 J. D. FAST (Eindhoven, Netherlands)
 H. M. FINNISTON (Newcastle, U.K.)
 J. FRIEDEL (Paris, France)

E. GEBHARDT (Stuttgart, Germany)
 G. B. GREENOUGH (Windscale, U.K.)
 E. GRISON (Saclay, France)
 B. R. HASIGUTI (Tokyo, Japan)
 J. HERENGUEL (Antony, France)
 L. K. JETTER (Oak Ridge, U.S.A.)
 B. KIESSLING (Stockholm, Sweden)
 K. LÜCKE (Aachen, Germany)
 B. LUSTMAN (Pittsburgh, U.S.A.)
 R. MADDIN (Philadelphia, U.S.A.)
 A. MERLINI (Milan, Italy)
 P. MURRAY (Harwell, U.K.)
 R. MYERS (Sydney, Australia)
 J. A. L. ROBERTSON (Chalk River, Canada)
 J. A. SABATO (Buenos Aires, Argentina)
 K. TANGBI (Bombay, India)
 P. VACHET (Paris, France)

Papers or letters should be sent to one of the Editors,

R. W. CAHN (Dept. of Metallurgy, University of Birmingham, Birmingham 15, England).
 J. P. HOWE (Atomics International, P.O. Box 309, Canoga Park, California, U.S.A.).
 P. LACOMBE (Centre de Recherches Métallurgiques de l'Ecole des Mines, Blvd. St. Michel 60, Paris VI, France)

either directly or through a member of the Editorial Advisory Board.

Papers or letters should be written in English, French or German; papers should have a summary in the appropriate language. Translations of the summary into the two other languages will be added by the Editors.

Instructions to contributors will be found in Vol. 1, No. 1 (pp. 111-112).

Books for review should be sent to one of the Editors.

The Journal of Nuclear Materials will initially be published quarterly.

The subscription price of a volume of 360 pages is \$ 18.00, 130 s., Gld. 68.50 per volume, post-free.

Subscriptions should be sent to the publishers, North-Holland Publishing Company, P.O. Box 103, Amsterdam or to any subscription-agent.

No part of this issue may be reproduced in any form, by print, photoprint, microfilm or any other means without written permission from the publisher. Reprints, photoprints or microfilms are obtainable at cost from the publisher.

Les articles ou les lettres devront être envoyés à un des Rédacteurs-en-chef,

R. W. CAHN (Dept. of Metallurgy, University of Birmingham, Birmingham 15, England).
 J. P. HOWE (Atomics International, P.O. Box 309, Canoga Park, California, U.S.A.).
 P. LACOMBE (Centre de Recherches Métallurgiques de l'Ecole des Mines, 60 Bd. St. Michel, Paris VI, France)

ou directement ou par un membre du Conseil des Rédacteurs.

Les articles ou les lettres devront être rédigés en anglais, français ou allemand, les articles avec un résumé dans la langue correspondante. Les traductions du résumé dans les deux autres langues seront ajoutées par les éditeurs.

Les instructions aux auteurs se trouvent dans le Vol. 1, No. 2 (pp. 211-212).

Les Livres (exemplaires de presse) devront être envoyés à un des Rédacteurs-en-chef.

Le Journal des Matériaux Nucléaires paraîtra initialement tous les trois mois.

Prix de souscription par volume d'environ 360 pages: \$ 18.00, 130 s., Gld. 68.50, franco.

Les abonnements devront être envoyés aux éditeurs, North-Holland Publishing Company, P.O. Box 103, Amsterdam, ou à votre librairie.

ALPHA-BETA CYCLING OF URANIUM

J. J. STOBO

C. A. Parsons and Co. Ltd., Nuclear Research Centre, Fossway, Newcastle-upon-Tyne, UK

Received 11 January 1960

Experiments on the alpha-beta cycling of the core of a bar of uranium while the rim remains in the alpha phase show that dimensional distortions of the bar occur when more than about 10 % of the bar diameter is transformed to beta. The extent of the damage depends on the fraction of the bar diameter transformed (e.g. +0.5 % diameter strain with 30 % transformed). Damage is not observed to increase with increasing number of cycles between 13 and 100.

Tubular specimens suffer more severe damage than solid bars when compared on a basis of the percentage of outside diameter transformed. The striking feature of these results is the large increase in internal diameter.

The distortions are dependent on the direction of movement of the interface between the phases, and the detailed results are consistent with a general model of phase-change cycling.

Metallographic examination after cycling shows that recrystallisation has taken place in all metal heated to above $560 \pm 10^\circ \text{C}$. No porosity which can be attributed to cycling has been detected.

Des expériences de cyclage $\alpha \rightarrow \beta$ sur un barreau d'uranium ont été réalisées de telle sorte que le cœur du barreau subisse seul le cyclage $\alpha \rightarrow \beta$ tandis que la périphérie reste en phase α . Des modifications de dimension du barreau se produisent quand le cyclage $\alpha \rightarrow \beta$ intéresse plus de 10 % du diamètre du barreau. L'importance du dommage dépend de la fraction du diamètre du barreau transformé (par exemple 30 % transformé provoque un allongement de diamètre de 0,5 %). On n'observe pas d'augmentation du dommage avec le nombre croissant de cycles entre 13 et 100 cycles.

Des échantillons tubulaires subissent une distorsion plus sévère que les barreaux pleins quand on compare ces deux types de barreaux en se basant sur le pourcentage du diamètre extérieur modifié.

Les distorsions dépendent de la direction de déplacement de l'interface entre les phases; les résultats détaillés sont conformes à un mode général de cyclage par changement de phase.

L'examen métallographique après cyclage montre que la recrystallisation a eu lieu dans toute la région du métal qui a été chauffée au-dessus de $560 \pm 10^\circ \text{C}$. Aucune porosité, qui pourrait être attribuable au cyclage, n'a été observé.

Es wurden Versuche zur zyklischen $\alpha \rightarrow \beta$ -Umwandlung des Kerns eines Uranstabes durchgeführt, wobei der Mantel des Stabs in der α -Phase verblieb. Dabei zeigten sich Änderungen der Stababmessungen, wenn die Umwandlung in die β -Phase in einem Bereich von mehr als 10 % des Stabdurchmessers ablief. Der Grad der Schädigung ist von dem Bruchteil des umgewandelten Stabvolumens abhängig (z.B. Umwandlung über 30 % des Durchmessers ergibt +0,5 % Zunahme des Durchmessers). Eine Zunahme der Schädigung wurde mit wachsender Zyklenzahl von 13 auf 100 nicht beobachtet.

Rohrförmige Proben erleiden bei einem Vergleich, bei dem der von der Umwandlung betroffene Prozentsatz des äusseren Durchmessers zugrunde gelegt wird, eine grössere Schädigung als massive Stäbe. Das auffallendste Merkmal dieser Ergebnisse ist die starke Zunahme des Innendurchmessers.

Die Gestaltsänderungen hängen von der Bewegungsrichtung der Phasengrenzfläche ab. Die Einzelbefunde stimmen überein mit einer allgemeinen Form der zyklischen Phasenumwandlung. Eine nach der zyklischen Wärmebehandlung vorgenommene metallographische Untersuchung ergab, dass an allen Stellen, die über $560 \pm 10^\circ \text{C}$ aufgeheizt wurden, eine Rekristallisation stattgefunden hat. Es konnte keine von der zyklischen Wärmebehandlung herrührende Porosität festgestellt werden.

1. Introduction

Permanent dimensional changes and distortions result when uranium and several other metals, notably iron, are cycled through their

phase changes^{1,2,3}). At 662°C uranium transforms from the alpha to the beta phase and therefore this has set the limit on the maximum fuel temperature in civil reactors to avoid

possible damage from cycling through the phase change. If a central core of beta could be tolerated in a fuel element, considerable gain in heat rating and efficiency would be possible.

This report discusses the quantitative effects of thermally cycling the central core of a uranium bar or tube through the alpha-beta transformation while the rim remains in the alpha phase. The experiments could not simulate the effects of irradiation although fission product accumulation leading to swelling or embrittlement (e.g., hot shortness) will be important for reactor service at these temperatures and could be affected (probably adversely) by a phase transition.

2. Discussion of Previous Work

Buckley *et al.*¹⁾ demonstrated experimentally that, when a plane phase boundary moves through a uranium specimen, there is a shape change characterised by shortening of the specimen normal to the boundary separating alpha from beta, and a lengthening normal to the boundary when it separates beta and gamma.

Lehr²⁾ and De Jong and Rathenau³⁾ reported a similar phenomenon in the alpha-gamma cycling of pure iron; in this case, however, the specimens grow in length normal to the phase boundary.

The explanations offered by these authors are similar and assume that:

- (1) there is coherency at the phase boundary;
- (2) to maintain this coherency in the face of the transformation stresses, there is plastic flow on both sides of the phase boundary, and this deformation occurs to a greater extent in the weaker phase.

The mechanism for alpha-beta cycling damage in uranium, as described by Buckley *et al.*, is shown schematically in fig. 1. Alpha is weaker and has 1 % lower specific volume than beta at the transformation temperature. The alpha phase, adjacent to the coherent interface, is plastically deformed to give axial shortening and an increase in radius of the specimen; this is the most marked result of cycling. During the

heating part of the cycle, there is also a tendency for the advancing beta phase to expand the adjacent alpha in the plane of the phase boundary and so lead to the development of a tapered specimen. This is a secondary effect which has been exaggerated in fig. 1, but which has been established experimentally⁴⁾.

In the cases of the beta-gamma transformation in uranium and the alpha-gamma transformation in iron, there is lengthening of a specimen normal to the phase boundary. It is known that beta uranium is much stronger than gamma, and Lehr²⁾ has suggested that, in pure iron, gamma is stronger than alpha at the transformation temperature.

These properties are tabulated in table 1.

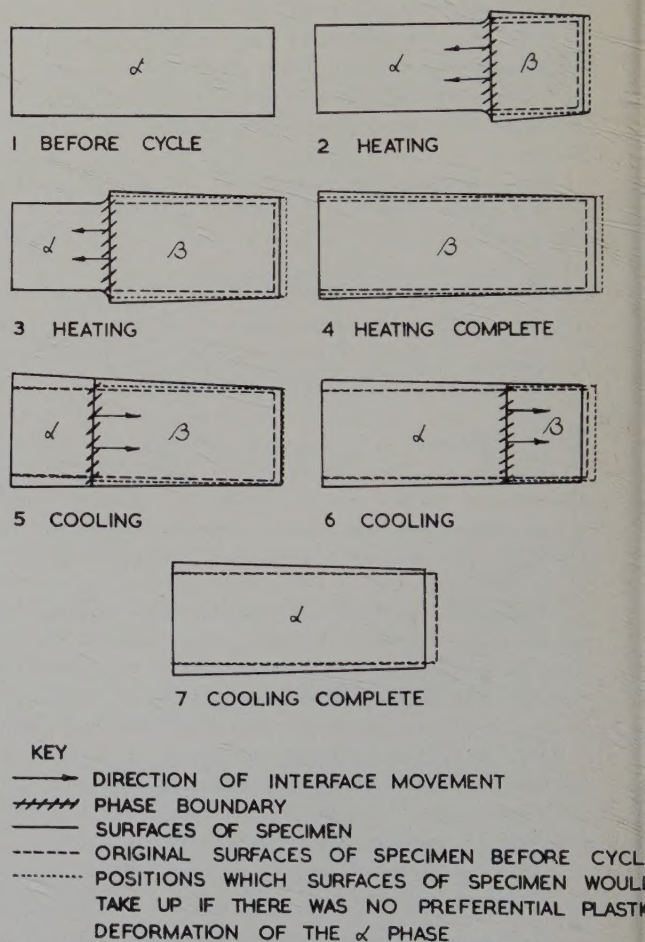


Fig. 1. α - β cycling damage mechanism for a plane interface.

TABLE 1

Metal	Uranium		Uranium		Iron	
Phase	α	β	β	γ	α	γ
Relative strength at transformation temperature	Low	High	High	Low	Low	High
Relative specific volume at transformation temperature	Low	High	Low	High	High	Low
Effect of phase-change cycling on dimension normal to phase boundary	Shortening		Lengthening		Lengthening	

In these three cases, a combination in one phase of high strength and high specific volume gives distortion of one sign, and high strength with low specific volume leads to distortion of the other sign. The following general statement of the effect is suggested as applicable to all such cases. When a phase boundary moves through a specimen there is a tendency for the specimen to retain the dimensions of the stronger phase in directions tangential to the boundary. This tendency can be expected to increase with increasing volume change on transformation and with increasing difference in strength.

McIntosh and Heal⁵⁾ reported results on the cycling of various uranium alloys and showed that $\frac{1}{2}$ at % Cr and 4 at % Mo confer considerable resistance to damage. They attribute this to the smaller difference in mechanical properties between alpha and beta in these alloys than in the nominally pure, magnesium-reduced uranium.

Buckley *et al.*¹⁾ estimate that under reactor conditions there is little chance of cycling damage when the beta phase core inside a uranium bar occupies less than 20 % of the diameter; beyond this, they calculate that the stress will be sufficient to make the alpha rim fully plastic. They also predict that cumulative cycling damage is unlikely until the phase boundary reaches the surface.

3. Experimental Method

In the experiments on solid bars, specimens 71 cm long and 2.35 or 2.44 cm diameter were machined from magnesium-reduced uranium which had been beta-quenched and alpha-

annealed. Circumferential grooves were scribed at accurate intervals of 5 cm along the specimens. These were used as markers for length measurements before and after cycling.

A 5 cm length at each end was copper plated for electrical contact purposes and the specimens were thermally insulated by winding with woven silica tape. A 0.3 mm thickness of tape was put on the 2.44 cm diameter bars for the high heat flux (46 kW/m or ~ 14 kW/ft) and a 0.6 mm thickness on the 2.55 cm diameter bars for the low heat flux experiments (20 kW/m or 6 kW/ft). The bars, with their silica tape wrappings, were canned in 66 cm long, 0.127 mm thick, 2.5 cm nominal bore, stainless-steel tubes. Hollow copper end connections were then fixed by filling them with molten lead and inserting the copper plated ends of the uranium bar. Three thermocouple holes were drilled through the can and into the bar by spark erosion and 0.16 cm diameter Pyrotenax chromel-alumel thermocouples inserted and brazed to the can in the arrangement shown in fig. 2(a). Thermocouples 1 and 2 were on the same cross-section, No. 1 being at the centre of the bar and No. 2 at a depth of $\frac{1}{3}$ of the radius from the surface. The axial position of No. 3 thermocouple was varied between 5 cm and 23 cm from the centre in various experiments to measure the length of the beta core.

Tubes for argon inlet and outlet were brazed to the can, one at each end; during the experiments a small flow of argon was maintained to prevent oxidation and indicate leaks.

The whole assembly (fig. 2(a)) was connected to flexible bus bars from a continuously variable

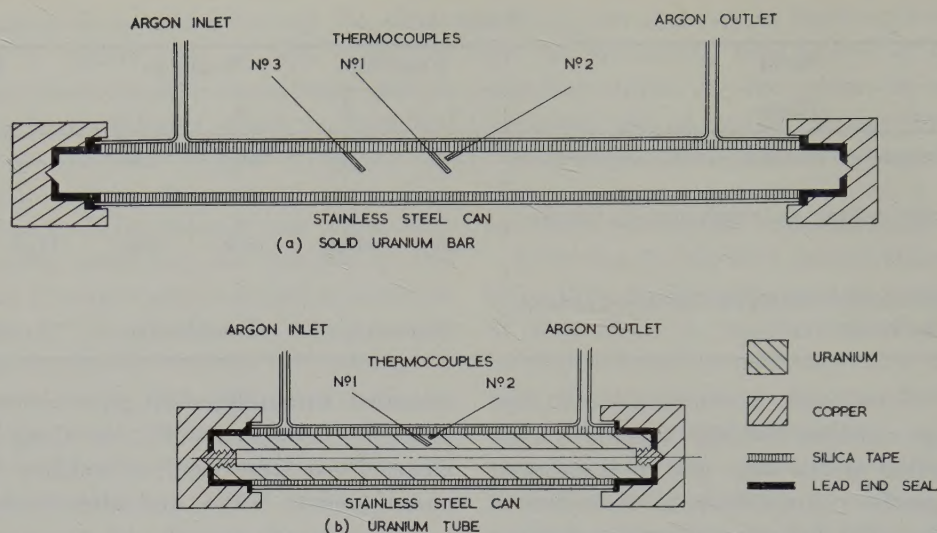


Fig. 2. Experimental arrangements.

high current, low voltage rectifier, the canned uranium being placed horizontally in a tank of water which was lightly stirred by compressed air.

In all tests, heating and cooling rates were $30^\circ \pm 5^\circ \text{C}$ per minute. Cycles were from a starting temperature of 600°C (No. 1 thermocouple) for unalloyed uranium and 500°C for the one specimen of $\frac{1}{2}$ at % Cr.

During testing, the temperature of the central thermocouple (No. 1) was continuously record-

ed; by operating a selector switch, spot readings of temperature from the other thermocouples were obtained on the same trace from time to time.

Experiments on tubular specimens, cooled only on the outside, were done using the arrangement shown in fig. 2(b). Only two thermocouples were used since a 30 cm long test specimen was the biggest available. Care was taken that No. 1 thermocouple hole penetrated

TABLE 2
Conditions and some results of the experiments

Expt. No.	Temperature range ($^\circ \text{C}$)	No. of cycles	Heat flux (kW/m)	Overall change in length (cm)	Increase in bow at centre (cm)	Remarks
4	600-700	100	20	+ 0.254	1.810	
7	600-680	100	20	- 0.127	0.725	
10	600-700	23	20	- 0.175	0.406	
11	600-720	33	20	+ 0.503	0.450	
12	600-680	50	20	- 0.127	0.546	
13	600-710	13	20	- 0.132	0.650	
19	600-700	50	20	- 0.254	1.580	
22	600-700	23	46	- 0.175	0.626	
23	600-700	25	46	- 0.444	1.145	
25	600-680	52	46	- 0.132	1.460	
17	600-700	50	16	- 0.051	—	Tube
20	600-700	50	16	+ 0.038	—	Tube
24	600-700	50	39	- 0.127	—	Tube
15	500-700	16	20	- 0.975	0.330	$\frac{1}{2}$ at % Cr

to the bore of the tube; thus the argon pressure inside was maintained at one atmosphere.

In all experiments there was an initial clearance of 0.25 mm between the silica insulation and the can.

In some of the experiments, water leaked in through the brazed joints, the lead end seals or through cracks caused by wrinkling of the stainless steel can. The experiment was stopped when this was observed but in none of the experiments reported here was oxidation of the uranium severe enough to affect the results.

4. Results

The conditions and some results of the experiments are shown in table 2.

In the low heat flux experiments with solid uranium bars, a radial temperature difference of 45° C was maintained. This figure was derived from the readings of the two thermocouples on the central cross-section (one at the centre and one at $\frac{1}{3}$ of the radius from the surface), assuming a parabolic relationship between temperature and radial position; this is approximately correct for this case of uniform heat generation⁶). A 45° C radial drop corresponds to 20 kW/m (6 kW/ft) in uranium and implies that the following were the percentages of diameter above 670° C in the various experiments (table 3).

TABLE 3

Max. temperature of cycle in centre of bar, (° C)	Percentage of bar diameter above 670° C at 20 kW/m (6 kW/ft)
680	47
700	82
710	94
720	100

The temperature of the alpha to beta transformation as observed from arrests varied between 665° C and 675° C in different tests; hence the choice of 670° C in table 3. The tabulated figures in the right hand column can be taken as approximations for the diameter of the beta core. When the uncertainty due to the

latent heat of transformation is considered, their accuracy, as amounts transformed is estimated at $\pm 10\%$ of the bar diameter.

The length of the beta core was estimated to be between 30 cm and 40 cm in the 20 kW/m experiments; this estimate was made from the readings of No. 3 thermocouple situated 5, 15, 18 and 23 cm from the centre of the bar in four different experiments (Nos. 11, 12, 13 and 19).

In the high heat flux experiments (those with 0.3 mm of silica insulation), a radial temperature difference of 100° C was obtained, corresponding to 46 kW/m (14 kW/ft). With 700° C as the maximum temperature on No. 1 thermocouple, 55% of the diameter was above 670° C, while 31% was above 670° C with 680° C as the maximum. The length of the beta core in these experiments was between 38 cm and 48 cm.

Two of the tubular specimens tested were 23 cm long, 2.35 cm o.d. and 0.79 i.d. and were subjected to a heat flux of 16 kW/m; under these conditions a maximum central temperature of 700° C corresponded to 86% of the wall thickness above 670° C. One tubular specimen 30 cm long, 2.44 cm o.d. and 0.71 i.d. was cycled to 700° C at 40 kW/m (12 kW/ft); in this case 58% of the wall thickness was above 670° C.

All the measured diameter and length strains are shown graphically in figs. 3-7. These are accurate to $\pm 0.3\%$ on diameter and $\pm 0.5\%$ on length. Diameter and length measurements after cycling were averaged from four measurements on each section between marker grooves since both wrinkling and bow were caused by cycling.

After cycling, density measurements were made on sections cut at 5 cm intervals along specimens No. 4, 15, 17, 19, 22 and 25. These showed that in no case was there a variation of more than $\pm 1\%$ from the value measured on the complete specimen before cycling.

5. Metallographic Results

Specimens from all experimental bars were examined metallographically before and after cycling; after cycling specimens were cut from the centres of the bars. Grain sizes, determined

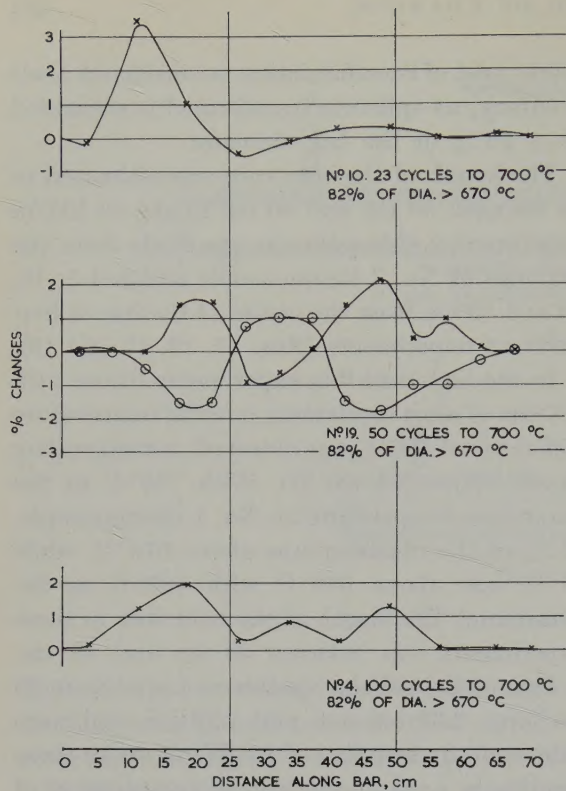


Fig. 3. Diameter and length changes in solid bars at 20 kW/m.

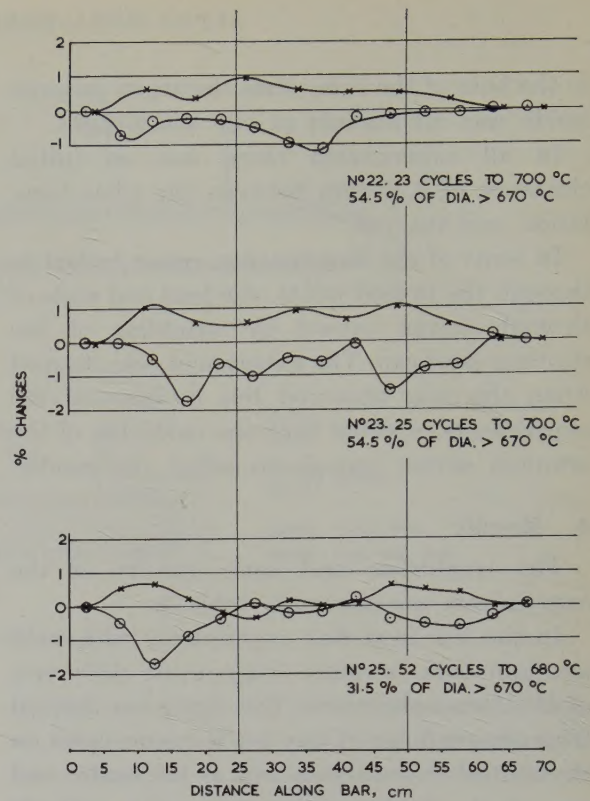


Fig. 5. Diameter and length changes in solid bars at 46 kW/m.

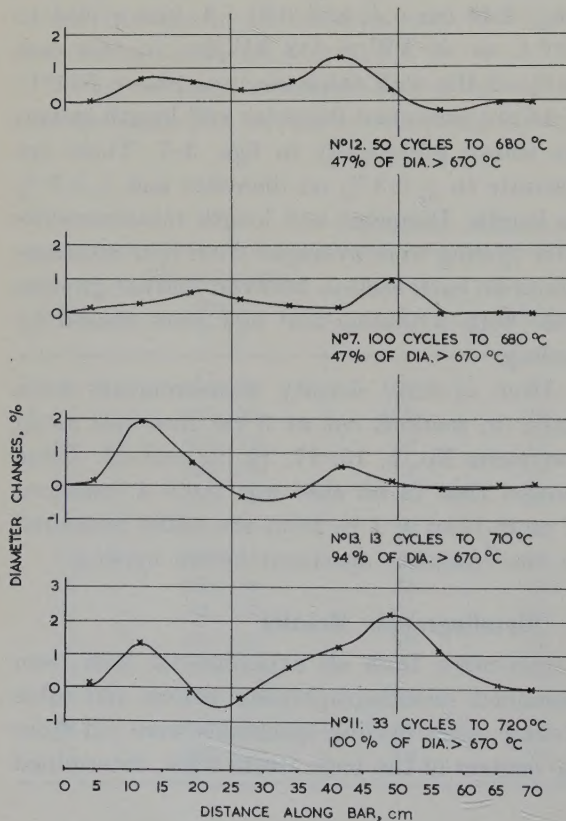


Fig. 4. Diameter changes in solid bars at 20 kW/m.

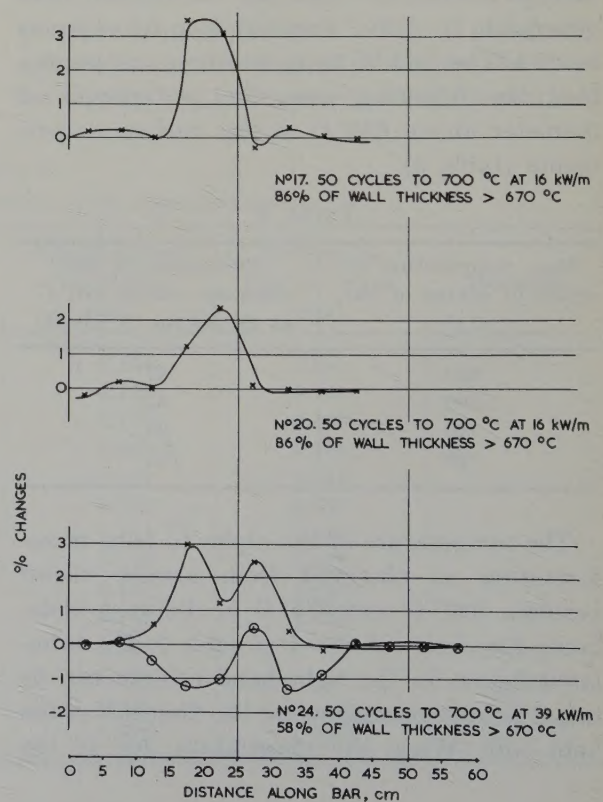


Fig. 6. Diameter and length changes in tubular specimens.

TABLE 4
Effect of cycling on grain size

Expt. No.	Uranium	Grain size, mm								Factor by which average trans- verse grain size changes with cycling
		Before cycling				After cycling				
		Longitudinal section		Transverse section		Longitudinal section		Transverse section		
		Ave.	Max.	Ave.	Max.	Ave.	Max.	Ave.	Max.	
4	Mg-red. β -quenched bar			0.17	0.8			0.30	2.5	Increase by 1.8
7	Mg-red. β -quenched bar			0.17	0.9			0.32	2.2	Increase by 1.9
10	Mg-red. nominally β -quenched but unrefined bar			0.59	5			0.35	3.2	Decrease by 1.7
11	Mg-red. nominally β -quenched but unrefined bar			0.61	5			0.28	2.4	Decrease by 2.2
12	Mg-red. nominally β -quenched but unrefined bar			0.63	5			0.27	2.3	Decrease by 2.3
13	Mg-red. nominally β -quenched but unrefined bar			0.59	5			0.30	2.8	Decrease by 2.0
19	Mg-red. β -quenched bar	0.28	0.9	0.22	0.9	1.0	3.8	1.2	4.4	Increase by 5.4
22	Mg-red. β -quenched bar	0.25	0.8	0.21	0.8	0.44	1.9	0.30	3.3	Increase by 1.4
23	Mg-red. β -quenched bar	0.17	0.7	0.16	0.7	0.28	1.0	0.38	5.4	Increase by 2.4
25	Mg-red. β -quenched bar	0.21	0.7	0.23	1.2	0.54	3.1	0.57	4.6	Increase by 2.5
17	Mg-red. β -quenched tube	0.25	0.6	0.26	0.9	0.46	1.5	0.27	2.3	No change
20	Unrefined tube	0.95	5.0	1.1	5.6	0.62	3.1	0.44	4.1	Decrease by 2.4
24	As-cast tube	0.80	5.5	0.85	6.0	0.38	5.0	0.46	6.6	Decrease by 1.8
15	As-cast $\frac{1}{2}$ at % Cr bar			0.23	0.5	0.17	0.6	0.17	0.9	Decrease by 1.3

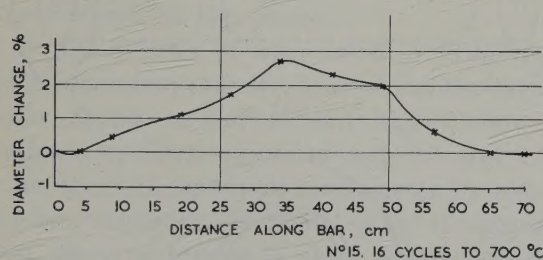


Fig. 7. Diameter changes of $\frac{1}{2}$ at % Cr alloy bar at 20 kW/m.

by the line intercept method, are reported in table 4. In none of these central sections was there a difference in metallographic structure between the rim and the core of the bar after cycling.

When sections were cut outside the axial limit of the beta core the boundary between regions of different grain size was observed; an example is shown as fig. 8 where the ellipsoidal zone of grain growth is seen adjacent to the beta quenched structure.

Examples of the surface wrinkling noticed after cycling are shown in fig. 9.

No evidence of cavitation or pore formation that could be attributed to cycling was found. Some porosity was observed in all sections but it was not possible to differentiate between casting defects and porosity induced by thermal cycling.

6. General Discussion

Fig. 1 shows how a plane interface can cause the experimentally observed¹⁾ damage. The specimen shortens normal to the interface and expands in the interface. In the present experiments the interface is a closed surface which can be considered approximately as the combination of a cylindrical interface which moves radially and two plane interfaces moving axially.

For a cylindrical interface the model is shown in fig. 10. The tendency is for dimensions in the interface (length and circumference) to be

expanded and for the dimension normal to the interface, the radius, to be contracted. These tendencies are denoted by arrows on fig. 10(a) and can be conveniently called primary tendencies.

Secondary effects, which modify these tendencies, arise when the model is considered further. In these experiments coherency across the phase boundary is sufficient to prevent the formation of voids; (this is supported by the density and metallographic results reported above). Thus circumferential growth cannot occur, as illustrated by fig. 10(b) where a thin annulus is considered to be transforming. For circumferential growth of this annulus both R_1 and R_2 (the i.d. and o.d.) must expand. The inside diameter R_1 cannot expand because of the strength of the beta core and the cohesion across the interface. Therefore since the annulus is plastic its thickness ($R_2 - R_1$) tends to increase rather more than it would if R_1 were free to expand, and its length, normal to the paper in fig. 10(b), tends to expand also. The tendency for circumferential growth is therefore resolved into components of axial and radial growth.

Thus the change in the radial dimension of the specimen is the sum of

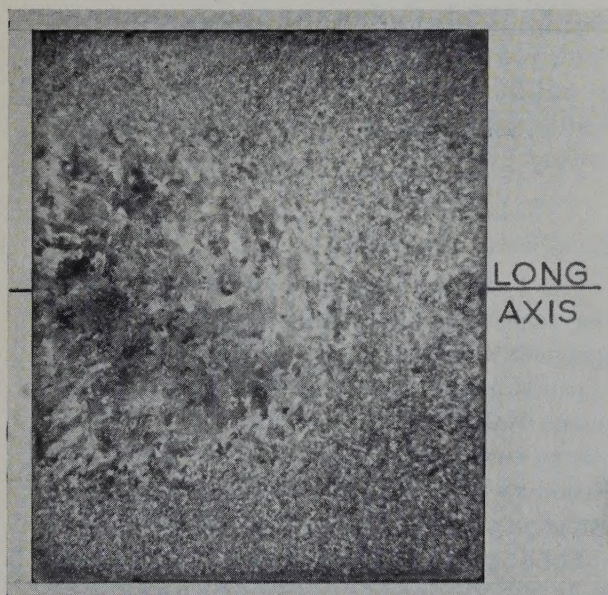


Fig. 8. Grain growth zone in uranium bar specimen.



Fig. 9a

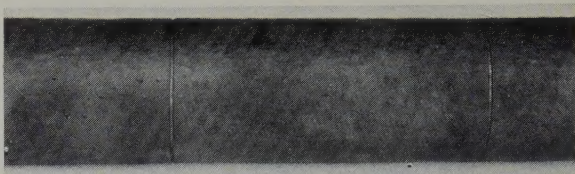
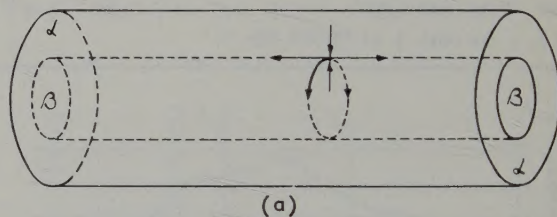


Fig. 9b

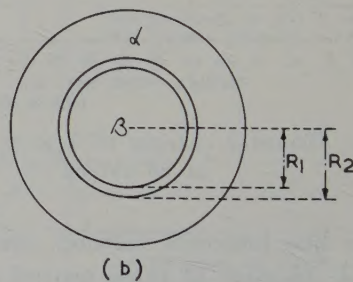


Fig. 9c

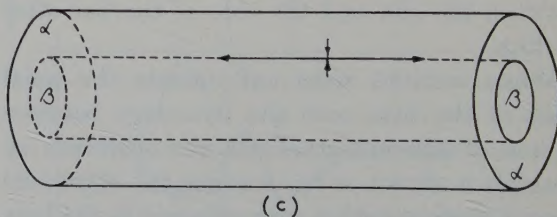
Fig. 9. Effect of cycling on surfaces of solid bars.



(a)



(b)



(c)

Fig. 10. Damage at a cylindrical interface.

- (1) the primary radial contraction normal to the interface, and
- (2) the radial expansion resulting indirectly from the primary tendency to circumferential growth.

The axial growth of the specimen is the sum of

- (1) the primary tendency to axial growth, and
- (2) the contribution to axial growth resulting indirectly from the primary tendency to circumferential growth.

Fig. 10(c) illustrates a possible result of these considerations.

The experimental results will be discussed in the following paragraphs in the light of the models shown in figs. 1 and 10.

7. Solid, Unalloyed Bars at 20 kW/m (6kW/ft)

Figs. 3 and 4 show that there are marked increases in diameter at the ends of the beta core in specimens 4, 7, 10, 11, 12, 13 and 19. Here the interface is approximately a plane moving axially; fig. 1 is appropriate and the results are consistent with its predictions. Specimen 19 (fig. 3) for which length changes are available shows that a decrease in length has occurred in this region.

In the centres of bars where a cylindrical interface moves radially, four of the five specimens cycled to 700° C and higher show a decrease in diameter of between 0.5 and 1 % while the fifth increased in diameter by about the same amount. The model of fig. 10 suggests that diameter strains in these regions are the algebraic sum of two conflicting tendencies which would qualitatively account for this anomaly and would explain why the diameter strains in the centres of the bars are less than those at the extremities of the beta core.

In specimens cycled to 680° C no diameter decrease was observed (fig. 4). This difference, from the specimens taken to 700° C and above, might be due to the following hypothetical sequence of events (illustrated in fig. 11):

(a) On heating, the beta phase forms firstly in "islands" along the length of the bar rather than as one thin fibre. This could be caused by quite small variations in heat transfer along the

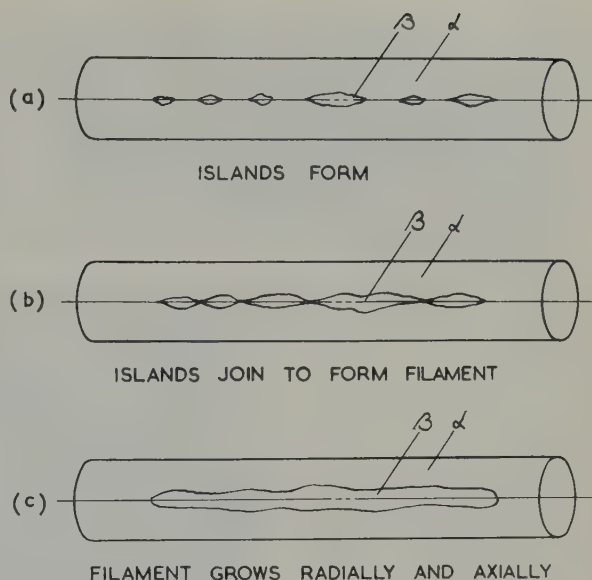


Fig. 11. Suggested model for β -zone growth with heat transfer irregularities.

can; thermocouple entries, in these experiments, are examples of likely sources of variation.

(b) The early growth of beta is by the joining up of these islands to form a core. At this stage the interface is moving axially as well as radially in the centre of the bar.

(c) When the beta forms a continuous core it grows radially in the centre and axially at the ends.

The reverse sequence would be expected on cooling.

It is proposed that in the 680° C experiments (Nos. 7 and 12, fig. 4) with about 50 % of the diameter being beta, the (a) and (b) steps of this sequence are predominant, giving diametral expansions by the mechanism of fig. 1, while in the other experiments, with more than 80 % of the beta formed, step (c) is predominant in its effect on shape changes by the mechanism of fig. 10.

In none of these experiments were sufficient thermocouples installed to detect this phenomenon. Its occurrence would, of course, affect all these experiments and would contribute to the lessening of strains in the centres of bars compared to those at the extremities of the beta cores.

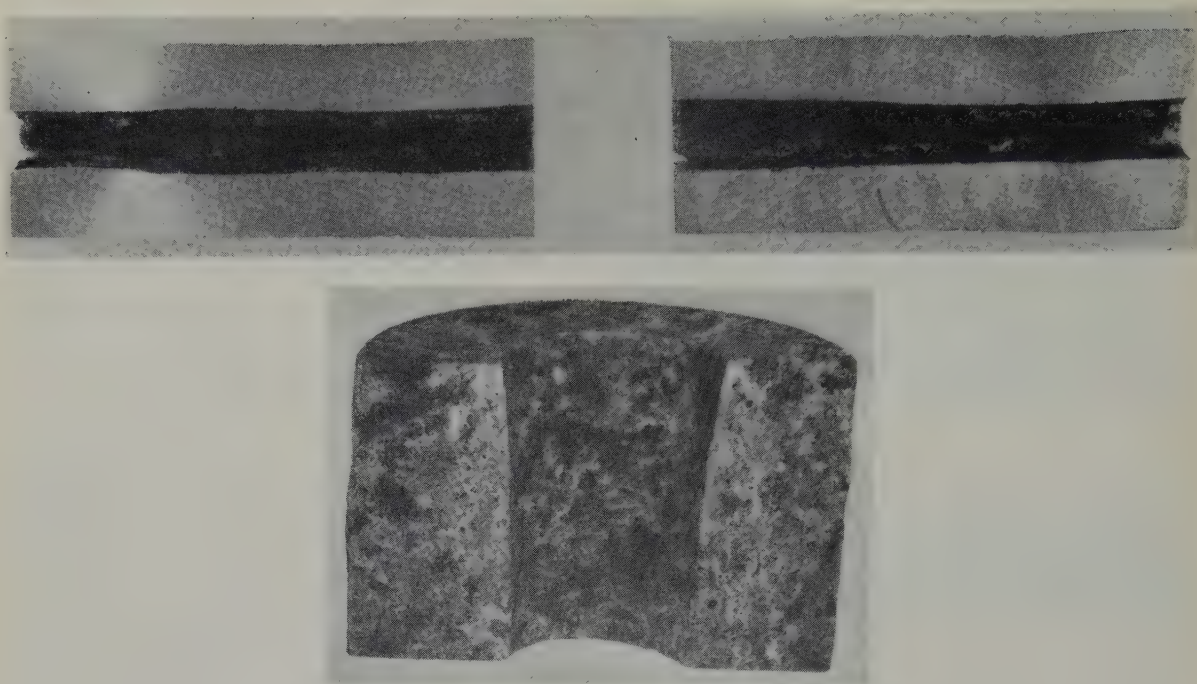


Fig. 12. Swelling of bores in tubular specimens.

The results do not show that an increasing number of cycles leads to more severe damage.

At 20 kW/m an increase in the amount of beta phase present from 47 % to 82 % of the diameter has caused a change in maximum diameter strain from 1 % to 2-3 %.

8. Solid Unalloyed Bars at 46 kW/m (14kW/ft)

Considered together with the 20 kW/m experiments, these specimens show (fig. 5) broadly the same type and amount of damage for the same fraction of diameter transformed to beta. This can be seen by comparing the results of Specimens 22 and 23 on fig. 5 with those of Specimens 7 and 12 on fig. 4, all of which had about 50 % of their diameter transformed to beta.

However, there are some differences in detail between the two sets of results. In the cases of higher heat flux, the beta cores were 7.5 cm longer than in the 20 kW/m experiments and consequently the axial damage zones are longer. Also, the axial temperature gradient from the end of the beta core to the terminal block was

steeper in the higher heat flux experiments; this has led to less axial movement of the interface at the ends and has given less prominent bulges in diameter at these points. Wrinkling of the surface was generally less marked at the higher heat flux as shown in figs. 9(a) and (b) but this is attributed to the smaller fraction of diameter transformed in the 46 kW/m experiment (fig. 9(b)) rather than to the higher heat flux directly.

When the results of the 20 kW/m and 46 kW/m experiments are considered together, an approximate relationship can be established between damage measured by the maximum diametral strain, and fraction of diameter transformed. This relationship is shown graphically in fig. 13. An extrapolation indicates that no damage would be expected when 10 % of the diameter is transformed to beta. This is in reasonable agreement with the 20 % derived theoretically by Buckley *et al.*¹⁾

It is important to note that if at 46 kW/m, the maximum uranium temperature is only 1° C above the transformation temperature, 10 % of the diameter is transformed to beta.

9. Tubular, Unalloyed Specimens

Two 23 cm specimens, Nos. 17 and 20, were cycled to 700° C at 16 kW/m so that 86 % of the wall thickness (or 90 % of the outside diameter) was above 670° C. The length of the beta core was between 6.5 cm and 9 cm. A 30 cm tubular specimen (No. 24) was cycled to 700° C at 39 kW/m so that 58 % of the wall thickness (or 70 % of the outside diameter) was above 670° C; here the beta core was between 13 and 18 cm long. The diametral strains (and length strains for Specimen 24) are shown in fig. 6. On sectioning, these specimens were found to have bores swollen between 20 % and 30 %. Examples are shown in fig. 12.

The mechanism of the swelling of the bores of the tubes is simply obtained by applying the model of fig. 1 to the special case of a hollow rod. The plane, annular interface moves axially and the specimen is therefore expanded in i.d. and o.d. and contracted axially. For the cylindrical interface moving radially in the centre of the specimen, the mechanism predicts contraction of the i.d. and of the o.d. and axial expansion.

The results for Specimens 17 and 20 are explained on this mechanism if it is assumed that the extreme shortness of the beta core (6.5–9 cm) has led to predominantly axial movement of the interface in these experiments. In specimen 24 the longer beta core (13–18 cm) has allowed some axial lengthening in the centre and a marked decrease in the amount of diameter strain (fig. 6). Thus there is a tendency towards a decrease in diameter at the centres of the specimens and the prediction that contractions of o.d. and i.d. would occur in longer specimens is the logical extension of the argument.

A comparison of the results on tubular specimens with those on solid rods indicates a tendency to greater damage (as measured on o.d.) as a result of the central hole. This is demonstrated on fig. 13 where the results for tubes are shown plotted on the same basis as those for solid rods; the percentage of the o.d. inside the 670° C isotherm is the ordinate for

both cases. While one solid rod experiment shows an anomalously large damage, in the remainder of the experiments the tubes have suffered more severely. The reason for this is not understood.

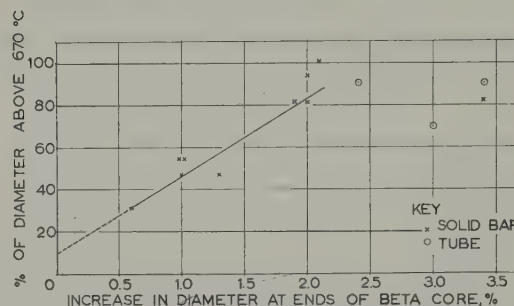


Fig. 13. Data for unalloyed specimens.

10. Uranium, $\frac{1}{2}$ at % Chromium Alloy Bar

Specimen 15 in the as-cast condition was given 16 cycles to 700° C at 20 kW/m. This corresponds to 100 % of the diameter being above 640° C, the beginning of the transformation range, and to 90 % above 660° C, the end of the range. At the cooling rate of 30° C per minute the transformation from beta to alpha was not observed as an arrest until 560° C. This is in keeping with the known T.T.T. characteristics of the alloy ⁷) and, because of it, 500° C was chosen as the lowest temperature of cycling. The diameter changes of the specimen after cycling are shown on fig. 7; the overall length of the bar decreased by 1 cm in 16 cycles which represents 2.8 % of the length of the beta core.

McIntosh and Heal ⁵) have observed the equality in strengths of the alpha and beta phases in this alloy at the transformation temperature. Because of this the transformation of the core of a bar to beta on heating should be accomplished with isotropic expansion with none of the effects associated with different strengths on each side of the boundary such as are suggested in fig. 1. This has probably happened in Specimen 15 as shown in fig. 7. At the lower transformation temperature (560° C) no data on relative strengths exist. The behaviour of this specimen can be explained by

assuming that at this temperature the alpha phase is stronger than the beta. If this is so, when the cooling transformation begins there will be a contraction in the specimen dimensions which are tangential to the interface and therefore a net expansion at right angles to these directions. Fig. 14 shows sketches of the stages of this process.

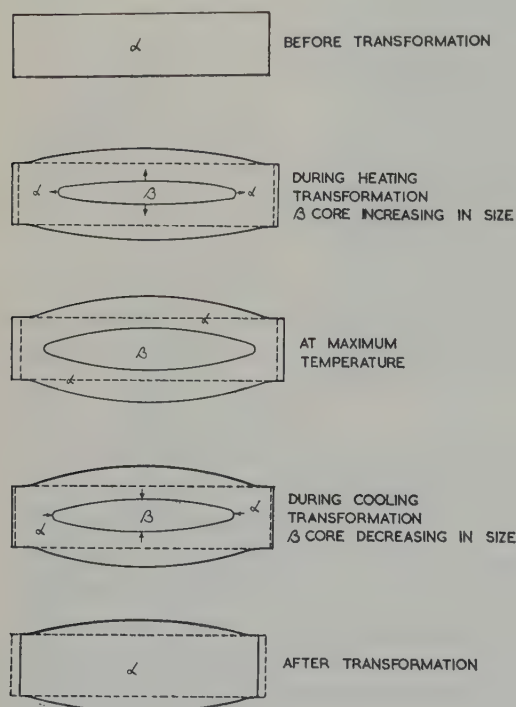


Fig. 14. Suggested model for cycling damage in a $U\text{-}\frac{1}{2}$ at % Cr alloy.

Thus, assuming that at 560°C the alpha is the stronger phase, the observed result is consistent with the general model of phase-change cycling damage. The result can be summarised as a tendency to retain the diameter at the maximum temperature by means of a large decrease in length on cooling.

Cooling rate would be expected to have an effect on the damage sustained by this alloy since the temperature of cooling transformation will be sensitive to cooling rate and, at different temperatures, the strength of the beta relative to the alpha may well be different.

11. Metallographic Discussion

The main metallographic feature in all the unalloyed specimens was a change in grain size (table 4). This was observed as an increase of between 1.4 and 5.4 times for the specimens grain refined by beta quenching while for as-cast and incompletely grain refined metal the grain size was approximately halved by cycling.

In the centres of the specimens there was no evidence of a rim and core of different grain size but such sections, one of which is shown as fig. 8, were found outside the axial beta core limits. This suggests that the grain growth, or refinement, has taken place whenever the metal has been heated above some temperature below that required for transformation. From a consideration of the positions at which sections such as fig. 8 occurred it is concluded that the grain size changes have taken place above $560^\circ \pm 10^\circ\text{C}$.

There are no data on the recrystallisation kinetics of British magnesium-reduced uranium, but Hayes⁸⁾ using metal of American origin has shown that recrystallisation begins at 525°C after 4 % reduction. The change in grain size of these bars may be due to recrystallisation of the alpha grains probably combined with grain growth following upon the plastic deformation caused by the transformation. The final cooling transformation will cause plastic deformation of the central core of the bar according to the mechanisms suggested.

The surface wrinkling is due to the anisotropy of the alpha lattice. Protuberances on the surface will occur when directions of low compressive critical shear stress happen to be aligned normal to the surface.

In the $\frac{1}{2}$ at % chromium alloy the grain size was found to be virtually the same before and after cycling. Little surface wrinkling was observed on the alloy specimen (fig. 9(c)) and this is attributed to the small grain size which makes the polycrystalline metal more isotropic.

That no porosity attributable to cycling was observed has two possible explanations. The first and more likely one is that, in the conditions of the experiments, the stresses are always

symmetrical about the axes of the bars and would therefore be unlikely to lead to void formation. This was not so in the experiments of Buckley *et al.*¹⁾ where the phase boundaries were plane and where large porosities were developed. The second explanation is that voids are present and cannot be discriminated from other voids, or that they are smaller than can be detected by light microscopy. Here, as an explanation for the small size of the voids compared to those of Buckley *et al.*, symmetry of stress would have to be invoked.

12. Conclusions

All the results can be satisfactorily explained, in a qualitative manner, on the basis of a model proposed by Lehr²⁾ and Buckley *et al.*¹⁾ but elaborated here to include cylindrical interfaces. The essence of the model for alpha-beta cycling in uranium is that, when alpha and beta are separated by a moving interface, plastic deformation of the weaker alpha brings about a contraction in the specimen dimension normal to the interface and an expansion in the directions in the interface.

It is suggested that the general statement of the phase change cycling damage effect in metals is: when a phase boundary moves through a specimen there is a tendency for the specimen to retain the dimensions of the stronger phase in the directions tangential to the boundary. This is shown to be consistent with published information on alpha-beta and beta-gamma cycling in uranium and on alpha-gamma cycling in iron.

Several points emerge when the results are considered quantitatively.

(a) The greatest amount of damage in the form of diameter and length strains has been found at the ends of the beta cores in the experiments on bars, where phase boundary movement is predominantly axial. The damage appears to be simply dependent on the amount of the diameter transformed to beta and varies

between 0.5 % dia. strain at 30 % dia. transformed to beta and 2.0 %–3.5 % at 80 % dia. transformed to beta.

(b) With 10 % or less of the diameter transformed to beta no damage will occur. This corresponds, at 46 kW/m (14 kW/ft, the approximate C.E.G.B. reactor heat rating), to a maximum uranium temperature of 1° C above the transformation temperature.

(c) Damage does not increase with number of cycles between 13 and 100.

(d) Tubular specimens, of the dimensions examined in this work, show more damage than solid bars with comparable amounts of beta. The most striking feature of their behaviour has been a large increase in inside diameter. There is reason to believe that, in other conditions, a decrease in inside diameter could also be obtained.

Acknowledgements

The experimental work of G. Walker and the metallographic work of T. B. Wilson is gratefully acknowledged.

The authors thanks are due to Dr. H. M. Finniston for criticism and encouragement, and to the Board of Directors of C. A. Parsons & Co. Ltd., for permission to publish.

References

- 1) S. N. Buckley, A. G. Harding and M. B. Waldron, *J. Inst. Met.* **87** (1959) 150
- 2) P. Lehr, *Comptes Rendus* **244** (1957) 77
- 3) M. de Jong and G. W. Rathenau, *Acta Met.* **7** (1959) 246
- 4) Unpublished work, UKAEA (Culcheth Laboratories)
- 5) A. B. McIntosh and T. J. Heal, Second Geneva Conference (1958) 15/P/49
- 6) J. Diamond and W. B. Hall, Symposium on Nuclear Energy (Institution of Mechanical Engineers, UK) March 1956, p. 53
- 7) D. W. White Jr., *Trans. Amer. Inst. Min. (Metall.) Engrs.* **203** (1955) 1221
- 8) E. E. Hayes, USAEC Document TID-2501 (1949) pp. 217–236

METALLOGRAPHIC DETERMINATION OF THE $\text{UO}_2\text{-U}_4\text{O}_9$ PHASE DIAGRAM

B. E. SCHANER

*Bettis Atomic Power Laboratory, Operated for the U.S. Atomic Energy Commission
by Westinghouse Electric Corporation, Pittsburgh, USA*

Received 8 February 1960

The $\text{UO}_2\text{-U}_4\text{O}_9$ equilibrium phase diagram was established by using metallographic techniques. Data obtained from visual examination of the microstructure of annealed and quenched samples made from dense solid pieces of UO_2 were used to determine the solubility of U_4O_9 in UO_{2+x} as a function of temperature. Two phases, UO_2 and U_4O_{9-y} , were found to exist at room temperature between O/U ratios of 2.00 and 2.22, although at temperatures over 940°C only a single phase is present. There is a wide range of UO_{2+x} between O/U ratios of 2.000 and 2.194 at temperatures between 200° and 950°C . In addition, a range of substoichiometric U_4O_9 lies between 2.25 and 2.20 at 940°C and to 2.22 at room temperature.

Le diagramme d'équilibre de $\text{UO}_2\text{-U}_4\text{O}_9$ a été établi à l'aide de techniques métallographiques. On a utilisé les données obtenues par examen visuel de la microstructure d'échantillons d' UO_2 compacts recuits et trempés pour déterminer la solubilité du U_4O_9 dans UO_{2+x} en fonction de la température. On a trouvé que deux phases UO_2 et U_4O_{9-y} existent à la température ordinaire entre les valeurs du rapport O/U de 2,00 à

2,22; au-dessus de 940°C une seule phase est présente. Il y a un large domaine d'existence de composés de formule UO_{2+x} dont les rapports O/U varient de 2,000 à 2,194 aux températures comprises entre 200° et 950°C . De plus un domaine de composition sous-stoechiométrique U_4O_9 existe entre 2,20 à 940°C et 2,22 à la température ambiante.

Das Uran-Sauerstoff-Diagramm wurde zwischen UO_2 und U_4O_9 auf metallographischem Wege ermittelt. Die Ergebnisse, die aus der Gefügebetrachtung von geglühten und abgeschreckten, aus dichten UO_2 -Stücken hergestellten Proben gewonnen wurden, wurden zur Bestimmung der temperaturabhängigen Löslichkeit von U_4O_9 in UO_{2+x} herangezogen. Es wurde gefunden, dass bei Raumtemperatur bei einem O/U-Verhältnis von 2,00 bis 2,22 zwei Phasen, nämlich UO_2 und U_4O_{9-y} existieren, während über 940°C nur eine einzige Phase vorliegt. Zwischen 200 und 950°C gibt es einen breiten Bereich von UO_{2+x} zwischen einem O/U-Verhältnis von 2,000 und von 2,194. Ferner liegt bei 2,20 und 940°C , sowie 2,22 und Raumtemperatur bereits substöchiometrisches U_4O_9 vor.

1. Introduction

In recent years various techniques have been used to establish the $\text{UO}_2\text{-U}_4\text{O}_9$ equilibrium phase diagram¹⁻⁴). Gronvold¹) performed the most complete analysis utilizing high temperature X-ray techniques in which he found that a single phase existed at 950°C between a composition of $\text{UO}_{2.00}$ to $\text{UO}_{2.17}$. Upon cooling, the second phase, U_4O_9 , appeared. At 950°C , U_4O_9 was stable between $\text{UO}_{2.24}$ and $\text{UO}_{2.26}$; however, at low temperature, it was only stable at $\text{UO}_{2.25}$. In more recent work Willardson, Moody and Goering²) utilized electrical conduc-

tivity measurements and their results suggested that a single phase was present in the neighborhood of 200°C from a composition of $\text{UO}_{2.00}$ to $\text{UO}_{2.10}$. Blackburn³), measuring oxygen dissociation pressures, extended Gronvold's phase diagram to 1100°C and showed a range of single-phase U_4O_9 between $\text{UO}_{2.25}$ and $\text{UO}_{2.27}$ and two phases between $\text{UO}_{2.23}$ and $\text{UO}_{2.25}$.

In order to reconcile the differences among these studies and particularly those between the work of Gronvold and Willardson *et al.*, the author has reconstructed the $\text{UO}_2\text{-U}_4\text{O}_9$ portion of the uranium-oxygen system through direct

metallographic observation of the microstructure of solid high density samples. By using quenched samples, the high-temperature structure can be frozen and can then be examined at room temperature. Gronvold stated that the broad range of homogeneity of UO_{2+x} did not appear on room-temperature X-ray diffraction patterns of rapidly-cooled samples; moreover, he stated that a danger exists in assuming that high-temperature phase relationships can be deduced from quenched samples. This present study, however, indicates that work with quenched samples can, indeed, be valuable. A broad range of homogeneity was found in samples quenched from high temperatures which agrees closely with the range established by Gronvold for O/U ratios below 2.20. A range of substoichiometric U_4O_9 above $\text{UO}_{2.20}$ has also been established by this work.

2. Experimental Procedure

The specimens for this study, $0.1 \times 0.6 \times 3.8$ cm ($0.04 \times 0.25 \times 1.5$ in.) platelets of UO_2 were fabricated by pressing and sintering comminuted UO_2 powder. Mallinckrodt Chemical Works PWR Grade powder was passed through a high-speed hammer mill (mikro-atomizer) to reduce the particle size to less than 8 microns in order to increase the sinterability of the material. The milled powder was granulated with one weight percent polyethylene glycol, pressed in a hardened steel die at a pressure of 30 tons per square inch, and sintered to an average density of 98.7 % theoretical in a hydrogen atmosphere for 160 hours at $1745\text{--}1800^\circ\text{C}$. The platelets were made thin in order to prevent samples from fracturing as a result of thermal shock during subsequent heating and quenching. A chemical analysis of the platelets is given in table 1.

The microstructure of the sintered stoichiometric UO_2 , shown in fig. 1, displays an average grain size of $60\ \mu$. Because difficulty was encountered in resolving the microstructure of precipitate formed in grains smaller than $20\ \mu$, these larger grains were desirable.

To obtain the range of compositions required for this test, the UO_2 platelets were oxidized in

TABLE 1
Analysis of sintered platelet

U(VI)	0.4–0.5 wt%*	Fe	12 ppm
Total U	88.2 wt%**	Mg	20 ppm
Al	8 ppm	Mo	5 ppm
C	90 ppm*	Ni	5 ppm
Ca	7 ppm	Si	145 ppm
Cr	5 ppm	Ti	10 ppm
Cu	5 ppm		

* Polarographic analysis.

** Chemical analysis—other spectrographic analyses.

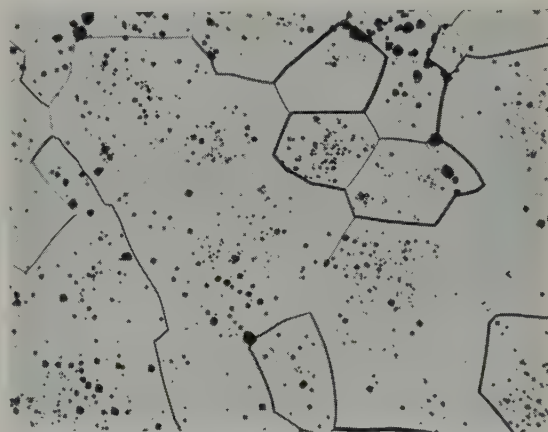


Fig. 1. Photomicrograph of $\text{UO}_{2.000}$, 98.7 % of theoretical density, etched. $\times 260$

high-temperature steam to various O/U ratios between $\text{UO}_{2.006}$ and $\text{UO}_{2.248}$. The platelets were set on an alumina boat in a globar furnace and heated in argon; preheated steam was admitted between 550 and 1500°C to produce the desired amount of oxidation. Special difficulties were encountered in producing O/U ratios in excess of 2.195. To obtain compositions to $\text{UO}_{2.25}$, it was necessary to introduce pure oxygen with the steam. Because minor temperature deviations resulted in a wide variation of resultant O/U ratios, the oxidation in this range was difficult to control. All samples were subsequently equilibrated by being annealed in helium-filled bulbs.

The composition of oxidized UO_2 samples was determined by weight gain on the assumption that the starting material was $\text{UO}_{2.000}$. The

O/U ratio was also calculated from a polarographic analysis ⁵⁾ of percent U⁺⁶ present in one platelet from each oxidation run to confirm the gravimetric determinations. The results of the two methods agreed to within ± 0.01 units of the O/U ratio. However, the values obtained from the gravimetric determination of the O/U ratios were used to construct the phase diagram.

To determine the phases present along any one isopleth, a platelet oxidized to a particular O/U ratio was first broken into eight approximately equal sections and sealed in Vycor or quartz bulbs for subsequent heating and quenching. Vycor was used for heat treatments below 1000° C, while fused quartz was used for treatments between 1000 and 1200° C. The bulbs were filled with helium to provide an inert atmosphere and to maintain a high rate of heat transfer.

Heat treatment to determine the phases present at descending temperatures was performed by first annealing at 900° C or 1200° C for a minimum of 48 hours. The annealing temperature depended upon composition and was selected, using Gronvold's phase diagram ¹⁾ as a guide, to ensure that the sample was maintained in a single-phase region. The entire set of bulbs was then slowly cooled to a temperature slightly above the previously-determined temperature of oxygen solubility. At this temperature a single bulb was quenched into water. After the furnace temperature was lowered an additional 10 or 20° C and held for a minimum of two hours another bulb was quenched. This procedure was repeated until all bulbs were quenched. In cases where the approximate temperature of precipitation was in doubt for a particular composition, the intervals were widened to 50 or 100° C to establish the range of two-phase formation prior to running a closer determination.

The bulbs were either quenched in water and allowed to cool by conduction through the walls of the bulb, or, for a more drastic quench, the bulbs were broken upon immersion in the water, thus allowing the water to contact the sample directly. Because the latter method produced a

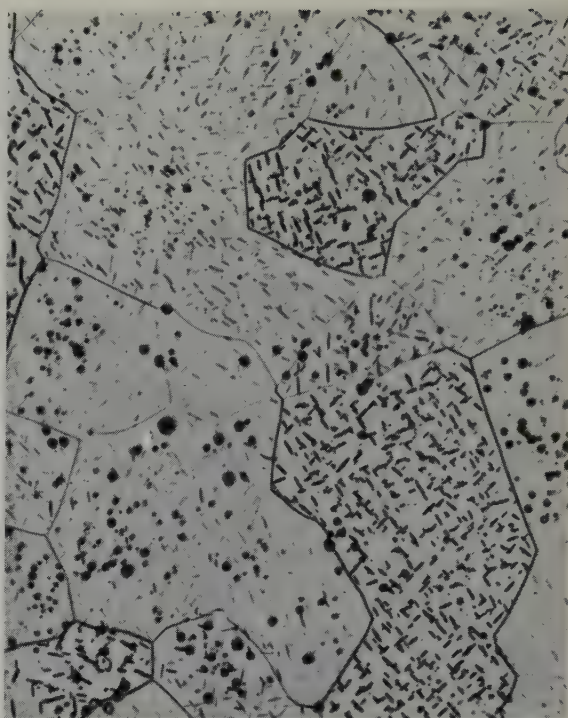


Fig. 2. Photomicrograph of UO_{2.006} slowly cooled after annealing at 900° C. etched. $\times 370$



Fig. 3. Photomicrograph of UO_{2.021} slowly cooled after annealing at 900° C. etched. $\times 370$

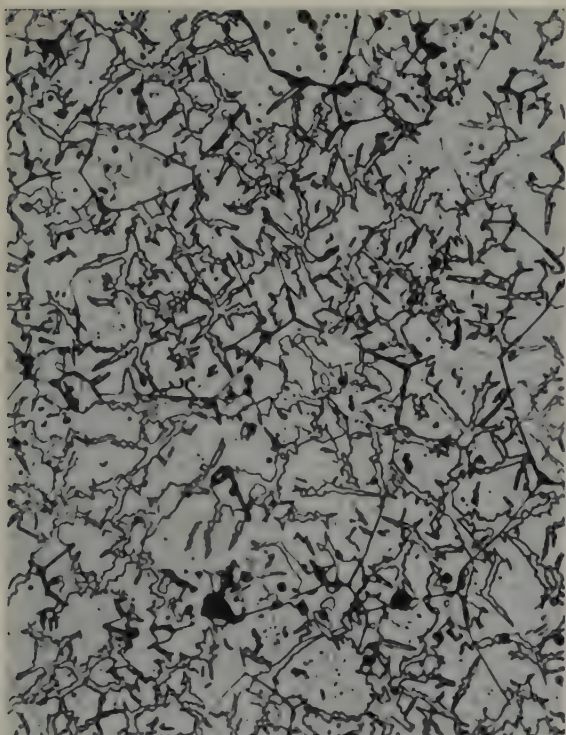


Fig. 4. Photomicrograph of $\text{UO}_{2.034}$ slowly cooled after annealing at 900° C. etched. $\times 370$



Fig. 6. Photomicrograph of $\text{UO}_{2.146}$ slowly cooled after annealing at 900° C. etched. $\times 370$

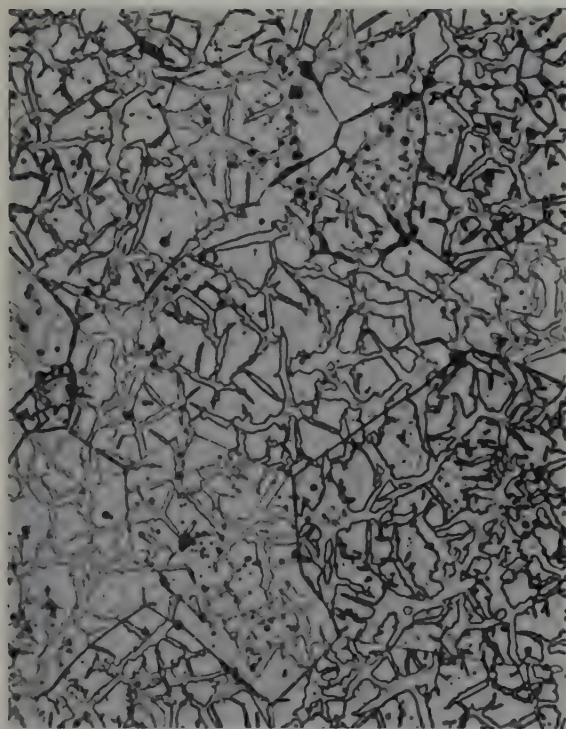


Fig. 5. Photomicrograph of $\text{UO}_{2.078}$ slowly cooled after annealing at 900° C. etched. $\times 370$

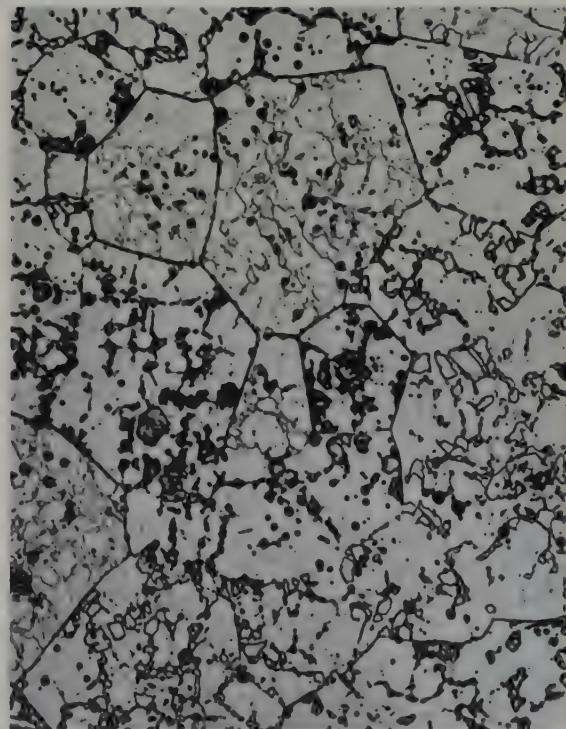


Fig. 7. Photomicrograph of $\text{UO}_{2.176}$ slowly cooled after annealing at 900° C. etched. $\times 370$

more rapid cooling, precipitation during cooling was retarded to a greater degree. This method of quenching was especially necessary at higher O/U ratios where the second phase precipitated from solution even with rapid cooling.

The samples were prepared for metallographic observation by mounting them in an amber epoxy plastic which hardened at room temperature and was cured at 60° C for two hours. The initial rough polishing was done wet on 240-, 400-, and 600-grit silicon carbide polishing paper and was followed by lapping with 3 μ and then 6 μ diamond dust. Final polishing was done with gamal alumina, a fine alumina polishing grit. To expose the grain boundaries of the phases, etching was performed with a 10:1 solution of H₂O₂ and H₂SO₄.

3. Analysis of Results

3.1. CONSTRUCTION OF THE PHASE DIAGRAM

Metallographic examination revealed that a second phase precipitated in samples of certain O/U ratios slowly cooled from high temperatures. It was also observed that a single-phase structure could be obtained by quenching samples of nonstoichiometric UO₂ from high temperatures. These facts were used to construct the UO₂-U₄O₉ phase diagram.

To determine the equilibrium microstructure at room temperature of samples of various O/U ratios, samples were slowly cooled after being annealed at 900° C. Microstructures of compositions between UO_{2.006} to UO_{2.176} are shown in fig. 2 through fig. 7. At the lower oxygen contents, a fine acicular structure of U₄O₉ can be noted. As the O/U ratio increases, in turn, the U₄O₉ forms crosses and interconnects until it encircles the UO₂ and forms islands of UO₂ in a matrix of U₄O₉.

Samples slowly cooled from high temperatures to successively descending temperatures and quenched at these successive temperatures, showed the formation of another phase at one particular temperature. Figs. 8 through 18 are typical examples of such isoplethal examinations of UO_{2.009}, UO_{2.021}, UO_{2.122}, and UO_{2.176},

respectively. For example, fig. 8 illustrates a sample of UO_{2.009} quenched from 360° C after annealing at 900° C for 48 hours, and displays a structure identical with sintered UO_{2.000}; fig. 9, a sample of the same composition quenched from 350° C, shows precipitation of acicular and massive U₄O₉. Consequently, the boundary between UO_{2+x} and U₄O₉ + UO_{2+x} for this composition lies between 360 and 350° C. The isopleth of UO_{2.021} is illustrated in figs. 10 and 11, with precipitation occurring between 420 and 410° C.

The shape of the precipitate and the mode of

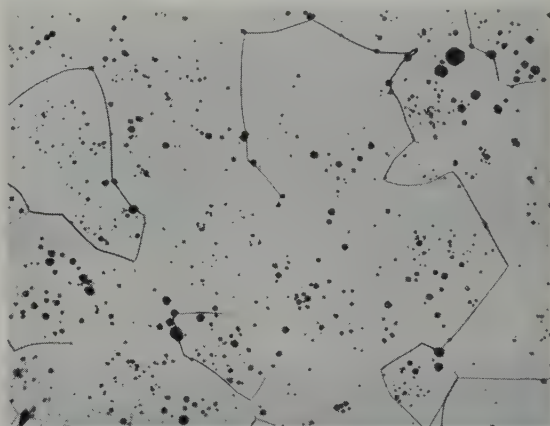


Fig. 8. Photomicrograph of UO_{2.009} annealed at 900° C, slowly cooled to 360° C, and quenched by breaking bulb containing sample under water. etched. $\times 260$

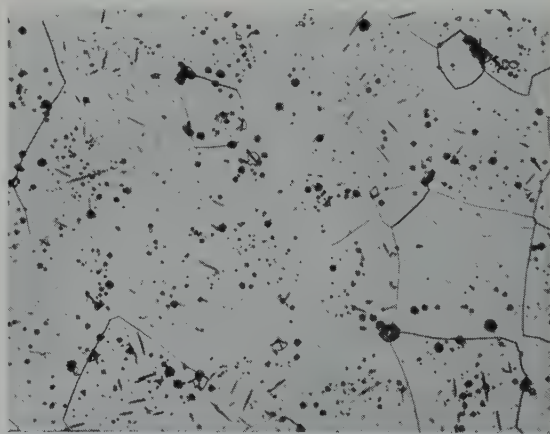


Fig. 9. Photomicrograph of UO_{2.009} annealed at 900° C, slowly cooled to 350° C and quenched by breaking bulb containing sample under water. etched. $\times 260$



Fig. 10. Photomicrograph of sample of $\text{UO}_{2.021}$, annealed at 900°C , slowly cooled to 420°C and quenched in water without breaking bulb. etched. $\times 260$

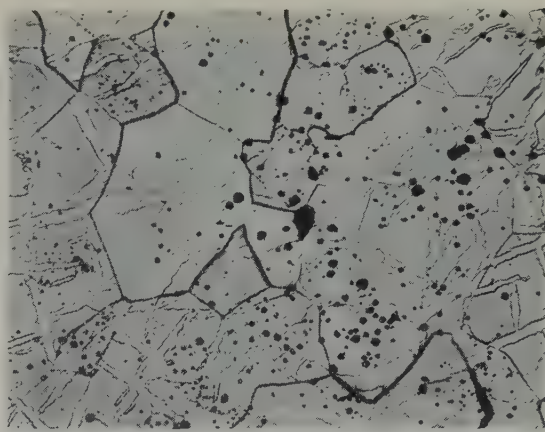


Fig. 13. Photomicrograph of $\text{UO}_{2.122}$, annealed at 900°C , slowly cooled to 550°C and quenched by breaking bulb containing sample under water. etched. $\times 260$

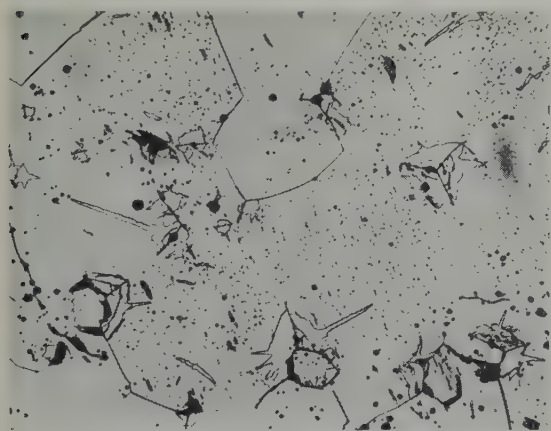


Fig. 11. Photomicrograph of sample of $\text{UO}_{2.021}$, annealed at 900°C , slowly cooled to 410°C and quenched in water without breaking bulb. etched. $\times 260$

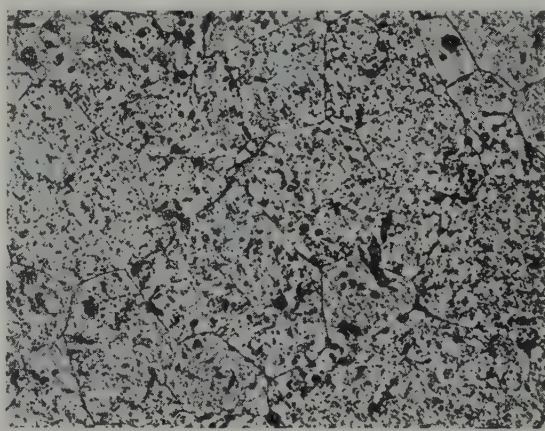


Fig. 14. Photomicrograph of sample of $\text{UO}_{2.176}$, annealed at 1200°C , slowly cooled to 865°C and quenched. etched. $\times 260$

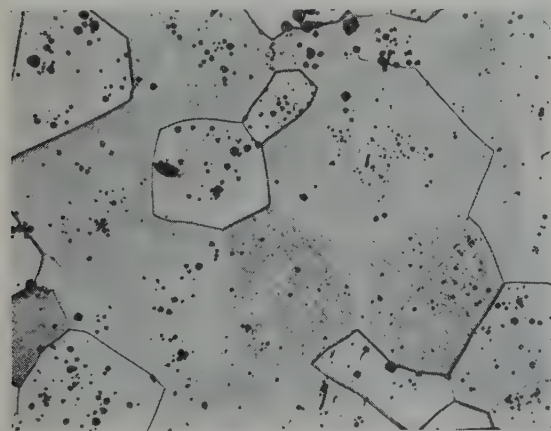


Fig. 12. Photomicrograph of $\text{UO}_{2.122}$, annealed at 900°C , slowly cooled to 650°C and quenched by breaking bulb containing sample under water. etched. $\times 260$

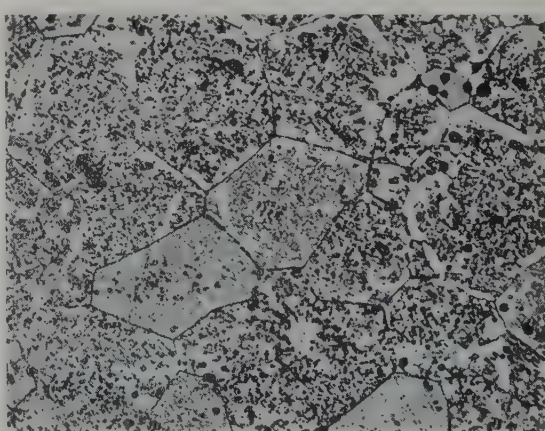


Fig. 15. Photomicrograph of sample of $\text{UO}_{2.176}$, annealed at 1200°C , slowly cooled to 845°C and quenched. etched. $\times 260$

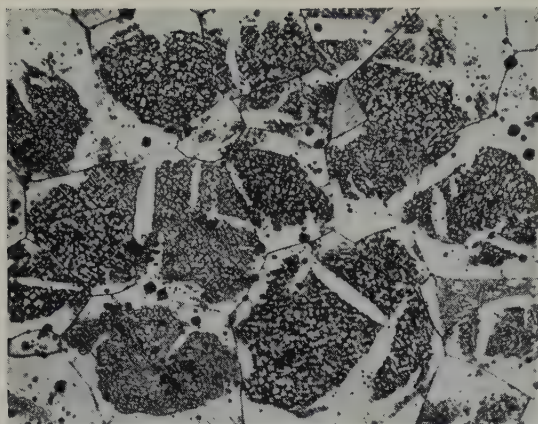


Fig. 16. Photomicrograph of sample of $\text{UO}_{2.176}$, annealed at 1200°C , slowly cooled to 690°C and quenched, etched. $\times 260$

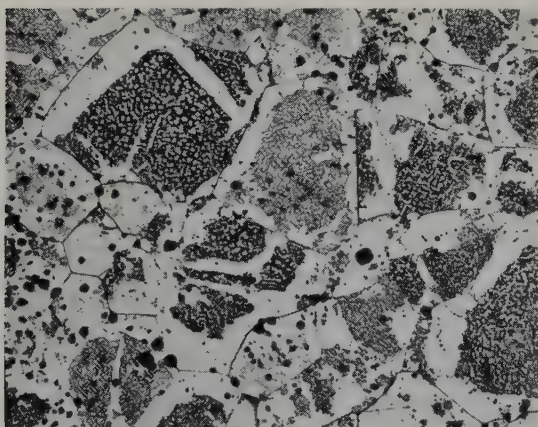


Fig. 17. Photomicrograph of sample of $\text{UO}_{2.176}$, annealed at 1200°C , slowly cooled to 590°C and quenched, etched. $\times 260$

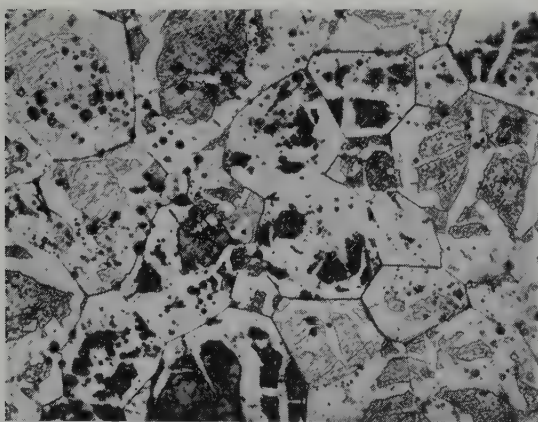


Fig. 18. Photomicrograph of sample of $\text{UO}_{2.176}$, annealed at 1200°C , slowly cooled to 490°C and quenched, etched. $\times 260$

its formation depends upon its history of thermal treatment. U_4O_9 apparently has a tendency to nucleate and grow at grain boundaries and a lesser tendency to grow inward into the grain in the form of a platelet. A comparison of fig. 11, a sample of $\text{UO}_{2.021}$ quenched from 410°C , and fig. 3, a sample allowed to cool slowly to room temperature from 900°C , shows that by annealing UO_{2+x} isothermally below the temperature of oxygen solubility rather than allowing it to cool slowly through the two-phase region, U_4O_9 precipitates in bulk form primarily at the grain boundaries. A void is formed at the grain boundary of the parent UO_{2+x} and the precipitated U_4O_9 phase which results from the conversion of UO_{2+x} to higher density U_4O_9 . These voids are visible as the dark regions associated with the precipitates in fig. 11. However, as the U_4O_9 grows into the grain, no void forms and it is presumed that the intergranular precipitate remains under stress. Subsequently, upon cooling of the sample of $\text{UO}_{2.021}$ to room temperature after annealing at 410°C , precipitation occurs within the grain in the form of a Widmanstätten structure of fine needles. These needles, similar to those found in samples annealed above the oxygen solubility temperature and slowly cooled, are actually the cross section of thin platelets which have intersected the polished surface of the sample. A number of grains in samples of compositions from $\text{UO}_{2.008}$ to $\text{UO}_{2.021}$ were examined to determine the orientation of the precipitated phase. In most grains, the needles were aligned in four directions, but in a few cases only three directions were noted. These observations indicate that the U_4O_9 platelets precipitate on planes parallel to the $[111]$ planes of the parent UO_{2+x} phase. These results are in agreement with work done by Tuxworth and Evans⁶⁾ on a sample of fused $\text{UO}_{2.08}$.

Figs. 12 and 13, two samples of $\text{UO}_{2.122}$, show the typical microstructure formed at higher oxygen concentrations. The needles in fig. 13, a sample quenched from 550°C , appear to be less symmetrically oriented than in the sample of $\text{UO}_{2.021}$ in fig. 3, apparently due to coalescence

of the U_4O_9 as it grows from the parent UO_{2+x} . The network of U_4O_9 increases in size as the solubility decreases with descending temperatures.

At O/U ratios lower than 2.12, precipitation of massive U_4O_9 occurred at the sample grain boundaries and by precipitation of needles within the grains (fig. 11). However, if the quench rate was not sufficiently rapid to retard all precipitation during cooling from the quench temperature to room temperature, some confusion resulted because, upon cooling, a finely-dotted structure appeared in the UO_2 matrix, fig. 10. Examination of these dots under an electron microscope revealed that each dot had a diamond shape under a superimposed cross, fig. 19. Apparently, this structure is the nucleus from which needles would grow if the sample were allowed to cool at a slower rate through the two-phase region, fig. 20.

The interpretation of quenched samples with O/U ratios over 2.16 becomes increasingly difficult because even the most rapid quenching rate is not sufficient to retain the oxygen in solution. To some extent, the resultant precipitation masked the structure formed at the quench temperature. The series of $\text{UO}_{2.176}$ samples shown in figs. 14-18 illustrate the precipitation of U_4O_9 from samples quenched without breaking the bulb. Therefore this

permits the precipitation to take place in the UO_{2+x} phase during cooling which causes the

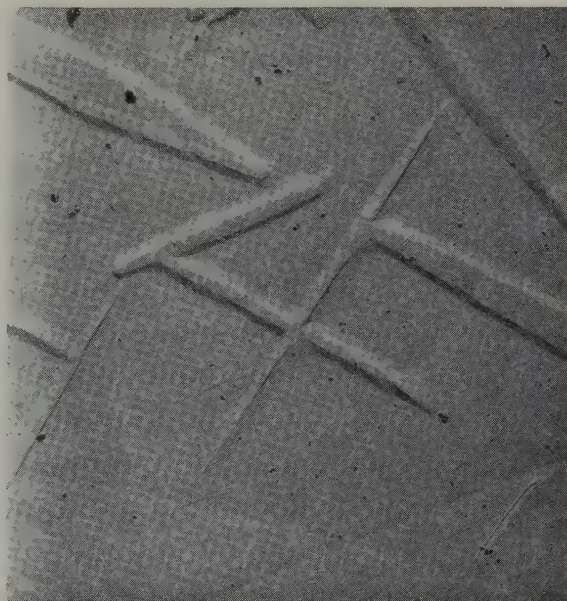


Fig. 20. Electron photomicrograph of direct carbon replica of polished and etched sample of $\text{UO}_{2.057}$. Replica has negative shadow. Sample was annealed at 900°C , slowly cooled to room temperature. $\times 13000$.

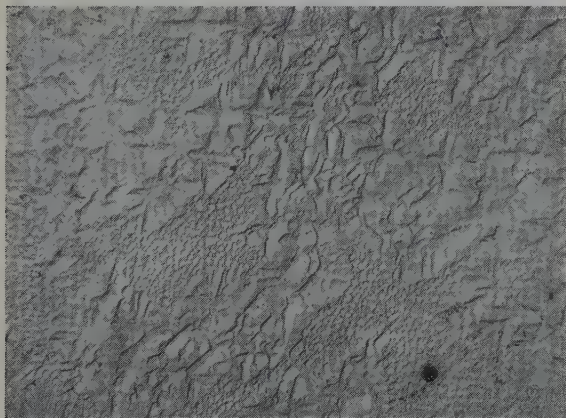


Fig. 19. Electron photomicrograph of direct carbon replica of polished and etched $\text{UO}_{2.057}$. Replica has negative shadow. Sample was annealed at 900°C . $\times 8500$.

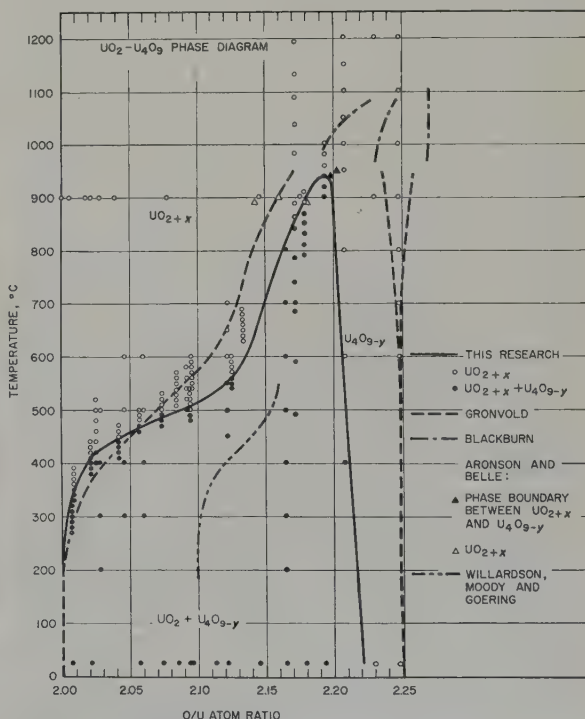


Fig. 21. $\text{UO}_2\text{-U}_4\text{O}_9$ phase diagram.

white U_4O_9 phase to stand out against the dark pattern of a mixture of UO_{2+x} and U_4O_9 . The solubility of oxygen decreases slowly from 850 to 550° C as noted by the relatively small increase in U_4O_9 over this temperature range and then decreases rapidly at 490° C as noted by the large increase in the amount of U_4O_9 .

The data obtained by examining the microstructure of quenched samples over a range of compositions between an O/U ratio of 2.008 and 2.248 are plotted in fig. 21. The diagram illustrates the transition from a single-phase to a two-phase structure to a composition of $\text{UO}_{2.194}$ as the temperature is reduced. This portion of the phase diagram corresponds closely to that of Gronvold¹⁾. However, the revision proposed by Willardson *et al.*²⁾ suggesting that the UO_{2+x} region at 180° C be extended to $\text{UO}_{2.10}$ does not appear to be warranted in view of the evidence presented here.

The significant area in which this diagram differs from the others mentioned is that a single-phase region was found at O/U ratios above 2.194 at 940° C and above 2.22 at room temperature. Gronvold¹⁾ had indicated that a single-phase region of substoichiometric U_4O_9 (U_4O_{9-y}) existed but only for a much more limited range of compositions and at temperatures over 400° C. The homogeneity range found here is also in disagreement with the results from the oxygen pressure measurements of Blackburn³⁾ which show a two-phase region between compositions of $\text{UO}_{2.20}$ and $\text{UO}_{2.23}$ at 1000° C. However, Aronson and Belle⁷⁾, utilizing an electrochemical technique to study the oxygen-uranium system, found a phase boundary between UO_{2+x} and U_4O_9 at 940° C at a composition of $\text{UO}_{2.20}$; this observation supports the results found by the author.

Because of the difficulty encountered in preparing solid platelets between O/U ratios of 2.20 to 2.25, only sparse data are available in this region of the phase diagram, and no data are presented for compositions in excess of $\text{UO}_{2.248}$.

Thus, the phase diagram proposed in fig. 21 indicates the formation of a solution of oxygen

in UO_2 stable above 940° C to a composition of at least $\text{UO}_{2.25}$ which decomposes at lower temperatures into a stoichiometric UO_2 phase and a substoichiometric U_4O_{9-y} phase.

The single-phase microstructure of U_4O_9 (shown in fig. 22) is from a sample of $\text{UO}_{2.248}$ which was slowly cooled. A closer examination of fig. 22 shows that some of the grain boundaries appear as dotted lines rather than solid lines, as shown in fig. 1 for a sample of $\text{UO}_{2.000}$. Exami-

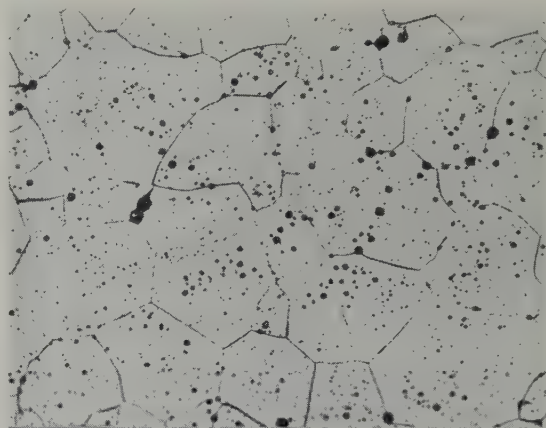


Fig. 22. Photomicrograph of a sample of $\text{UO}_{2.248}$ annealed at 1200° C for 48 hours and slowly cooled. etched. $\times 260$

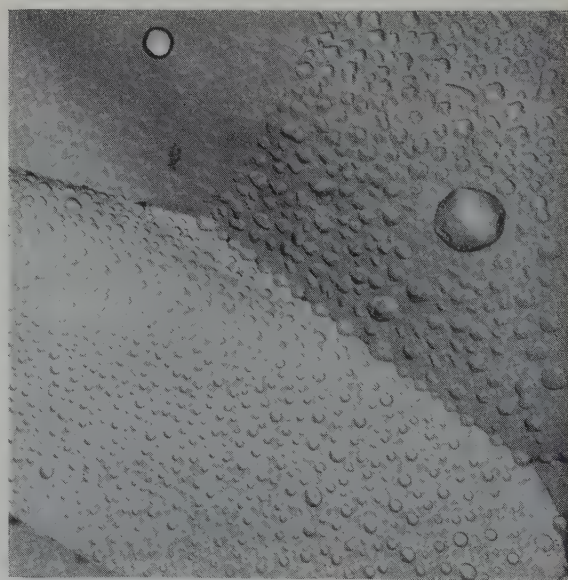


Fig. 23. Electron photomicrograph of direct carbon replica of fractured sample of $\text{UO}_{2.229}$. The replica has a positive shadow. $\times 3800$.

nation of a fractured surface at high magnifications by the use of electron microscope techniques revealed that these dots were small pores distributed along the grain boundaries. Fig. 23, an electron photomicrograph of a sample of $\text{UO}_{2.229}$ broken so that the fracture occurred along the grain boundaries, shows that the grain boundaries are covered uniformly with fine pores. In addition, these pores appear to be preferentially oriented and have a geometric symmetry similar to the pores found by Padden⁸) in dense, sintered UO_2 bodies. Identification of this structure as porosity rather than precipitate was accomplished by making a carbon replica of the fractured sample and observing the shadows formed by vapor-deposited uranium. The origin of these pores is not clear although they may form as the UO_{2+x} transforms to U_4O_9 . This transformation, as mentioned previously, is associated with a volume increase which produces a gap between the U_4O_9 and the grain boundary.

3.2. X-RAY AND HARDNESS DATA

Phase identification was made and lattice parameters were measured, using Cu K_α radiation, by reflection from the surface of the polished samples. The two phases present between compositions of $\text{UO}_{2.25}$ and UO_2 were identified as being of cubic structure. The presence of a second cubic phase in slowly-cooled samples was not detected with X-rays until a composition of $\text{UO}_{2.021}$ was reached, although metallographically a second phase was observed with compositions as low as $\text{UO}_{2.006}$.

Since it was possible to obtain the UO_{2+x} phase at room temperature by quenching, for a wide range of oxygen concentrations, X-ray measurement could be used to determine the dependence of the lattice parameter on oxygen content. A series of samples covering a representative range of O/U ratios were prepared, annealed at 900°C , and quenched by breaking the bulbs under water to retard precipitation. The lattice parameters were then measured on the resultant single-phase UO_{2+x} structures. These parameters are plotted in fig. 24 as a

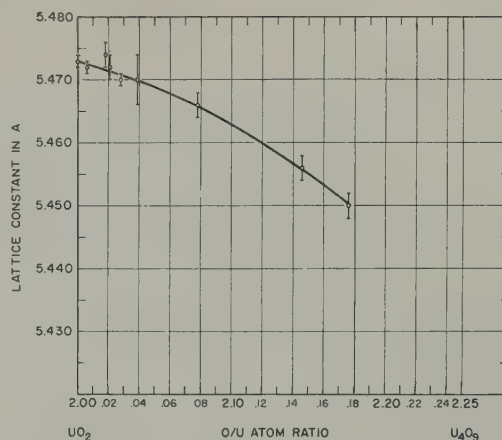


Fig. 24. Lattice constants of the UO_{2+x} phase at different O/U ratios. Samples annealed at 900°C for 67 hours and quenched to room temperature.

function of O/U ratio and show a decrease in lattice size with an increase in oxygen content. The lattice constants for U_4O_9 , given in table 2, verify the presence of substoichiometric U_4O_9 . A single phase was detected between $\text{UO}_{2.208}$ and $\text{UO}_{2.248}$ with a lattice contraction produced by increased oxygen content.

The hardness of annealed and quenched samples of UO_{2+x} (single-phase) was measured using a Knoop diamond indenter with a load of 500 grams. Fifteen hardness impressions were made in the polished surface of each sample, and the average hardness was plotted versus

TABLE 2
Lattice constants of the U_4O_9 phase

O/U ratio	a_0 (Å)	Thermal treatment
2.208	5.454 ± 0.002	Annealed at 1200°C for 64 h and quenched.
2.248	5.437 ± 0.002	
2.208	5.447 ± 0.005	Annealed at 1200°C for 64 h, slowly cooled to 600°C , held for 24 h and quenched.
2.248	5.441 ± 0.005	
2.229	5.443 ± 0.002	Annealed at 1200°C for 48 h and slowly cooled.
2.248	5.441 ± 0.002	

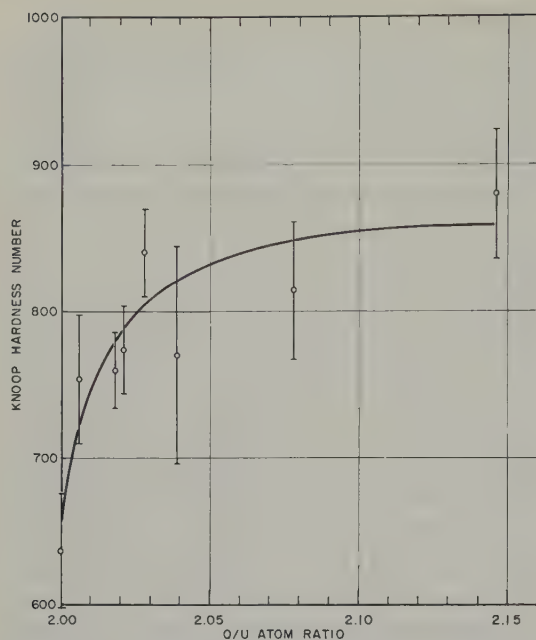


Fig. 25. Effect of oxygen content on hardness of UO_{2+x} solid solution. Samples annealed at 900°C for 67 hours and quenched to room temperature. Knoop diamond indenter, 500 g load.

composition, fig. 25. Evidently, only a small amount of excess oxygen results in a large increase in the hardness of the UO_{2+x} .

4. Conclusions

In summary, the phase diagram constructed using the data from metallographic examination of annealed and quenched samples establishes the following four points:

- 1) Two phases, UO_2 and U_4O_{9-y} , are present at room temperature between O/U ratios of 2.00 and 2.22.
- 2) At temperatures over 940°C only a single phase exists.

3) A broad range of UO_{2+x} is present between O/U ratios of 2.00 and 2.194 at temperatures between 200 and 940°C .

4) A range of substoichiometric U_4O_9 (U_4O_{9-y}) extends from an O/U ratio of 2.25 to a ratio of 2.20 at 940°C and to 2.22 at room temperature. The region above U_4O_9 was not studied.

Acknowledgements

The author wishes to thank Dr. R. Berman for the X-ray measurements, Mr. T. Padden for the hardness measurements, Mr. G. Cicconi for his technical assistance, Mr. P. Schnizler for the electron microscope work, Drs. J. Belle and S. Aronson for their helpful criticism, and especially Dr. B. Lustman whose insistence that the phase diagram could be obtained by metallographic techniques brought this work into being.

The work was performed at the Bettis Plant operated by Westinghouse Electric Corporation for the U.S. Atomic Energy Commission under AEC Contract AT-11-1-GEN-14.

References

- 1) F. Gronvold, J. Inorganic and Nuclear Chemistry 1 (1955) 359
- 2) R. K. Willardson, J. W. Moody and H. L. Goering, J. Inorganic and Nuclear Chemistry 6 (1958) 19
- 3) P. E. Blackburn, J. Phys. Chem. 62 (1958) 897
- 4) H. Hering and P. Perio, Bull. Soc. Chem. (1952) 351
- 5) R. M. Burd and G. W. Goward, Westinghouse Atomic Power Division (USA) report WAPD 205 (1959)
- 6) R. H. Tuxworth and W. Evans, J. Nucl. Mat. 1 (1959) 302
- 7) S. Aronson and J. Belle, J. Chem. Phys. 29 (1958) 151
- 8) J. Belle and B. Lustman, Westinghouse Atomic Power Division (USA) report WAPD 184 (1957)

THE LATTICE SPACINGS OF THORIUM-LANTHANUM ALLOYS

D. S. EVANS, G. V. RAYNOR and R. T. WEINER

Department of Physical Metallurgy, University of Birmingham, Birmingham 15, UK

Received 11 January 1960

The lattice spacing/composition curve for the thorium-lanthanum alloy system has been investigated, for comparison with previous work on the thorium-cerium system. The stringent precautions necessary to minimise contamination (principally by nitrogen) are outlined. The results indicate that face-centred cubic thorium and lanthanum form a complete series of solid solutions; the experimentally determined lattice spacings lie on a smooth and continuous curve, except for a narrow range of composition from about 52 to 60 at % lanthanum, in which erratic results may be obtained. The reason for the scatter at these compositions is thought to lie in an enhanced solubility of nitrogen in the alloys.

The lattice spacing curve obtained is not of the same form as that for the thorium-cerium alloys, and the reason for this is discussed in terms of the relative ease with which cerium may change its effective valency in solid solution.

La courbe de variation du paramètre en fonction de la composition dans le système Th-La a été déterminée pour comparer avec le travail précédent effectué sur le système Th-Ce. Les précautions rigoureuses nécessaires pour minimiser la contamination (principalement par l'azote) sont soulignées. Les résultats indiquent que le thorium et le lanthane cubique à faces centrées forment une série continue de solutions solides. Les paramètres déterminés expérimentalement se placent sur une courbe régulière et continue, sauf pour un domaine étroit de composition compris entre 52 à

60 at % de lanthane dans lequel des résultats erratiques sont obtenus. La raison de cette dispersion de résultats est estimée due à une solubilité accrue de l'azote dans ces alliages.

La courbe des paramètres n'est pas de la même forme que celle des alliages thorium-cérium. La raison de ceci est discutée en prenant comme argument la facilité relative avec laquelle le cerium peut modifier sa valence réelle en solution solide.

Der Zusammenhang zwischen dem Gitterparameter und der Konzentration von Thorium-Lanthan-Legierungen wurde untersucht, um Vergleiche mit früheren Arbeiten über Thorium-Cer anzustellen. Es werden die erheblichen Vorsichtsmassnahmen zur Vermeidung von Verunreinigungen (insbesondere durch Stickstoff) herausgestellt. Die Ergebnisse zeigen, dass das kubisch flächenzentrierte Thorium und Lanthan eine durchgehende Mischkristallreihe bilden; dabei liegen die ermittelten Gitterparameter auf einer glatten, stetigen Kurve mit Ausnahme des Bereichs von 52 bis 60 At % Lanthan, wo die experimentell bestimmten Werte vermutlich nicht stimmen. Der Grund für die Streuung in diesem Bereich wird in der erhöhten Stickstofflöslichkeit in diesen Legierungen gesucht.

Die Gitterparameter-Kurve hat eine andere Gestalt als die von Thorium-Cer-Legierungen, was als Folge der verhältnismässig grossen Bereitschaft von Cer diskutiert wird, in Mischkristallen seine Valenz zu ändern.

1. Introduction

As part of a programme for the investigation of the alloying properties of the heavy metals, the lattice spacings in the system thorium-lanthanum have been examined, for comparison with previous work dealing with the thorium-cerium alloys. According to the work of Weiner, Freeth and Raynor¹⁾ and of Van Vucht²⁾, there is a very marked deviation from Vegard's

Law in spite of the formation of a complete series of solid solutions (fig. 1). This was attributed to a contraction of the cerium atoms in solid solution, due to a transition of the 4f electron into a 5d orbital, and made possible by the strain energy consequent on the substitution of cerium for thorium on the lattice of the latter. It is known that a considerably contracted form of cerium may be produced by

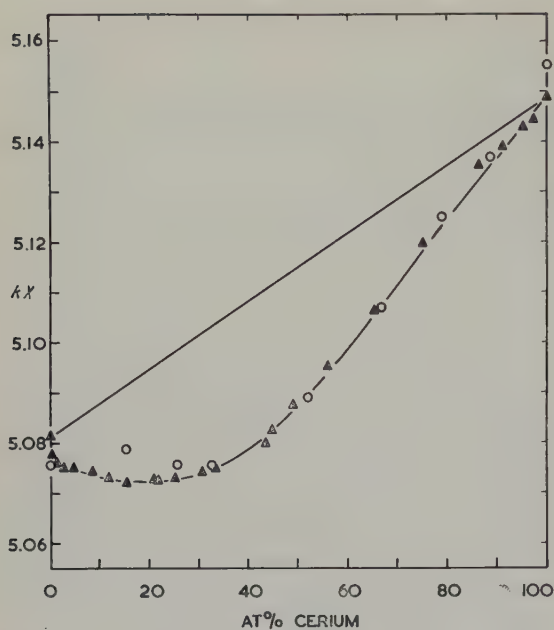


Fig. 1. Lattice spacings in the system thorium-cerium.

▲ Weiner *et al.*¹⁾
○ Van Vucht²⁾.

the application of high pressures³⁾. Lanthanum is physically and chemically very similar to cerium; although it also suffers a transformation on the application of sufficient pressure⁴⁾, the pressure required is considerably greater than for cerium. There is therefore less likelihood of any effect analogous to the electronic transformation responsible for anomalies in the thorium-cerium system being observed in thorium-lanthanum alloys, and the present work was undertaken to investigate this point.

2. Materials and Methods

Alloys were prepared from the following materials:

(i) Iodide thorium, for which a typical analysis shows 0.02 wt % carbon, less than 0.1 wt % of metallic impurities, 0.01 wt % nitrogen and 0.01 wt % oxygen.

(ii) Electrolytic thorium, which was 99.5 wt % pure, the main impurity being oxygen, together with 0.015 wt % nitrogen and 0.02 wt % calcium. The major proportion of the latter impurity would be expected to volatilise during alloy preparation.

(iii) Sintered bar thorium, of purity stated to be slightly lower than the electrolytic material.

(iv) Lanthanum, prepared by the reduction of spectroscopically standardized oxide, containing negligible amounts of metallic impurity except for 0.001 wt % iron.

The lanthanum metal was obtained from Messrs. Johnson Matthey and Company Limited, and the three grades of thorium were kindly presented by the Atomic Energy Research Establishment, Harwell.

All alloys were prepared in a non-consumable electrode arc-furnace, previously evacuated through a diffusion/rotary pump combination to below 10^{-5} mm Hg. Specimens were melted in an atmosphere of approximately 15 cm of argon, which was purified prior to striking the arc on the alloy by melting a zirconium button and maintaining it molten for 5 minutes. The weight loss observed was very small, and since check chemical analyses showed only slight deviations from the intended compositions, these were taken in general as satisfactory for use. In general, alloys containing high proportions of lanthanum were made first, and, after examination, diluted with thorium; precautions were taken to guard against excessive increase of impurity levels and cumulative errors in composition.

Homogenization was carried out for 14 to 21 days at 1000° C (thorium-rich alloys) to 700° C (lanthanum-rich alloys); the specimens were wrapped in degassed tantalum sheet after heavy cold deformation, and sealed two or three at a time in silica tubes, degassed and evacuated to 2×10^{-6} mm Hg. This procedure was adopted so that, if accidental contamination had occurred during annealing, the effects would not be confined to a single alloy and would thus be more readily recognised. After homogenization, annealing was continued for several days at 675° C in the case of the alloys studied after preliminary work had been completed.

The techniques adopted for preparing, annealing and exposing filings of the alloys were dictated by prior and concurrent work⁵⁾ on

the lattice spacings of pure thorium, which showed that great care was necessary to avoid contact with air at all stages in the preparation and treatment of filings if abnormally high lattice spacings were to be avoided. As a result of the investigation of thorium, the technique initially adopted for thorium-lanthanum alloys was modified in the later stages of the work reported in this paper, and reference is made to this factor in describing experimental results. Most of the results reported were, however, obtained with a standard technique found suitable for thorium, which is fully described by Evans and Raynor⁵). Briefly, filings prepared under carbon tetrachloride were transferred before drying to a tantalum tray which had been outgassed at 950° to 1000° C, and which was then sealed by folding. The boat and contents were transferred to an outgassed annealing furnace tube capable of continuous evacuation, and the excess tetrachloride was evaporated. The heat-treatment then followed, the rate of heating to the annealing temperature being controlled to prevent any rise of pressure above 5×10^{-5} mm Hg. Thereafter the vacuum in the system improved to 5×10^{-6} mm Hg over 20 to 30 minutes, reaching, if the heat-treatment was prolonged, 2×10^{-6} mm after 60 minutes. At the end of such treatments, filings were rapidly cooled by removing the furnace, and immediately made up into Debye-Scherrer specimens. In the earlier stages of the work the filings were placed in outgassed silica capillaries (0.35 to 0.5 mm bore), which were evacuated to 10^{-1} mm Hg and sealed; it was later found that improved diffraction patterns were obtained from filings coated on to a greased silica rod.

X-ray diffraction patterns were obtained at room temperature using a Philips Debye-Scherrer camera of radius 11.483 cm, in which specimens were exposed to copper K_α radiation ($\lambda_{\alpha_1} = 1.537\,395$ kX ; $\lambda_{\alpha_2} = 1.541\,232$ kX). Satisfactory high angle diffractions were observed, and systematic errors were eliminated by the use of the Nelson-Riley extrapolation function⁶). Correction was also made for refraction by the

method of Wilson⁷). It is estimated that the accuracy obtained was ± 0.0001 to 0.0002 kX for thorium-rich alloys, and ± 0.0003 to 0.0005 kX for lanthanum-rich alloys, for which the quality of the films deteriorated slightly.

Several alloys were in addition examined metallographically, using conventional methods.

3. Lattice Spacings of the Pure Metals

In the course of the work, lattice spacing values were obtained for the various samples of pure metals used, taking all the precautions to avoid contamination during preparation or heat-treatment described by Evans and Raynor⁵). For thorium (face-centred cubic below approximately 1400° C), annealed as filings for one hour at 675° C, the values obtained were:

- (i) Iodide thorium: 5.0741 ± 0.0002 kX
- (ii) Sintered bar thorium: 5.0777 ± 0.0002 kX
- (iii) Electrolytic thorium: 5.0778 ± 0.0001 kX .

The electrolytic and sintered bar material have the same lattice spacing, within the limits of experimental error.

Lanthanum exists in at least three forms. The close-packed hexagonal α form which is stable at room temperature was found by Spedding and co-workers⁸) to be characterized by the packing sequence of close-packed hexagonal planes ABAC rather than ABAB, so that the lattice spacings may be written $a = 3.762 \pm 0.002$ kX , $c = 12.134 \pm 0.003$ kX with $c/a = 3.2252$ ⁸). At a transformation temperature of 340° C⁹), face-centred cubic β -lanthanum is formed, with a lattice spacing given as approximately 5.31 kX by Spedding and co-workers⁸). At 870° C a further transformation occurs, to give a γ -form of unknown crystal structure.

In the present work, filings of lanthanum were annealed at a temperature of 675° C and rapidly cooled. This treatment sufficed to maintain the β -form free from admixture with α -lanthanum. The lattice spacing obtained for filings prepared under carbon tetrachloride and annealed in a closed tantalum boat was

5.2951 ± 0.0005 kX . It was possible, however, to obtain for filings made in air and annealed under less stringent conditions, lattice spacing values as high as 5.2965 kX . Traces of a second face-centred cubic diffraction pattern, identified as due to lanthanum nitride, were present on all films, suggesting the material as supplied to be saturated with nitrogen.

4. Thorium-Lanthanum Alloys

Above 340°C , both thorium and lanthanum have face-centred cubic structures, and since their atomic diameters differ only by 4 %, complete solid solution formation would be expected; this is confirmed by the work of Peterson and Mickelson¹⁰).

(i) Preliminary experiments. — Fourteen alloys covering the whole range of compositions were prepared using electrolytic thorium, and lattice spacings were determined from filings which had been prepared in air, and annealed for the relief of strain in open molybdenum boats. These lattice spacings are plotted in fig. 5 as black triangles, and are consistent with the existence of an extensive solid solution of lanthanum in thorium from 0 to 50 at % lanthanum, and a solid solution of thorium in lanthanum from 60 to 100 at % lanthanum. A somewhat unexpected scatter of results in the range 50 to 60 at % lanthanum, however, made interpretation uncertain in this region, though no diffraction patterns corresponding to the coexistence of two saturated phases were obtained. This survey was completed before the critical examination by Evans and Raynor⁵) of the correlation between contamination and the variability of the lattice spacing of thorium, so that the whole range of alloys was re-examined in the light of this correlation.

(ii) Final Results. — According to the work of Evans and Raynor⁵), thorium filings prepared in air and annealed in open boats were characterized by lattice spacings in the range 5.078 to 5.082 kX , the higher spacings corresponding to the higher annealing temperatures. Reasons were given for attributing this effect to contamination due to nitrogen, by adsorption

during filing and subsequent diffusion during annealing, and by pick-up from the furnace atmosphere. Preparation of filings under carbon tetrachloride and annealing in closed tantalum boats effectively minimised contamination, and reproducible results for the lattice spacing of thorium, as given in Section 3, were obtained except after unnecessarily long heat-treatments at temperatures exceeding about 750°C . To obtain similar information for the thorium-lanthanum alloys, a specimen containing 54.1 at % lanthanum was examined in some detail. The spacings obtained after filing in air and annealing in open boats are summarized, in terms of time and temperature of annealing, in fig. 2. The results are practically independent of time, but increase with increasing temperature up to 820°C ; the scatter at 820° is probably due to relatively large changes, with temperature, in the solubility of some contaminant in this region, as suggested in fig. 3. The results for filings made out of contact with air, and annealed in closed boats, were again independent of time of annealing, but varied slightly with temperature, as shown in fig. 3. By analogy with the similar results obtained for pure thorium the broken line in fig. 3 corresponds with the saturation of the alloy with nitrogen, which appears to reach a maximum at 825°C . Fig. 3 also indicates that heat-treatment in open boats leads to contamination, in excess of that produced by nitrogen, possibly due to carbon or silicon.

A dependence of lattice spacing on annealing temperature, similar to that for the 54.1 at % lanthanum alloy, was observed for all the alloys used in the present work; in general, filings prepared in air and annealed in open boats had lattice spacings approximately 0.0015 kX larger than corresponding filings made under carbon tetrachloride and annealed in closed boats. For this reason the latter technique was adopted throughout the remainder of the work, and a standard annealing temperature of 675°C was chosen for strain relief.

Of the alloys examined, several were made from sintered bar and electrolytic thorium,

which correspond to lattice spacings higher than that of iodide thorium by 0.0036 kX . As shown in fig. 4a, the lattice spacings obtained for such alloys are slightly but systematically higher than those obtained for alloys made from iodide thorium under exactly the same conditions. It was, therefore, considered justifiable to correct the spacings of the alloys which contained sintered bar or electrolytic thorium by the subtraction of $0.000\,036 \text{ kX}$ per atomic %

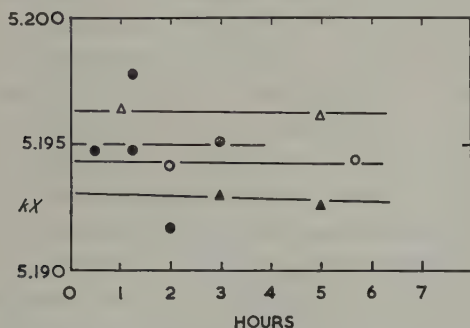


Fig. 2. Lattice spacings of an alloy containing 54.1 at % lanthanum, as a function of time and temperature of annealing of filings prepared in air and annealed in open boats.

- ▲ Filings annealed at 520°C
- Filings annealed at 620°C
- △ Filings annealed at 720°C
- Filings annealed at 820°C .

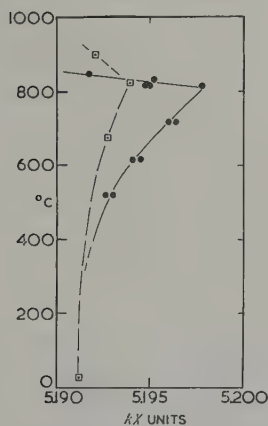


Fig. 3. Lattice spacings of an alloy containing 54.1 at % lanthanum, as a function of annealing temperature.

- Filings prepared in air and annealed in open boats
- Filings prepared under carbon tetrachloride and annealed in sealed boats.

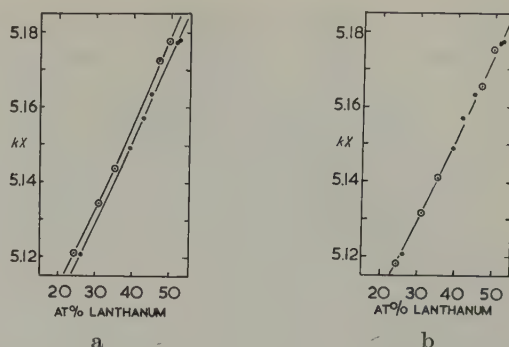


Fig. 4. Lattice spacings of alloys prepared from sintered bar and electrolytic thorium compared with those of alloys prepared from iodide thorium; (a) before correction, (b) after correction.

- Alloys prepared from sintered bar or electrolytic thorium
- Alloys prepared from iodide thorium.

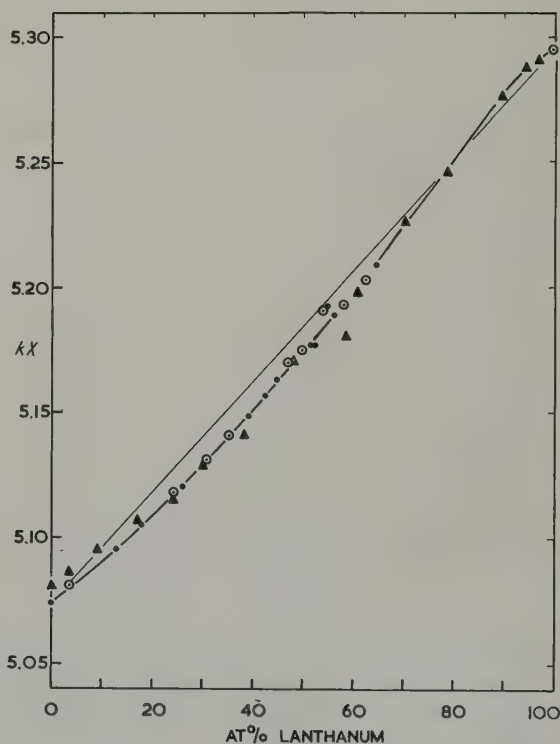


Fig. 5. Lattice spacing/composition relationships in the thorium-lanthanum system.

- Alloys prepared from iodide thorium
- Alloys prepared from sintered bar or electrolytic thorium
- ▲ Preliminary results.

thorium to obtain values strictly comparable with those for alloys containing iodide thorium. When this is done, (figs. 4b and 5), all the results obtained under stringent standard conditions (i.e. excluding the preliminary results) fall on a smooth curve, with the exception of those in the region of 50 to 60 at % lanthanum, which are referred to below.

The lattice spacing values obtained are summarized in Appendix I. No correction has been applied to the results for preliminary alloys, which are included for completeness, since the conditions under which they were obtained were not strictly comparable with those for the later work.

5. Discussion

Neglecting for the moment the results for the alloys containing 54.1 and 54.5 at % lanthanum, and the preliminary result at 58.8 at % lanthanum, the points fall on a smooth and continuous curve consistent with the existence of a complete series of solid solutions between the face-centred cubic forms of the two metals. This conclusion is supported by the results of metallographic work; all alloys examined were single phase. Of particular interest is the absence of any anomalously low region of lattice spacings between 0 and approximately 30 at % solute, as was observed for the thorium-cerium alloys. Lanthanum is predominantly 3-valent in its general chemistry and can only be transformed to a contracted form under extremely high pressures. Cerium on the other hand exhibits chemical valencies of both 3 and 4, and may comparatively easily be transformed to a contracted form, presumably by transfer of its 4f electron into a 5d orbital to give tetravalency, by the application of pressure or by cooling to a low temperature. The absence of any marked anomaly in the lattice spacing/composition curve for thorium-lanthanum alloys therefore adds weight to the suggestion¹) that in thorium-cerium alloys this valency change is induced in a proportion of the cerium atoms present, possibly by the strain energy consequent upon the introduction of the larger cerium

atoms into the thorium lattice. The work of Bates and Newman¹¹) on the magnetic susceptibilities of thorium-cerium alloys provides further evidence for promotion of the 4f electron of cerium to the conduction band.

The deviations of the lattice spacing curve from a straight line joining the spacings of thorium and lanthanum are comparatively small. The positive deviation from approximately 80 at % lanthanum to pure lanthanum may be interpreted as due to the solution of 4-valent thorium in 3-valent lanthanum; such positive deviations are common where the valency of the solute element exceeds that of the solvent¹²). Conversely the negative deviation at the thorium-rich end of the system may be due to the same factor, with the valency of the solvent exceeding that of the solute. It should, be noted that, for compositions exceeding about 40 at % lanthanum, the diffraction patterns from filings annealed in open boats contained lines due to thorium nitride, and it is probable that the lanthanum contained sufficient nitrogen to saturate the alloys in this composition range. This is supported by the recognition of nitride lines in an alloy made from thorium of very low initial nitrogen content, and containing 65 at % lanthanum. Even under the stringent conditions adopted to obtain the results summarized in fig. 5, therefore, it is probable that the curve is slightly affected by the presence of nitrogen.

The possibility of saturation with nitrogen in the alloys richer in lanthanum may explain the anomalous region between 50 and 60 at % lanthanum. If in this region there is a marked increase in the solid solubility of nitrogen, such as may be caused by a widening of the homogeneous solid solution area in the thorium-lanthanum-nitrogen system, the results obtained may be expected to be particularly sensitive to slight accidental variations in heat-treatment conditions. Thus the two high results at approximately 55 at % lanthanum probably represent somewhat more seriously contaminated material, and the lower result at 56.4 at % lanthanum, which was obtained under

stringent annealing conditions at a late stage in the investigation, is to be preferred.

The preliminary results do not agree particularly closely with the final measured spacings up to 35 at % lanthanum. Since the vacuum conditions in the annealing work were less satisfactory in these early experiments, the lack of close agreement is probably to be attributed partly to nitrogen saturation of all the filings used in preliminary work †, and partly to contamination of the filings by molybdenum from the boats originally used; the latter type of contamination may easily occur by volatilization of molybdenum oxide, which is subsequently reduced by the thorium-rich filings.

The evidence of the present work, therefore, is that thorium and lanthanum form a complete series of solid solutions, the lattice spacing/composition curve for which is smooth and continuous. Owing to the very high reactivity of the alloys, the curve shown in fig. 5 may be slightly affected by the presence of traces of nitrogen, but the consistency and reproducibility of the final results suggests that such contamination has been reduced to a minimum.

Acknowledgements

Grateful acknowledgement is made to the United Kingdom Atomic Energy Authority for the general support given to this work, and to the General Electric Company Limited, U.K., for the award of a research scholarship to one of us (D.S.E.).

† This suggestion is supported by the observation that the high values of the lattice spacing of thorium obtained in the preliminary work may be reproduced by deliberate nitrogenation of iodide thorium of spacing $a = 5.0741 \text{ kX}$.

APPENDIX 1

Lattice spacings, at 25° C, in the thorium-lanthanum system

Alloy No.	Lanthanum (at %)	Type of thorium used	Lattice spacing kX	Corrected lattice spacing kX	Remarks
20	3.6*	E	5.0854	5.0819	
P 2	10.6*	E	5.0952	—	
17	13.0	I	5.0956	—	Prep. from 18
P 3	16.0*	E	5.1070	—	
15	17.9	I	5.1055	—	Prep. from 19
P 4	24.1	E	5.1158	—	
6	24.3	S.B.	5.1210	5.1183	Prep. from 2
18	26.1	I	5.1206	—	
P 5	30.4*	E	5.1295	—	
3	30.9	S.B.	5.1343	5.1318	Prep. from 1
9	35.1	E	5.1436	5.1413	Prep. from 8
P 6	33.7	E	5.1416	—	
19	39.2	I	5.1490	—	
14	42.8	I	5.1571	—	Prep. from 12
10	44.8*	I	5.1635	—	
1	46.9	S.B.	5.1725	5.1706	
P 7	48.0*	E	5.1710	—	
8	49.9	E	5.1774	5.1756	Prep. from 7
13	51.8	I	5.1772	—	
11	52.3*	I	5.1778	—	
2	54.1	S.B.	5.1928	5.1911	
12	54.5	I	5.1930	—	
16	56.4	I	5.1890	—	
7	58.1	E	5.1953	5.1938	
P 8	53.8	E	5.1810	—	
P 9	61.0	E	5.1981	—	
5	62.7	S.B.	5.2047	5.2034	
4	64.9	I	5.2097	—	
P 10	71.4*	E	5.2269	—	
P 11	78.5*	E	5.2462	—	
P 12	89.8	E	5.2770	—	
P 13	94.4	E	5.2884	—	
P 14	97.1*	E	5.2917	—	
	100		5.2951	—	

Notes :

- (i) The symbol P in column 1 indicates a preliminary alloy.
- (ii) * denotes analysed composition in column 2.
- (iii) The symbols S.B., E, and I in column 3 refer respectively to sintered bar, electrolytic and iodide thorium.

References

- ¹⁾ R. T. Weiner, W. E. Freeth and G. V. Raynor, *J. Inst. Met.* **86** (1957-58) 185
- ²⁾ J. H. N. van Vucht, *Philips Research Reports* **12** (1957) 351
- ³⁾ A. W. Lawson and Ting-Yuan Tang, *Phys. Rev.* **76** (1949) 301
- ⁴⁾ P. W. Bridgman, *Proc. Amer. Acad. Arts and Sci.* **76** (1948) 71
- ⁵⁾ D. S. Evans and G. V. Raynor, *J. Nucl. Mat.* **1** (1959) 281
- ⁶⁾ J. P. Nelson and D. P. Riley, *Proc. Phys. Soc.* **57** (1945) 160
- ⁷⁾ A. J. C. Wilson, *Proc. Cambridge Phil. Soc.* **36** (1940) 485
- ⁸⁾ F. H. Spedding, A. H. Daane and K. W. Harman, *Acta Cryst.* **9** (1956) 559
- ⁹⁾ F. H. Spedding, A. H. Daane and K. W. Harman, *Trans. AIME* **209** (1957) 895
- ¹⁰⁾ D. Peterson and R. Mickelson, unpublished information quoted by F. A. Rough and A. A. Bauer, Battelle Memorial Institute (USA) Report, BMI-1300
- ¹¹⁾ L. F. Bates and M. M. Newman, *Proc. Phys. Soc.* **72** (1958) 345
- ¹²⁾ G. V. Raynor, *Trans. Faraday Soc.* **45** (1949) 698

FISSION FRAGMENT DAMAGE TO CRYSTAL STRUCTURES †

R. M. BERMAN, M. L. BLEIBERG and W. YENISCAVICH

Bettis Atomic Power Division, Westinghouse Electric Corporation, Pittsburgh, Pennsylvania, USA

Received 8 February 1960

Al_2O_3 and ZrSiO_4 show little change in properties when exposed to 10^{18} – 10^{19} nvt of thermal neutrons. When, however, a source of fission fragments is provided in the form of a UO_2 dispersant, the grain boundaries and the peaks of the X-ray diffraction profile disappear on irradiation. The crystal structure of U_3O_8 is also destroyed when irradiated in-pile. Al_2O_3 was observed to increase about 30 % in volume concurrent with the destruction of its crystal lattice. Calculations indicate that only a small proportion of the atoms are displaced by the fission fragment through elastic collisions or other applicable mechanisms. It is suggested that the fission fragments act indirectly, through anisotropic effects which distort the lattice and render it unstable. There are apparently a number of materials that exhibit this property; this places a serious limitation on the materials suitable for use within the range of fission fragment recoil. In contrast to this behavior, a number of ceramic materials having a cubic crystal structure exhibit excellent stability in-pile. These materials include UO_2 and $\text{UO}_2 + \text{ZrO}_2$.

Al_2O_3 et ZrSiO_4 ne subissent qu'un faible changement de leurs propriétés après exposition à un flux de neutrons thermiques de 10^{18} – 10^{19} nvt. Mais si l'on ajoute une source de fragments de fission sous la forme d' UO_2 dispersé, les contours de grain et les pics des raies de diffraction aux R.X. disparaissent après irradiation. De même la structure cristalline de U_3O_8 est détruite par irradiation en pile.

On a observé que Al_2O_3 augmente de volume d'environ 30 % en même temps que sa structure cristalline est détruite. Les calculs indiquent que seule une petite proportion des atomes est déplacée par les fragments de fission par collision élastique ou des autres mécanismes. On suggère que les fragments de

fission agissent indirectement par des effets anisotropiques qui déforment la maille et la rendent instable.

Il y a apparemment un nombre considérable de matériaux qui présentent ce phénomène, ce qui limite sérieusement les matériaux susceptibles d'être utilisés dans le domaine du recul des fragments de fission. En contraste avec ce comportement, certains matériaux céramiques de structure cristalline cubique montrent une très bonne stabilité en pile. Parmi ces derniers, on cite en particulier UO_2 et $\text{UO}_2 + \text{ZrO}_2$.

Die Eigenschaften von Al_2O_3 und ZrSiO_4 werden bei Bestrahlung mit thermischen Neutronen von 10^{18} – 10^{19} nvt nur wenig verändert. Sobald aber in Form von dispergiertem UO_2 eine Quelle für Spaltprodukte eingebracht wird, verschwinden bei Bestrahlung die Korngrenzen und die Maxima des Röntgenbeugungsdiagramms. Die Kristallstruktur von U_3O_8 wird bei Bestrahlung im Reaktor ebenfalls zerstört. Bei Al_2O_3 war zu beobachten, dass zusammen mit der Zerstörung des Kristallgitters das Volumen um 30 % zunahm. Berechnungen zeigen an, dass nur ein kleiner Bruchteil der Atome durch elastische Stöße mit den Spaltprodukten oder durch andere denkbare Vorgänge von ihren Gitterplätzen entfernt werden. Es wird daher angenommen, dass die Spaltprodukte indirekt wirken, etwa durch Anisotropieeffekte, welche das Gitter verzerren und es instabil werden lassen. Offensichtlich gibt es eine beträchtliche Zahl von Materialien mit einem solchen Verhalten, was eine schwerwiegende Begrenzung der Materialien bedeutet, die in Bereichen des Auftretens von Spaltprodukten verwendet werden können. Im Gegensatz hierzu weisen viele keramische Materialien mit kubischem Kristallgitter eine ausgezeichnete Stabilität im Reaktor auf. Zu diesen Materialien gehören auch UO_2 und $\text{UO}_2 + \text{ZrO}_2$.

1. Introduction

The experience with bulk UO_2 as the blanket fuel material for the Shippingport Plant Reactor (PWR) has led to increased interest in the

radiation stability of ceramic materials as nuclear fuels. The in-pile behavior of UO_2 has been described by Eichenberg *et al.*, and Robertson and co-workers, who have demon-

† This work was performed under AEC Contract No. AT-11-1-GEN-14.

strated the excellent irradiation stability of this material ^{1,2}). Similarly, a large body of information has been obtained on the in-pile behavior of non-fissionable ceramic materials of potential worth in nuclear technology; this has recently been reviewed by Crawford and Wittels ³). Of particular interest to this investigation is the effect of pile irradiation of Al₂O₃. Alumina has been shown to be relatively unaffected by pile irradiation; Antal and Goland concluded from the results of a study of this material after exposures of 1.19×10^{19} neutrons per cm², that alumina exhibited good crystallographic stability to fast neutron irradiation ⁴).

From these results, it would appear that a particularly attractive fuel material would be a dispersion of UO₂ in alumina. Since these two materials are mutually insoluble, the properties of the mixture were expected to be a simple combination of those of the two components. Both have excellent irradiation stability when tested alone. The overall thermal conductivity of the fuel should be increased, since the thermal

conductivity of the Al₂O₃ matrix is three times that of UO₂ at operating temperatures. Furthermore, the physical and chemical properties of Al₂O₃ are quite satisfactory since it has a low neutron cross-section, high mechanical strength, and high resistance to corrosion in hot-water environments.

Another potentially attractive fuel material would appear to be a solid solution between UO₂ and ZrO₂. About 40 mol % ZrO₂ can be accommodated in solution in the face-centered cubic structure of UO₂; while the tetragonal ZrO₂ structure can accept about 20 mol % UO₂ at sintering temperatures ⁵). These single-phase solid solutions offer the possibility of a uniform nuclear fuel with a neutron absorption cross-section somewhat lower than UO₂ alone.

The present experiments were designed to confirm the expected behavior of these and other possible ceramic fuel materials under reactor conditions, and to study the nature of the changes in physical properties that take place on irradiation.

TABLE I
Characterization of materials investigated

Composition (wt %)	Density (g/cm ³) (Pre-irrad.)	No. phases	Crystal symmetry	Unit Cell Dimensions-A.U.			Composition of phases	
				a ₀	b ₀	c ₀		
<i>Compounds</i>								
UO ₂	10.97	1	Cubic	5.469	11.97	4.150	Single pure phase	
U ₃ O ₈	8.39	1	Orthorhombic	6.717			Single pure phase	
Al ₂ O ₃	4.00	1	Hexagonal	4.758			12.99	Single pure phase
ZrSiO ₄	4.65	1	Tetragonal	6.58			5.93	Single pure phase
<i>Dispersions</i>								
Al ₂ O ₃ + 21 UO ₂	4.47	2	Cubic	5.469	11.97	12.99	Two phase — mutually insoluble	
			Hexagonal	4.758				
Al ₂ O ₃ + 80 UO ₂	8.14	2	Cubic	5.469			12.99	Two phase — mutually insoluble
			Hexagonal	4.758				
ZrSiO ₄ + 25 UO ₂	5.43	2	Cubic	5.469	6.0	6.0	Two phase — limited solubility of U in ZrSiO ₄	
			Tetragonal	6.60				
<i>Solid solutions</i>								
ZrO ₂ + 80 UO ₂	8.29	1	Cubic	5.371	11.49	7.99	Single phase	
ZrO ₂ + 13 CaO + 17 UO ₂	5.78	3	Tetragonal	4.064			3.987	ZrO ₂ with 10 wt % UO ₂ , 10 wt % CaO
			Cubic	5.220				UO ₂ with 25 wt % ZrO ₂
			Orthorhombic	11.15				CaZrO ₃

2. Experimental Techniques

2.1. SAMPLE PREPARATION

Three types of ceramic materials were investigated: compounds, solid solutions, and dispersions of insoluble or partially soluble compounds. The compositions of these materials

and their crystal structures are listed in table 1. The methods of preparation varied somewhat for the different materials, but in general was rather similar to that used for the $\text{UO}_2\text{-Al}_2\text{O}_3$ mixtures. The components were mixed and ball-milled in a rubber-lined mill, using

TABLE 2
Burnup and operating conditions

Exp. number	Sample number	Composition (wt %)	Sample dimensions (mm)	% U^{235} in Total U	Atoms U^{235} per $\text{cm}^3 (\times 10^{-20})$	Fuel surface ($^\circ\text{C}$)	Fissions/ $\text{cm}^3 (\times 10^{20})$	nvt ($\times 10^{-20}$)	Surface heat flux (watt/ cm^2)
14-27	U-6	UO_2	$15.5 \times 15.5 \times 1.02$	8.05	19.1	114	1.12	1.15	85
	A-3	$\text{Al}_2\text{O}_3 + 21 \text{UO}_2$	$15.5 \times 15.5 \times 1.02$	93.29	19.7	262	2.74	2.94	195
	U-7	UO_2	$15.5 \times 15.5 \times 1.02$	8.05	19.1	358	3.55	4.10	265
	A-4	$\text{Al}_2\text{O}_3 + 21 \text{UO}_2$	$15.5 \times 15.5 \times 1.02$	93.29	19.7	218	2.33	2.42	165
	B-1	$\text{Al}_2\text{O}_3 + 21 \text{UO}_2$	$15.5 \times 15.5 \times 1.02$	93.29	19.7	114	1.25	1.34	85
14-28	U-4	UO_2	$15.5 \times 15.5 \times 1.02$	8.05	19.1	42	1.57	1.70	31
	U-10	UO_2	$15.5 \times 15.5 \times 1.02$	8.05	19.1	150	5.12	6.15	113
	U-11	UO_2	$15.5 \times 15.5 \times 1.02$	8.05	19.1	283	8.34	11.30	210
	A-10	$\text{Al}_2\text{O}_3 + 21 \text{UO}_2$	$15.5 \times 15.5 \times 1.02$	93.29	19.7	392	10.80	15.70	290
	A-6	$\text{Al}_2\text{O}_3 + 21 \text{UO}_2$	$15.5 \times 15.5 \times 1.02$	93.29	19.7	213	6.92	8.52	157
29-10	1	$\text{Al}_2\text{O}_3 + 21 \text{UO}_2$	$25.4 \times 10.7 \times 0.97$	68.7	14.5	288	5.25	9.00	161
	2	$\text{ZrO}_2 + 13 \text{CaO} + 17 \text{UO}_2$	$25.4 \times 10.7 \times 0.97$	68.7	14.6	278	4.48	7.28	132
	3 & 4	UO_2	$25.4 \times 10.7 \times 0.97$	6.1	14.5	290	5.70	10.02	167
30-3	T04	$\text{Al}_2\text{O}_3 + 21 \text{UO}_2$	$15.5 \times 15.5 \times 2.03$	93.29	19.7	300	0.92	0.87	148
	T17	$\text{Al}_2\text{O}_3 + 21 \text{UO}_2$	$15.5 \times 15.5 \times 2.03$	93.29	19.7	300	0.92	0.87	148
	T07	$\text{ZrO}_2 + 13 \text{CaO} + 17 \text{UO}_2$	$15.5 \times 15.5 \times 2.03$	93.29	19.7	225	0.70	0.68	113
	T08	$\text{ZrO}_2 + 13 \text{CaO} + 17 \text{UO}_2$	$15.5 \times 15.5 \times 2.03$	93.29	19.7	225	0.70	0.68	113
	T01	UO_2	$15.5 \times 15.5 \times 2.03$	9.0	21.4	230	0.72	0.68	117
	T14	UO_2	$15.5 \times 15.5 \times 2.03$	9.0	21.4	230	0.72	0.68	117
BNL-4	2C	$\text{ZrO}_2 + 80 \text{UO}_2$	$15.9 \times 15.9 \times 1.27$	10.25	18.8	45	0.14	0.15	4.7
	2D	$\text{ZrO}_2 + 80 \text{UO}_2$	$15.9 \times 15.9 \times 1.27$	Depleted		40	0.0002	0.02	0.01
	3A	$\text{Al}_2\text{O}_3 + 80 \text{UO}_2$	$15.9 \times 15.9 \times 1.27$	12.25	21.3	42	0.03	0.02	1.2
	3B	$\text{Al}_2\text{O}_3 + 80 \text{UO}_2$	$15.9 \times 15.9 \times 1.27$	12.25	21.3	43	0.07	0.06	2.3
	3C	$\text{Al}_2\text{O}_3 + 80 \text{UO}_2$	$15.9 \times 15.9 \times 1.27$	12.25	21.3	45	0.26	0.15	13.9
	3D	$\text{Al}_2\text{O}_3 + 80 \text{UO}_2$	$15.9 \times 15.9 \times 1.27$	Depleted		40	0.0002	0.02	0.01
	3E	$\text{Al}_2\text{O}_3 + 80 \text{UO}_2$	$15.9 \times 15.9 \times 1.27$	Depleted		40	0.0006	0.06	0.02
	3F	$\text{Al}_2\text{O}_3 + 80 \text{UO}_2$	$15.9 \times 15.9 \times 1.27$	Depleted		40	0.0015	0.15	0.03
	5D	U_3O_8	$15.9 \times 15.9 \times 1.27$	Depleted		40	0.0001	0.01	—
	5E	U_3O_8	$15.9 \times 15.9 \times 1.27$	Depleted		40	0.0001	0.03	—
	6C	Al_2O_3	$15.9 \times 15.9 \times 1.27$	—	—	40	0	0.09	—
	11A	$\text{ZrSiO}_4 + 25 \text{ wt } \% \text{UO}_2$	$15.9 \times 15.9 \times 1.27$	0.7	0.20	40	0.0004	0.04	0.01
	11B	$\text{ZrSiO}_4 + 25 \text{ wt } \% \text{UO}_2$	$15.9 \times 15.9 \times 1.27$	0.7	0.20	40	0.0008	0.08	0.03
	11D	ZrSiO_4	$15.9 \times 15.9 \times 1.27$	—	—	40	0	0.03	—
	11E	ZrSiO_4	$15.9 \times 15.9 \times 1.27$	—	—	40	0	0.04	—

"Borundum" balls. A binder of 1 wt % 20M "Carbowax" was added, and the particles were agglomerated to facilitate pressing. The platelets were then pressed in steel dies at 14 TSI; allowance was made, in the size of the dies, for shrinkage during sintering. Samples consisting mainly or entirely of ZrSiO_4 or U_3O_8 were sintered in air for 24 hours at 1200 to 1350° C; the other materials were sintered in hydrogen for approximately 40 hours at 1760° C. The platelets were then ground to final dimensional tolerances by lapping with silicon carbide grit. Densities in excess of 95 % of the theoretical maximum were attained. The samples sizes of ceramic materials used in this investigation are shown in table 2.

2.2. IRRADIATION TECHNIQUES

Except for experiment BNL-4, the samples were encased in Zircaloy-2 and irradiated as prototype fuel elements, the fabrication of which has been described in detail elsewhere⁶). The ceramic plates of experiment BNL-4 were clamped in an aluminium sample holder. Experiments WAPD 14-27 and 28, and BNL-4, were further encased in sealed aluminum capsules. The other experiments were exposed directly to the recirculated water of high-temperature, high-pressure loops built into the Materials Testing Reactor. The loops were operated at 155 kg/cm² and 290° C.

Table 2 lists the total irradiation exposure of each sample, as integrated neutron flux and fissions/cm³, as well as heat fluxes and surface temperatures attained during irradiation. All samples were irradiated at the MTR except for those of experiment BNL-4, which were irradiated in unused fuel channels of the Brookhaven National Laboratory reactor.

2.3. POST-IRRADIATION EXAMINATION

After irradiation, the samples were returned to the Bettis "hot" laboratory, where they were opened and examined remotely. Density changes were observed both through dimensional changes, measured with remotely operated micrometers, and through the immersion

method, using water to which a few drops of "Aerosol" detergent had been added. Portions of the samples were mounted in thermosetting plastic and polished; these mounts were used both for metallography and X-ray diffraction.

X-ray diffraction data were obtained on a double-crystal spectrometer capable of obtaining a powder diffraction pattern from extremely radioactive samples. A horizontally-mounted tube provides copper K radiation. After leaving the sample, the diffracted beam traverses a bent channel in a large mass of lead brick, first to a curved lithium fluoride crystal, then to a scintillation counter. This counter is operated at a very low plate voltage, barely enough to obtain a signal from the photomultiplier tube. This makes it possible to eliminate, by means of a pulse height discriminator, the signals caused by any radiation except the copper K-alpha X-rays and those gamma rays having very similar energies. Each of these steps takes its toll in signal intensity. Therefore in order to improve the intensity, no collimation or Soller slits are used either before or after the sample, except for one slit at each end of the 21-inch lead channel. The long channel and the small port of the detector provide sufficient collimation both horizontally and vertically.

The monochromator, with its several hundred pounds of lead brick shielding, is stationary. The sample and the horizontal X-ray tube are moved during the scanning; they revolve at the proper 2:1 ratio on a rotating milling machine table, specially adapted to this purpose. The table is driven through a set of precision, low-backlash reducing gears at any one of three speeds, up or down, by remotely-operated motors. The entire assembly is housed in a steel cell with eight-inch walls.

3. Results

3.1. CHANGES IN DENSITY AND MICROSTRUCTURE

Thickness measurements were made on all prototype fuel elements after irradiation. The results are presented in table 3. It will be noted that the fuel elements which contained Al_2O_3 +

TABLE 3
Dimensional changes of Zircaloy clad fuel elements and density changes in fuel

Exp. number	Sample number	Fuel composition (wt %)	Burnup fissions/cm ³ ($\times 10^{-20}$)	Fuel element thickness (inches)			Fuel densities (g/cc)		
				Pre	Post	ΔT	Pre	Post	% ΔD
14-27	U-6	UO ₂	1.12	0.073	0.074	0.001	10.52	10.48	0.38
	A-3	Al ₂ O ₃ + 21 UO ₂	2.74	0.073	0.080	0.007	4.46	3.63	18.5
	U-7	UO ₂	3.55	0.072	0.073	0.001	10.52	10.43	0.86
	A-4	Al ₂ O ₃ + 21 UO ₂	2.33	0.072	0.080	0.008	4.46	3.57	19.9
	B-1	Al ₂ O ₃ + 21 UO ₂	1.25	0.067	0.072	0.005	4.46	3.66	17.9
14-28	U-4	UO ₂	1.57	0.073	0.073	0	10.52	10.47	0.48
	U-10	UO ₂	5.12	0.072	0.073	0.001	10.52	10.48	0.38
	U-11	UO ₂	8.34	0.073	0.074	0.001	10.52	10.45	0.67
	A-10	Al ₂ O ₃ + 21 UO ₂	10.80	0.071	0.079	0.008	4.46	3.59	19.7
	A-6	Al ₂ O ₃ + 21 UO ₂	6.92	0.072	0.080	0.008	4.46	3.62	18.8
29-10	1	Al ₂ O ₃ + 21 UO ₂	5.25	0.073	0.080	0.007	4.50	3.71	17.4
	2	ZrO ₂ + 13 CaO + 17 UO ₂	4.48	0.073	0.072	-0.001	5.55	5.55	0
	3 & 4	UO ₂	5.70	0.073	0.073	0	10.67	10.67	0
30-3	T04	Al ₂ O ₃ + 21 UO ₂	0.92	0.121	0.139	0.018	4.40	3.41	22.5
	T17	Al ₂ O ₃ + 21 UO ₂	0.92	0.123	0.136	0.013	4.40	3.69	16.3
	T07	ZrO ₂ + 13 CaO + 17 UO ₂	0.70	0.112	0.112	0	5.40	5.40	0
	T08	ZrO ₂ + 13 CaO + 17 UO ₂	0.70	0.125	0.125	0	5.40	5.40	0
	T01	UO ₂	0.72	0.120	0.120	0	10.60	10.60	0
	T14	UO ₂	0.72	0.125	0.125	0	10.60	10.60	0

NOTES: 1. Post-irradiation densities of the 14-27 and 28 fuels were calculated from measured density changes in the fuel elements.

2. Post-irradiation densities of the 29-10 and 30-3 fuels were calculated from measured changes in fuel element thicknesses.

21 wt % UO₂ showed considerable increase in thickness, whereas the fuel elements containing UO₂ and ZrO₂ + 13 wt % CaO + 17 wt % UO₂ were essentially unchanged.

Post-irradiation density measurements were made on the WAPD-14-27 and 28 fuel elements. By making the assumption that the Al₂O₃ + 21 wt % UO₂ completely filled the interior of the fuel element, it was possible to calculate post-irradiation densities of these ceramic materials. This assumption is considered valid because metallographic sections of these fuel elements showed that swelling of the Al₂O₃ + UO₂ had resulted in the elimination of all the original void volume in the fuel element interiors. The density of the UO₂ ceramic was calculated in a similar manner except that the

compartment void volume was assumed to remain constant. Post-irradiation densities of the WAPD-29-10 and WAPD-30-3 materials were calculated from the measured increases in thickness of the fuel element. These results were confirmed by direct measurement, using the immersion method, on fragments of fuel removed from the cladding in experiment 30-3. The density determinations are presented in table 3.

A decrease in density of about 18 % was noted in all Al₂O₃ + 21 wt % UO₂ materials and was found to be independent of total accumulated irradiation exposure in the range of this investigation, 0.9 to 10.8×10^{20} fissions/cc. This is illustrated in fig. 1, which shows the percentage decrease in density plotted as a function of burnup. If it is assumed that this density

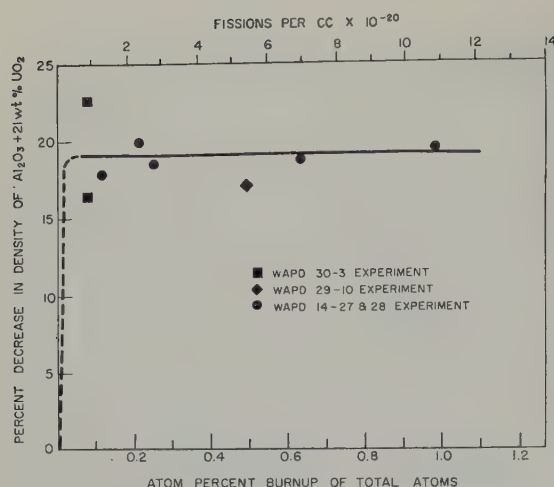
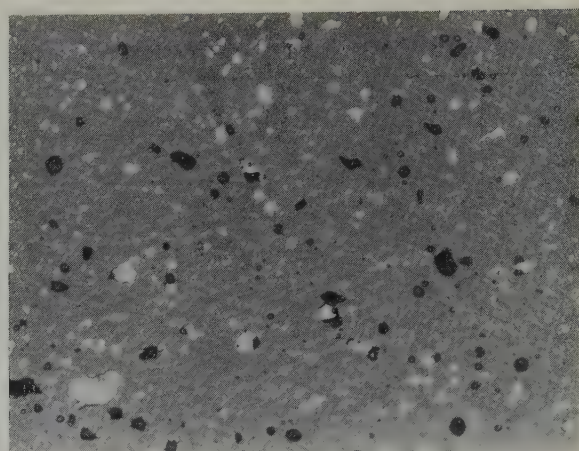


Fig. 1. Increase in volume of $\text{Al}_2\text{O}_3 + 21 \text{ wt } \% \text{UO}_2$ on irradiation.

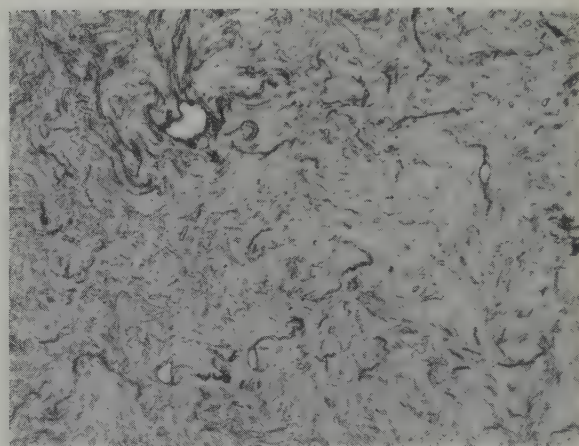
decrease is due solely to the swelling of Al_2O_3 , then the density of this compound must have decreased about 30 %, from 4.00 g/cm^3 to 3.07 g/cm^3 . This assumption is supported by the X-ray diffraction results given below.

The pronounced effect of irradiation on the $\text{Al}_2\text{O}_3 + 21 \text{ wt } \% \text{UO}_2$ ceramic fuels was also illustrated by the microstructure of this material (fig. 2). Before irradiation, the Al_2O_3 was the continuous phase and had definite grain boundaries. Particles of UO_2 and also voids were dispersed throughout this matrix. After irradiation, there is no evidence of grain boundaries in the Al_2O_3 , and the original porosity of the material has disappeared. Elongated voids and tails on the UO_2 particles were observed, suggesting that the voids had been collapsed by the swelling of the Al_2O_3 , and that the Al_2O_3 had been compressed around the UO_2 particles.

The change in microstructure of the $\text{ZrO}_2 + 13 \text{ wt } \% \text{CaO} + 17 \text{ wt } \% \text{UO}_2$ is shown in fig. 3. The phase consisting largely of UO_2 (grey particles) exhibited a "halo" effect at interface boundaries after irradiation. This darkening of the interfacial area around the particles may be attributed to fission fragment damage to the tetragonal zirconia phase, although it appears to be much smaller than the calculated range of fission fragments in this material. Unlike the $\text{Al}_2\text{O}_3 + \text{UO}_2$, no changes in porosity are ob-



As fabricated $\times 500$.



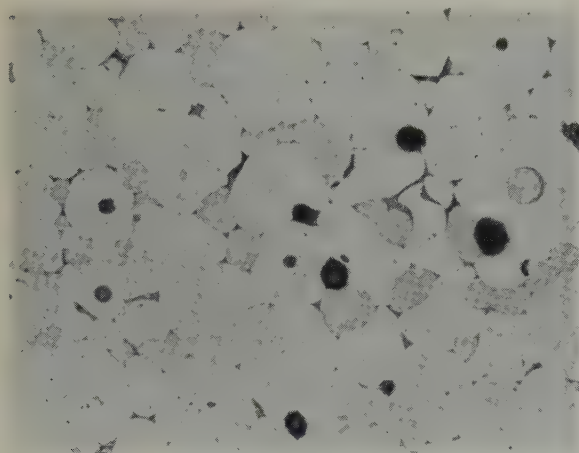
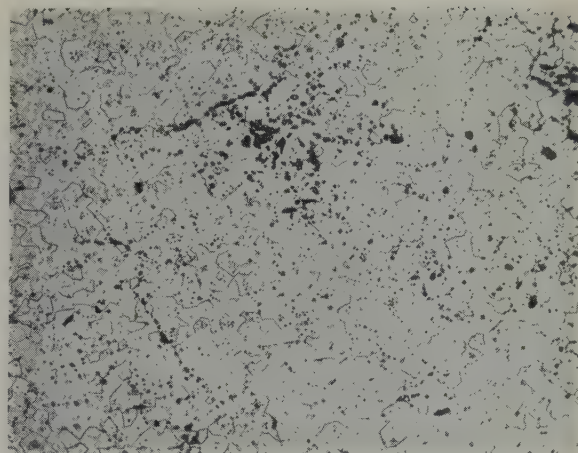
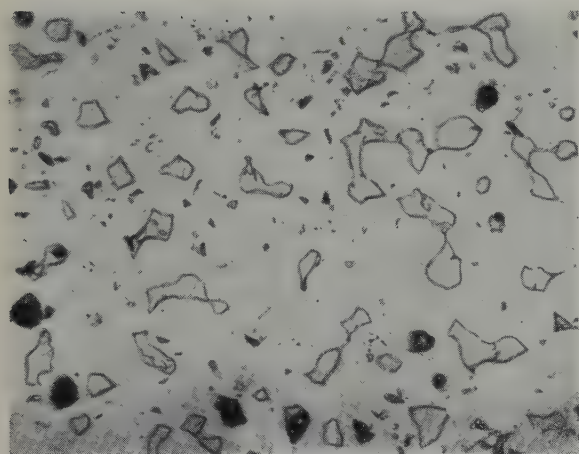
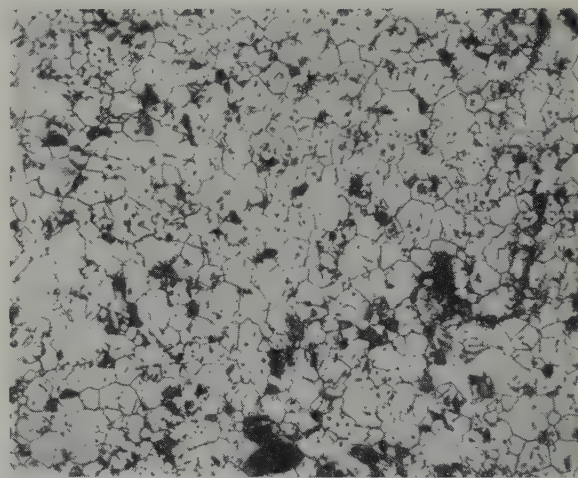
10.8×10^{20} fissions/cc. $\times 500$.

Fig. 2. $\text{Al}_2\text{O}_3 + 21 \text{ wt } \% \text{UO}_2$ fuel structure before and after irradiation.

served. The UO_2 showed no change in microstructure with exposures as high as 8.34×10^{20} fissions/ cm^3 , except for slight cracking within particles; photomicrographs of UO_2 before and after irradiation are presented in fig. 4. This is consistent with the observations of other workers¹).

3.2. X-RAY DIFFRACTION RESULTS

X-ray diffraction profiles obtained on the double-crystal spectrometer from irradiated and unirradiated materials are shown in fig. 5. Copper K_α radiation was used. Before irradiation, the $\text{Al}_2\text{O}_3 + \text{UO}_2$ mixtures gave the X-ray diffraction profile shown in fig. 5a. As expected, the

As fabricated. $\times 260$.As fabricated UO_2 . $\times 160$. 4.5×10^{20} fissions/cc. 21 at % U fissioned. $\times 260$.Fig. 3. $\text{ZrO}_2 + 13 \text{ CaO} + 17 \text{ UO}_2$ fuel structure before and after irradiation. 8.34×10^{20} fissions/cc. $\times 160$.Fig. 4. UO_2 fuel structure before and after irradiation.

diffraction profiles of UO_2 and Al_2O_3 are superimposed. After 2×10^{16} fissions per cubic centimeter, obtained by placing the sample for four weeks in a flux of approximately 10^{12} thermal neutrons per cm^2 at Brookhaven National Laboratory, the material gives the diffraction profile shown in fig. 5b. Only the peaks produced by the UO_2 particles are observed. If the peaks of the Al_2O_3 had been as much as one-twentieth ($\frac{1}{20}$) as intense after irradiation as before, they would have been detected on the instrument. The peaks produced by the UO_2 show only a slight decrease in intensity and increase in

breadth; there is also a barely significant increase, of about one part in 1000, in the linear dimensions of the unit cell. Therefore, it can be assumed, for purposes of calculation, that all the observed swelling occurs in the Al_2O_3 . A similar diffraction profile was obtained on a sample of $\text{Al}_2\text{O}_3 + 21 \text{ wt } \% \text{ UO}_2$ (sample T04 of test 30-3) after 0.92×10^{20} fissions/ cm^3 . The disappearance of the X-ray diffraction profile of Al_2O_3 cannot be ascribed to the disappearance of the phase itself through solution, for the photomicrographs (fig. 2) show quite clearly that both phases are still present after irradiation. From

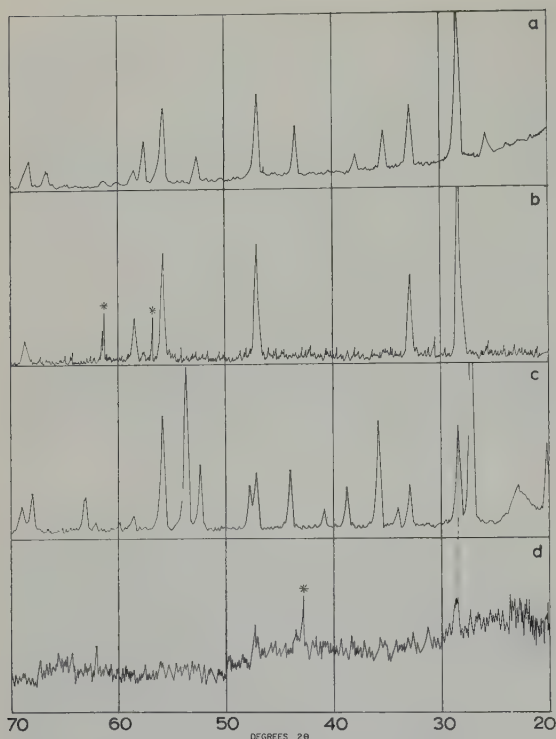


Fig. 5. Diffraction patterns obtained with copper $K\alpha$ X-rays. a) $\text{Al}_2\text{O}_3 + 80 \text{ wt } \% \text{UO}_2$, unirradiated; b) after 2×10^{16} fissions/cc. c) $\text{ZrSiO}_4 + 25 \text{ wt } \% \text{UO}_2$, unirradiated; d) after 4×10^{16} fissions/cc.

* — Non-reproducible bursts of noise.

these results it must be concluded that the crystal lattice of Al_2O_3 has been destroyed due to the irradiation.

Zircon (ZrSiO_4) is sometimes found in an amorphous state in nature. These zircons, called "metamict", contain small amounts of uranium and/or thorium. The destruction of their crystalline structure has been ascribed to the resulting irradiation of the zircon by alpha recoils through geologic time⁷). To explore the possibility that the $\text{Al}_2\text{O}_3 + \text{UO}_2$ was being rendered amorphous by a process analogous to metamictization, plates of $\text{ZrSiO}_4 + \text{UO}_2$ were irradiated to comparable exposures. Fig. 5c shows the diffraction profile of this material before irradiation; once again, except for some minor shifts ascribed to solid solution, the profile consists of the UO_2 peaks superimposed on the ZrSiO_4 peaks. Fig. 5d shows the dif-

fraction profile after irradiation. Note that the strongest surviving peak, at $28.5^\circ 2\theta$, corresponds not to the very strong ZrSiO_4 peak at 27° , but to the much smaller UO_2 peak immediately to its left in fig. 5c. The ZrSiO_4 peaks, like the $\text{Al}_2\text{O}_3 + \text{UO}_2$, have completely disappeared and three broad maxima are observed at approximately 25° , 45° and $65^\circ 2\theta$. This is similar to the appearance of the X-ray diffraction profile of a liquid or glass, particularly one containing heavy atoms.

Control samples of Al_2O_3 and ZrSiO_4 without uranium were exposed to comparable or greater amounts of neutron bombardment. The diffraction peaks of the ZrSiO_4 broadened slightly, and there was a slight expansion of the unit cell, which confirms the results reported by Crawford and Wittels³). The Al_2O_3 showed no significant change whatsoever in its diffraction profile. This result is confirmed by the work of Antal and Goland who reported only trifling effects on exposure of Al_2O_3 to integrated fast neutron fluxes about 50 times as great⁴).

Boyko, Halteman and Roof report the disappearance of the diffraction profile of U_3O_8 on irradiation⁸). This experiment was repeated herein, using depleted uranium. The least-irradiated U_3O_8 sample, number 5D of experiment BNL-4, underwent only about $\frac{1}{200}$ of the number of fissions per unit volume as the samples of Boyko, Halteman and Roof. After irradiation, the sample failed to show even the few, weak, residual diffraction peaks that they observed. A possible explanation is that their samples reached a somewhat higher temperature during irradiation, and had partially annealed themselves, while in this work, the temperature of the U_3O_8 did not exceed 75°C and no such annealing occurred. The X-ray profile shows broad maxima similar to those observed in the samples of $\text{ZrSiO}_4 + \text{UO}_2$ described above.

It can be seen in fig. 5 that the crystal structure of UO_2 was not destroyed by the irradiation. In contrast to the Al_2O_3 , its properties after irradiation did not differ in any significant way from those of UO_2 irradiated alone. After a very slight amount of irradiation,

the unit cell dimension a_0 has expanded from 5.469 Å to 5.475 Å. This value is reached by the time 2×10^{16} fissions per cm^3 have accumulated. Thereafter, no change in unit cell size has been found. The cell size calculated from the UO_2 profile obtained from sample T04, after nearly 10^{20} fissions per cm^3 , was still $5.475 \text{ Å} \pm 0.003$.

In the cubic solid solutions of ZrO_2 in UO_2 , this initial expansion of the unit cell is observed. After 2×10^{16} fissions/ cm^3 , the cell edge has increased from 5.371 to 5.382 Å. A considerable increase in the breadth of the peaks was observed. On further irradiation, the breadth of the peaks decreases to a value slightly above that for unirradiated material. The cell size, instead of remaining constant as in UO_2 , decreases somewhat; from sample 2C of experiment BNL-4, which had undergone 1.4×10^{19} fissions/ cm^3 , a sharp diffraction profile of a single cubic phase was obtained. The cell edge was $5.343 \text{ Å} \pm 0.002$. Studies are continuing on this and other cubic UO_2 solid solutions. In each case, the diffraction profile of a cubic structure has been obtained after irradiation. The cubic CaF_2 -type structure of these materials is apparently very resistant to destruction by irradiation.

4. Discussion

When sintered bodies consisting of fine-grained mixtures of alpha Al_2O_3 and UO_2 are irradiated in a reactor, the crystal structure of the Al_2O_3 is destroyed. This occurs after extremely small amounts of reactor exposure and is shown by the disappearance of the X-ray diffraction profile and also the grain boundaries of the Al_2O_3 . Concurrently, the volume of the Al_2O_3 increases about 30 %. After this initial swelling, the density of the material does not change significantly with additional exposure.

This expansion would be a serious difficulty if $\text{Al}_2\text{O}_3 + \text{UO}_2$ dispersions were to be used as a nuclear fuel since it could cause constriction of the coolant channels and perhaps rupture of the cladding.

The crystal structure of Al_2O_3 shows excellent stability when exposed to neutrons alone.

Al_2O_3 has been irradiated by Antal and Goland to 1.19×10^{19} nvt (fast). For comparison, some of the samples of experiment BNL-4 received integrated fluxes of 1×10^{18} nvt (thermal) and perhaps $\frac{1}{10}$ that number of fast neutrons. Antal and Goland report that approximately 0.12 % of the atoms are displaced at this high neutron exposure, as compared to the expected 5.5 %, calculated on the basis of the theoretical formulae of Kinchin and Pease⁹). They conclude that the crystal structure of Al_2O_3 is particularly resistant to destruction by neutrons.

The destruction of the Al_2O_3 lattice must therefore be ascribed to fission fragments. Clearly, the effect of fission fragments on these ceramic materials cannot satisfactorily be estimated by extrapolation from results obtained with other particles such as neutrons and alpha particles. Furthermore, materials show wide variability in their tendency to become amorphous under the action of fission fragments. UO_2 , $\text{ZrO}_2 + \text{UO}_2$, and $\text{ZrO}_2 + \text{CaO} + \text{UO}_2$ exhibited remarkable stability in-pile. Excellent X-ray diffraction profiles were obtained from these samples after irradiation.

A behavior similar to that of Al_2O_3 was noted in ZrSiO_4 , which shows little change upon exposure to thermal neutrons at the exposure levels used in this investigation. When it is exposed to fission fragments, however, its crystal structure is rapidly destroyed. The crystal structure of U_3O_8 is also destroyed when irradiated to comparable exposures in a reactor. Similarly, Bleiberg and Jones reported the disappearance of the X-ray profile and grain boundaries of U_3Si after an exposure of 1.06×10^{19} fissions/ cm^3 . They also observed a decrease in density of 3.8 % in this material¹⁰).

Wittels and Sherill have found that certain materials can be rendered amorphous by fast neutrons alone¹¹). These include various stable and metastable crystalline forms of SiO_2 (except Coesite), which give no diffraction profile after exposure to 1.2×10^{20} nvt (fast). These exposures are on the order of 100 times those in the present experiment. In the case of quartz, the effect of the neutron bombardment

was an anisotropic structure change. The axial ratio c/a increased with increasing exposure, until the point was reached at which the structure became unstable and the material became amorphous. It may be postulated that fission fragments have a similar effect on the structures of ZrSiO_4 , Al_2O_3 , U_3O_8 and U_3Si , since none of these materials are isometric. In CaF_2 -type structures such as UO_2 , on the other hand, the three mutually perpendicular axes have identical properties, and these materials do not become amorphous under fission fragment bombardment. This supposition was explored by calculating the number of displaced atoms caused by the fission fragments in this material.

Using values obtained by Suzor¹²⁾ for the range of fission fragments in aluminium foils, and assuming that the stopping power of an atom is proportional to the square root of its atomic number, it is possible to calculate that the maximum range of a Zr^{97} fragment in amorphous Al_2O_3 is 12.7 microns. Inspection of the photomicrographs (fig. 2) shows that this range is adequate to reach virtually all of the Al_2O_3 from the UO_2 particles in the material prepared for this investigation. Since the fission fragments have sufficient range to affect the entire Al_2O_3 matrix, the question arises whether the fragments can disrupt the structure directly by displacing its constituent atoms, or whether they must work through some indirect mechanism such as anisotropic expansion of the lattice. In the case of sample 3D of experiment BNL-4, it was shown that after 2×10^{16} fissions/cm³, the crystal structure of Al_2O_3 was completely destroyed. Assuming that two fission fragments were produced in each fission and that all the fragments penetrated the Al_2O_3 , then each fission fragment must be responsible for affecting a volume of Al_2O_3 containing 1.18×10^6 atoms. This can be compared to the number of displacements produced by a fission fragment, which may be calculated using the method of Kinchin and Pease^{9,13)}.

These calculations have been made for two fission fragments near the lighter and heavier maxima of the fission fragment distribution

curve. A Zr^{97} fragment with an initial energy of 93 MeV will displace approximately 215 aluminum and 360 oxygen atoms before being brought to rest. These atoms, in general, will have enough energy to displace others. In the case of the aluminum atom, the mean number of displacements per primary collision would be 35; in the case of the oxygen atom, 21. A Zr^{97} fragment with its entire path in Al_2O_3 would therefore displace about 15 000 atoms. Repeating this calculation for a Cs^{137} fragment with an initial energy of 63 MeV, one finds that 29 600 atoms are displaced. The mean value for all fission fragments would therefore be about 22 000, if their entire paths lay in Al_2O_3 . Sample 3D, however, is only 40.7 % Al_2O_3 by volume; the actual mean number of atoms in Al_2O_3 displaced through collisions with a fission fragment, or with another atom carrying a portion of the fission fragment's energy, could hardly exceed 9000, or one atom in 130. It is, of course, not necessary to displace every single atom to destroy a structure, but the number of displacements seems too low to account for the disappearance of the structure due to collision displacements. Antal and Goland⁴⁾ performed similar calculations on Al_2O_3 irradiated with fast neutrons; they obtained a value of 5.5 % of the atoms displaced. Since the structure of their material was still intact, and it showed only a slight swelling, they estimated the actual number of displacements as 0.12 %. It must be concluded that the actual number of atoms moved from the lattice sites through the action of fission fragments is far greater than theory would predict; for neutrons, in the case of Al_2O_3 , it is far less. This illustrates the difficulty of extrapolating results obtained with lighter particles to the case of fission fragments.

Monoclinic ZrO_2 has a distorted CaF_2 structure. Wittels and Sherrill¹⁴⁾ have found that natural ZrO_2 containing small amounts of uranium is converted to the cubic form, with an undistorted CaF_2 structure, on irradiation. They have also observed that uranium-free ZrO_2 was not transformed by comparable amounts of irradiation with neutrons alone. The results are

analogous to those reported for Al_2O_3 and ZrSiO_4 , except that the irradiation resulted in the extremely stable CaF_2 -type structure rather than an amorphous phase. The density of fission events was roughly the same as that in sample 3D of experiment BNL-4. The calculations performed by Wittels and Sherrill, therefore, gave results closely comparable to those above; it was necessary for each fission fragment to convert to the cubic form a volume of ZrO_2 containing 10^6 atoms, but the number of displacements calculated was on the order of two magnitudes less.

Wittels and Sherrill attributed the results observed in ZrO_2 to fission or displacement spikes, which have been shown to be adequate to cause the phase reversal noted in U-9 wt % Mo alloy¹⁵). Walton¹³) calculates that a heavy fission fragment will displace 5.5×10^4 atoms of uranium metal by momentum transfer. In U-9 wt % Mo, according to Bleiberg, the displacement spike, formed after the energy of the particle has dropped below the range in which Walton's mechanism is effective, will affect an additional 6×10^4 atoms¹⁵). In lighter materials, however, the displacement spike does not begin to form until only an infinitesimal portion of the energy of the fission fragment remains. Brinkman calculates this threshold value to be 9000 eV in the case of metallic zirconium and 1200 eV in the case of aluminum¹⁶). The values for the oxides would be even less. Therefore, it does not seem reasonable to attribute the effects noted herein to displacement spikes.

In Al_2O_3 , approximately 99 % of the energy of the fission fragment is dissipated through ionization. Varley¹⁷) suggests that this portion of the energy might account for some displacements in ionic crystals, by converting negative ions into positive ones, which would then be repelled from their position in the lattice by the surrounding positive ions. It is plainly not sufficient for an ion to be expelled into a neighboring vacancy; it would simply return to its original position when it regained its electrons. A fairly high positive charge is therefore necessary; let us assume that there will be

one of these "multiple ionization" displacements for every oxygen ion reaching an oxidation state of +3, i.e. losing 5 of its 10 electrons. Since the total amount of energy dissipated by the fission fragment is known, as well as the energy necessary for a single ionization, it can be calculated that about 5×10^6 oxygen ions lose a single electron as a 93-MeV particle passes through Al_2O_3 . Varley estimates that the cross-section decreases an order of magnitude with each additional electron removed from the same atom; this would result in only about 500 oxygen ions reaching the charge of +3. This mechanism applies only in the case of ionic materials; it cannot contribute significantly to the number of displacements in ZrSiO_4 , which is largely covalent, or in U_3Si , in which the bonds are metallic.

There remains the hypothesis that the fission fragments act indirectly, through anisotropic effects which distort the lattice, and render it unstable. On this assumption, it may be possible to draw up a tentative list of criteria for the likelihood of fission-fragment-induced phase changes in a particular substance.

The first requirement is that the substance be anisotropic. All of the materials showing fission-fragment-induced phase changes are anisotropic. The CaF_2 -type cubic materials do not show these changes. Marked anisotropy of macroscopic physical properties, particularly reactions to thermal and mechanical stresses, may also be a useful criterion.

The presence of high-temperature or metastable allotropic forms obtainable by ordinary chemical means might also indicate that the structure is comparatively unstable. Al_2O_3 has a metastable gamma form, and SiO_2 has many metastable forms as well as five stable crystalline phases. U_3O_8 has a high-temperature form and a closely related $\text{UO}_{2.6}$ phase slightly deficient in oxygen.

The existence of more than one stable configuration between an ion and its nearest neighbors indicates that the structure may be unstable. In Al_2O_3 , each aluminium ion is surrounded by six oxygen ions; in many silicates,

however, it is surrounded by four. Likewise, zirconium may occur in six or eight co-ordination with oxygen. This occurs when the ratio between the ionic radii of the two ions is close to the theoretical stability limit between two co-ordination numbers.

However, as Primak¹⁸⁾ points out, the determining factor may not be the initial state of the material, but the stability of the amorphous (or metamict) phase once it is formed. Since this cannot readily be predicted, it will continue to be necessary to test carefully, under closely-simulated operating conditions, each material proposed for placing within, or in contact with, nuclear fuel.

5. Conclusions

The results of this investigation indicate that there is a large group of substances that cannot be used for applications within the range of fission fragment recoil because their structure would be destroyed, with consequent deterioration of their macroscopic physical properties. This constitutes a serious limitation on the choice of materials for certain nuclear applications. It has been shown that this property cannot be predicted from the damage produced by neutron bombardment. As a result, two materials with satisfactory resistance to irradiation damage when irradiated alone may be unsatisfactory when mixed if one of them produces fission fragments.

Calculation indicates that the number of atoms displaced by fission fragments is insufficient to account for the destruction of the crystal structure directly. It seems probable that the structures most readily destroyed are anisotropic; none of the substances rendered amorphous artificially are cubic. It is suggested that the effects of bombardment on the crystal structure are anisotropic, and render the structure unstable by distorting it.

The fact that ZrSiO_4 (zircon) is among the substances that can be rendered amorphous artificially suggests that the phenomenon may be analogous to metamictization in naturally occurring minerals.

Acknowledgement

The authors wish to thank Dr. B. Lustman for his many helpful suggestions and his encouragement throughout the course of this investigation. Invaluable technical assistance was rendered by R. Etchison, F. Susko, and R. Gray. The authors are grateful to the Westinghouse Electric Corp. and the U.S. Atomic Energy Commission for permission to publish this work.

References

- 1) J. D. Eichenberg, P. W. Frank, T. J. Kisiel, B. Lustman and K. H. Vogel, Westinghouse Atomic Power Division (USA) Report WAPD 183 (1957)
- 2) J. A. L. Robertson, A. S. Bain, A. H. Booth, J. Howieson, W. G. Morison and R. F. S. Robertson, Second Geneva Conference on Peaceful Uses of Atomic Energy **6** (1958) 655
- 3) J. H. Crawford and M. C. Wittels, First Geneva Conference on Peaceful Uses of Atomic Energy **7** (1954) 654
- 4) J. J. Antal and A. N. Goland, Phys. Rev. **112** (1958) 103
- 5) N. M. Voronov, E. A. Voitekova and A. S. Danilin, Second Geneva Conference on Peaceful Uses of Atomic Energy **6** (1958) 221
- 6) J. Glatter, E. F. Losco, W. J. Hurford, J. S. Theilacker, R. L. Fischer, N. T. Saunders and R. A. Wolfe, Second Geneva Conference on Peaceful Uses of Atomic Energy **6** (1958) 630
- 7) A. Pabst, Am. Min. **37** (1952) 137
- 8) E. R. Boyko, J. D. Eichenberg, R. B. Roof, Jr. and E. K. Halteman, Bettis Technical Review, WAPD-BT-1958 (1958) 128
- 9) G. H. Kinchin and R. S. Pease, Reports on Progress in Physics **18** (1955) 1
- 10) M. L. Bleiberg and L. J. Jones, Trans. Met. Soc. AIME **212** (1958) 758
- 11) M. C. Wittels and F. A. Sherrill, Phys. Rev. **93** (1954) 1117
- 12) F. Suzor, C.R. Acad. Sci. **226** (1948) 1081
- 13) G. N. Walton, Progress in Nuclear Physics **6** (1957) 192
- 14) M. C. Wittels and F. A. Sherrill, Phys. Rev. Ltrs. **3** (1959) 176
- 15) M. L. Bleiberg, J. Nucl. Mat. **1** (1959) 182
- 16) J. A. Brinkman, J. Appl. Phys. **25** (1954) 961
- 17) J. H. O. Varley, Progress in Nuclear Energy **5** (1956) 672
- 18) W. Primak, Phys. Rev. **95** (1954) 837

RECRYSTALLIZATION OF DEFORMED ALPHA-URANIUM SINGLE CRYSTALS

LOWELL T. LLOYD

Argonne National Laboratory, Argonne, Illinois, USA

Received 7 March 1960

The orientation relationship between deformed and recrystallized alpha-uranium can be expressed as 27.5° rotations about axes located 70.0° from the [100], 63.5° from the [010] and 34.0° from the [001]. In deriving this relationship it was necessary to consider the recrystallized grains found upon annealing deformed single crystals as originating from twins as well as from the parent crystal. Comparisons of deformation and recrystallization textures of polycrystalline uranium agree well with the finding.

Les relations d'orientation entre monocristaux d'uranium α déformés et cristaux de recristallisation peuvent être représentées par des rotations de $27,5^\circ$ autour d'axes situés à 70° de [100], $63,5^\circ$ de [010] et 34° de [001]. Pour obtenir cette relation d'orientation, il était nécessaire de supposer que les cristaux de recristallisation formés par recuit des monocristaux

déformés provenaient aussi bien des macles de déformation de l'uranium que du monocristal initial. Les comparaisons entre textures de déformation et de recristallisation de l'uranium polycristallin montrent un bon accord avec les relations d'orientation trouvées.

Der Orientierungszusammenhang zwischen verformtem und rekristallisiertem α -Uran kann als Rotationen um $27,5^\circ$ um Achsen ausgedrückt werden, die mit [100], [010] und [001] Winkel von $70,0^\circ$, $63,5^\circ$ bzw. $34,0^\circ$ bilden. Um diesen Zusammenhang abzuleiten, war zu berücksichtigen, dass die rekristallisierten Körner, die nach dem Glühen verformter Einkristalle zu beobachten waren, sowohl von Zwillingen als auch vom Mutterkristall stammen. Vergleiche von Verformungs- und Rekristallisationstexturen von polikristallinem Uran erbrachten eine gute Übereinstimmung mit dem vorliegenden Befund.

1. Introduction

The orientation relationships found between deformed single crystals and grains grown in them by annealing have contributed significantly to the knowledge of recrystallization textures for face-centered-cubic¹⁻³) and body-centered-cubic^{4,5}) metals. Normally the structures are related by rotations about axes perpendicular to the most densely populated planes. The same relationships apply to comparisons of deformation and recrystallization textures of polycrystalline materials⁶⁻⁸).

Preferred orientation data have been reported for deformed and recrystallized uranium rods⁹⁻¹³) and sheets^{14,15}) treated in the orthorhombic alpha phase temperature range. These consist of several components and exhibit appreciable scatter; consequently, it is impossible to arrive at a recrystallization orien-

tation relationship from the texture data. In view of the agreement for single crystals and polycrystalline samples of cubic materials, it was believed that recrystallization studies of deformed single crystals could delineate the orientation relationship for alpha-uranium.

2. Experimental Work

The single crystals used in this work were prepared by the grain coarsening technique described by Fisher¹⁶) and their deformations have been reported by Lloyd and Chiswick¹⁷). Anneals were performed in lead pot furnaces after sealing individual, tantalum wrapped samples in evacuated Vycor capsules. Orientations of residual deformed material and recrystallized grains were determined from X-ray Laue back-reflection photograms taken on surfaces prepared metallographically after

Fig. 2 shows recrystallized grain (001) poles grouped near the deformed crystal (001) pole †. Less distinct, but still definitive, (100) pole groups are found near {110} poles of the crystal and its {130} twins. This suggested that the grains might be related to deformation twin orientations as well as to the parent crystal. To test the hypothesis, the principal poles of the grains believed to originate from {130} twinned material were stereographically reflected on the twin planes and considered as if they originated from the parent crystal.

Further stereographic grouping was possible by reflecting the grain orientations on the principal planes of the deformed crystal so that all points from equivalent locations were plotted in single groups. The data for sample *A* after the treatments are shown in fig. 3. By expressing the location of the poles of the recrystallized grains in terms of longitude and latitude angles, it was possible to determine a mean position for each group. The great circles represent the loci of rotation axis for the pairs of principal pole positions, and their intersection is the common

axis. Four axes are possible; however, three require large rotations to bring the orientations into coincidence, while rotation for the one selected here was much smaller.

The data for the other five samples were treated in a similar manner. Of seventy five grains analyzed only four could not be referred simply to deformed orientations available in the crystals. Possibly these were related to cases where secondary twins are created within primary twins; such orientations were not considered. Table 1 indicates the number of

TABLE 1

Recrystallized grains considered to originate from deformed orientations present in alpha-uranium single crystals

Sample	Operative deformation mechanisms		Number of grains related to **	
	Slip system	Twin plane *	Twin orientation	Parent crystal
<i>A</i>	—	(130)	9	14
		($\bar{1}\bar{3}0$)	1	
<i>E</i>	{011}—[100] ?	\approx (176)	5	0
		\approx ($\bar{1}\bar{7}6$)	3	
		(130)	3	
		\approx ($\bar{1}\bar{7}6$)	2	
		\approx ($\bar{1}\bar{7}6$)	0	
<i>J</i>	(010)—[100]	($\bar{1}\bar{3}0$)	2	1
		\approx ($\bar{1}\bar{7}2$)	2	
<i>P</i>	(010)—[100]	(130)	4	5
		($\bar{1}\bar{3}0$)	5	
		\approx ($\bar{1}\bar{7}2$)	0	
		\approx ($\bar{1}\bar{7}2$)	1	
<i>S</i>	(010)—[100]	(130)	2	1
		($\bar{1}\bar{3}0$)	5	
<i>V</i>	(010)—[100]	($\bar{1}\bar{3}0$)	1	2
		\approx ($\bar{1}\bar{7}2$)	3	

* Twin planes are arranged in order of decreasing importance as operative deformation mechanism.

** Three grains in sample *A* and one grain in sample *P* were not related simply to available deformed orientations.

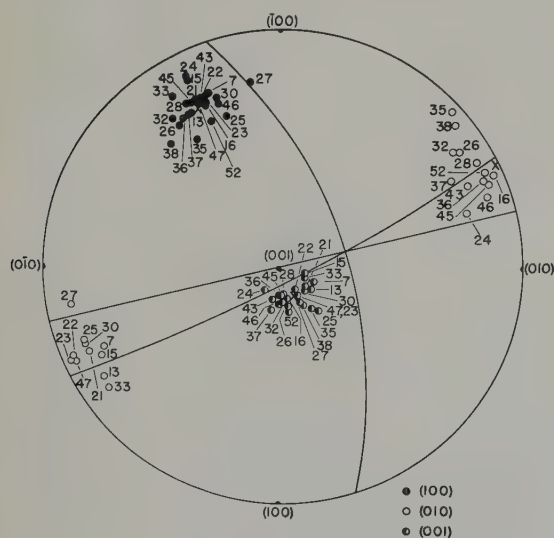


Fig. 3. Final grouping of principal poles of recrystallized grains for sample *A*. Average position for each group is indicated as "X" and rotation axis is located at the intersection of the three great circles.

† Since the (001) is the shear plane for {130} twins, the (001) poles of the parent crystal and its {130} twins coincide.

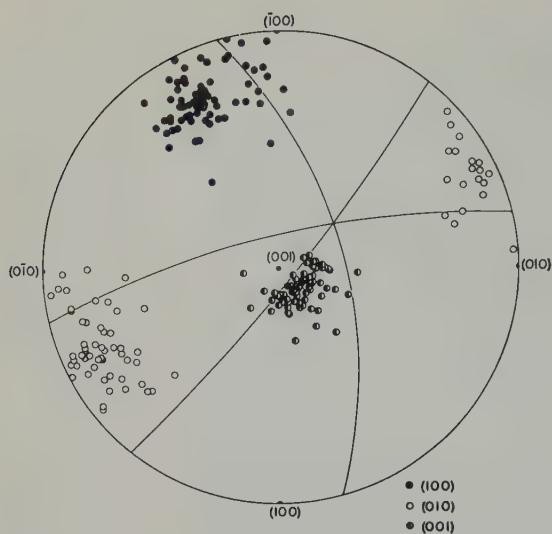


Fig. 4. Grouping of principal poles of recrystallized grains for six crystals deformed in compression.

grains assumed to originate from the various deformed orientations, and fig. 4 shows the final groupings. The average rotation axis was located 70.0° from the $[100]$, 63.5° from the $[010]$ and 34.0° from the $[001]$. A rotation of 27.5° was necessary to bring the orientations into coincidence. Four equivalent axes exist in alpha-uranium; rotation about those in the first and third quadrant was clockwise, and rotation for the second (shown in fig. 4) and fourth was counterclockwise.

4. Discussion

The primary criterium employed in treating the data was that recrystallized grains originated from the deformed orientation whose (001) pole lay near the grains' (001) pole. To fix the relationship in three dimensional space, it was assumed that the (100) pole of a recrystallized grain took up a position near a $\{110\}$ pole of the deformed orientation. The interesting aspect was the referral of grains to twin orientations as well as to the parent crystal. As can be seen from table 1, the correspondence between the twins necessary to explain the grains and those occurring upon deformation was extremely good. Moreover, the number of grains ascribed to a specific twin agrees reasonably well with its

relative importance as a deformation mechanism.

Unfortunately grains were not obtained in crystals deformed exclusively by slip, where they should be related to the crystal orientation only. The apparatus used in the compression studies was fitted with one compression platen free to move in a direction normal to the load, and end restraints were minimized. Samples deformed by slip alone would not be expected to recrystallize since the deformations approached pure shear.

Calais, Lacombe and Simenel¹⁸⁾ have reported orientation data for grains grown in a single crystal deformed by (010) kinking; the orientations were related to the deformed crystal only. The authors also gave results for samples deformed primarily by $\{130\}$ or $\{112\}$ twinning. The data for five samples were subjected to stereographic treatment like that for the present work; final groupings are shown in fig. 5. The average rotation axis was located 82.5° from the $[100]$, 52.5° from the $[010]$ and 38.5° from the $[001]$, with a rotation magnitude of 19° . These are in fair agreement with the present work. In treating the data, some twin orientations other than those recorded as operative had to be assumed; from the tensile deformation directions, the orientations con-

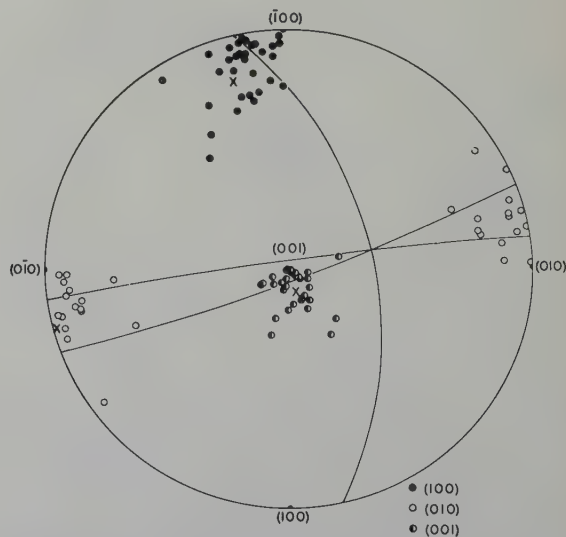


Fig. 5. Grouping of principal poles of recrystallized grains for five crystals deformed in tension¹⁸⁾

sidered were reasonable. It is gratifying to find substantial agreement for the two sets of data. This argues strongly for the validity of the method for treating the data and, particularly, for the procedure of considering recrystallized grains to originate from twinned material.

To check the applicability of the orientation relationship to polycrystalline materials, recrystallization textures constructed from deformation textures and the relationship have been compared with those reported for the material. The agreements found were good; two works are of particular interest.

The only quantitative fiber texture data are those of Jetter and McHargue¹³) who reported 70 volume per cent of the structure associated with the major deformation component and 30 % with the minor. After annealing, 65 % of the structure was associated with the major recrystallization component and 35 % with the minor. Upon applying the recrystallization relationship to the deformation texture components, it was found that part of the major recrystallization texture was supplied by the minor deformation component and the rest was supplied by half of the major deformation component. The remaining half of the major deformation component supplied the minor recrystallization component. The percentage of the constructed recrystallization components agree exactly with the reported amounts.

Mueller, Knott and Beck¹⁴) reported deformation and recrystallization textures for uranium sheet. The author's ideal components are depicted graphically in fig. 6 with respect to rolling direction (R.D.) and plane of the sheet (plane of the paper). The deformation components are shown in the upper left quadrant; their identities are given by the indicated principal pole symbols and by numbers. The positions are not depicted in true spatial relationship; however, the representation is sufficient since the sheet was rolled so as to make the data symmetrical about the transverse and rolling directions. One principal pole of the ideal recrystallization components are plotted in each of the other three quadrants. The

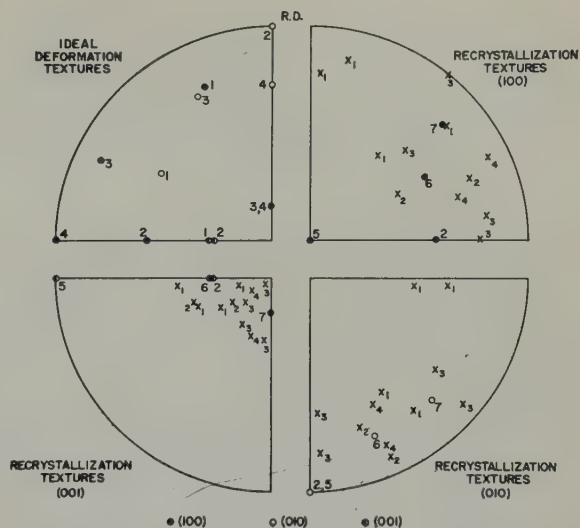


Fig. 6. Ideal deformation and recrystallization texture components of alpha-uranium sheet¹⁴). Circular points represent ideal components, and \times 's represent recrystallization components constructed from ideal deformation components and recrystallization orientation relationship.

locations of recrystallization components constructed from the deformation components and the recrystallization orientation relationship are plotted as "X"; the numbers refer to the ideal deformation textures from which they originated.

The agreement between observed and constructed components was reasonably good with the exception of number 5. None of the constructed (100) and (001) positions lie close to their respective poles; although, the (010) pole was in an area of agreement. This component was reported as the least important. The best agreement occurs for number 6 recrystallization component and the positions constructed from number 2 deformation component. All three of the reported poles were centrally located with respect to the constructed poles. Number 2 deformation and number 6 recrystallization components were reported as most important.

The magnitude of rotation about the axis common to the deformed and recrystallized orientations for orthorhombic alpha-uranium agrees reasonably well with that reported for

cubic and hexagonal metals, namely 20° to 40° . The recrystallization relationship, however, differs from that for the higher symmetry metals because rotation is not about an axis normal to the most densely populated (and slip) planes.

5. Conclusions

The orientation relationship between recrystallized grains obtained upon annealing single crystals of alpha-uranium after compression at room temperature and the deformed orientations present in the crystals can be expressed as 27.5° rotations about axes located 70.0° from the [100], 63.5° from the [010] and 34.0° from the [001]. Rotations for the axes in the first and third quadrants of a (001) standard projection were in a clockwise direction and counter-clockwise for axes in the second and fourth quadrants. In arriving at this relationship, the grains were considered to originate from twin orientations as well as from the parent crystal. The twins necessary to explain the recrystallized grains corresponded exactly with the operative twins.

The same type of relationship was obtained from orientation data reported by Calais, Lacombe and Simenel for recrystallized grains grown by annealing single crystals deformed in tension at room temperature. Comparison of recrystallization textures for polycrystalline alpha-uranium rods and sheets with ones constructed from the deformation textures and the orientation relationship showed good agreement.

Acknowledgements

This work was performed under the direction of Dr. F. G. Foote. The author is indebted to

Dr. H. H. Chiswick who reviewed the paper and made several helpful suggestions. The metallographic preparations and much of the X-ray work were done by Mr. M. D. Odie. This work was performed under the auspices of the Atomic Energy Commission of the United States of America.

References

- 1) J. J. Becker and J. N. Hobstetter, *Trans. AIME* **197** (1953) 1235
- 2) S. Kohara, M. N. Parthasarathi and P. A. Beck, *Trans. AIME* **212** (1958) 875
- 3) H. Yoshida, B. Liebmman and K. Lücke, *Acta Met.* **7** (1959) 51
- 4) C. G. Dunn and P. K. Koh, *Trans. AIME* **206** (1956) 1017
- 5) C. G. Dunn and P. K. Koh, *Trans. AIME* **209** (1957) 81
- 6) Y. C. Liu and W. R. Hibbard, Jr., *Trans. AIME* **203** (1955) 381
- 7) G. Wiener and R. Concoran, *Trans. AIME* **206** (1956) 901
- 8) Hsun Hu, *Trans. AIME* **209** (1957) 1164
- 9) W. P. Chernock and P. A. Beck, Argonne National Laboratory (USA) Report ANL 4839 (1951)
- 10) M. H. Mueller, H. W. Knott, W. P. Chernock and P. A. Beck, *Trans. AIME* **212** (1958) 793
- 11) M. H. Mueller and H. W. Knott, Argonne National Laboratory (USA) Report ANL 5329 (1957)
- 12) M. H. Mueller and H. W. Knott, Argonne National Laboratory (USA) Report ANL 5887 (1958)
- 13) L. K. Jetter and C. J. McHargue, *Trans. AIME* **209** (1957) 291
- 14) M. H. Mueller, H. W. Knott and P. A. Beck, *Trans. AIME* **203** (1955) 1214
- 15) C. M. Mitchell and J. F. Rowland, *Acta Met.* **2** (1954) 559
- 16) E. S. Fisher, *Trans. AIME* **209** (1957) 882.
- 17) L. T. Lloyd and H. H. Chiswick, *Trans. AIME* **203** (1955) 1206.
- 18) D. Calais, P. Lacombe and Mme. N. Simenel, *J. Nucl. Mat.* **1** (1959) 325

ON THE PRODUCTION OF DISPLACED ATOMS BY THERMAL NEUTRONS

R. M. WALKER

General Electric Research Laboratory, Schenectady, N.Y., USA

Received 28 January 1960

The production of displaced atoms by processes resulting from thermal neutron capture are discussed. The results of an approximate calculation are presented which indicate that, in a number of elements, the number of displaced atoms produced by the recoil following capture γ -ray emission may form an appreciable fraction of the total number of displaced atoms produced in a reactor experiment. The unique features of the radiation damage produced by thermal neutrons are noted, and some considerations attendant upon isolating and using such reactions in damage experiments are discussed.

L'auteur discute le déplacement d'atomes dû aux processus résultant de la capture de neutrons thermiques. Il présente les résultats d'un calcul approché qui indiquent que, pour certains des éléments, le nombre des atomes déplacés produits par le recul qui suit une émission gamma de capture peut former une partie appréciable du nombre total des atomes déplacés produits dans une expérience en cours dans le réacteur.

1. Introduction

When materials are irradiated in a reactor it is generally assumed that fast neutrons are primarily responsible for the displacement of atoms leading to observable radiation effects. In certain cases, however, the thermal neutron flux may be responsible for a major portion of the damage. This paper considers such thermal neutron effects in various elements. The major thermal neutron damage process is the production of displaced atoms by atom recoils following emission of prompt capture γ -rays. In general, one can neglect the damage production due to recoils following decay β -rays and γ -rays, since the recoil energies produced this way are much lower than those resulting from prompt γ -ray emission. The production of

Les caractères uniques des effets des irradiations par neutrons thermiques sont notés et quelques considérations sur la possibilité d'isoler et d'utiliser de telles réactions dans les expériences de dommage par irradiation sont discutées.

Die Entstehung atomarer Fehlstellen als Folge von Prozessen, die vom Einfang thermischer Neutronen herrühren, wird besprochen. Hierzu werden die Ergebnisse einer näherungsweisen Berechnung angeführt. Daraus geht hervor, dass bei einer Reihe von Elementen die Zahl der atomaren Fehlstellen, die durch die Rückstöße bei γ -Emission infolge von Einfangprozessen erzeugt werden, einen merklichen Teil der Gesamtzahl atomarer Fehlstellen ausmacht, welche beim Reaktorexperiment entstehen. Die ausserordentlichen Merkmale der Strahlenschädigung infolge von thermischen Neutronen werden herausgestellt. Ferner werden Überlegungen angestellt, welche sich aus der Trennung und Anwendung solcher Reaktionen bei Bestrahlungsexperimenten ergeben.

damage by the subsequent interaction of emitted radiations with nuclei other than the parent nucleus can also be neglected as this is a second order effect. In certain special cases, de-excitation of a nucleus following thermal capture involves the emission of a fast heavy particle. These reactions have long been recognized and studied and will not be considered further here. In what follows, therefore, we will consider only the production of defects arising from (n, γ) reactions.

Schweiner¹⁾ recently called attention to this process in Si and Ge. We discuss here the results for a number of elements obtained on the basis of an approximate calculation. It is shown, for an assumed "typical" reactor irradiation, that the thermal neutron induced

displacement damage may be a significant fraction of the total displacement damage in about 30 elements. The unique character of the damage produced by thermal neutrons is noted, and some considerations involved in using this as a tool for radiation damage research are discussed.

2. Calculation of Displaced Atom Concentrations

We discuss first the calculation of damage production by slow neutron (n, γ) reactions. Following this, the damage production by fast neutrons is calculated and compared with the slow neutron rates.

In order to calculate the damage produced by recoiling atoms, it is necessary to know their energies. If all the excitation energy of a captured neutron is released as a single γ -ray of energy E (in MeV), then the recoil atom has a unique energy T (in MeV) given from momentum conservation as

$$T = \frac{537 E^2}{A} \times 10^{-6} \quad (1)$$

where A is the atomic weight. E is generally ≈ 6 MeV, and, therefore, T may be several hundred electron volts. Since the threshold energy for the production of radiation damage is only about 25 eV, such energetic recoils can produce extensive damage.

If we let φ_t be the flux of thermal neutrons and σ_t the capture cross section, then the fraction of atoms in a thin specimen which capture neutrons and hence recoil is given by $\varphi_t \sigma_t$. If each of these recoils forms an average total number of displaced atoms equal to $\bar{\nu}_t$, then the total fraction, F_t , of displaced atoms produced in the target is given by

$$F_t = \varphi_t \sigma_t \bar{\nu}_t. \quad (2)$$

For moderately heavy elements, Dienes and Vineyard²⁾ give

$$\bar{\nu} \approx \bar{T}/2T_d, \quad (\bar{T} \gg T_d) \quad (3)$$

where T_d is the threshold energy for damage

production. Combining these expressions we obtain

$$F_t = \frac{269 E^2 \varphi_t \sigma_t}{AT_d} \times 10^{-6}. \quad (4)$$

Unfortunately, the excitation energy is not usually released in a single γ -ray. Generally, many γ -rays are emitted in cascade. If their emission time is short compared to the recoil atom collision time, the final relevant recoil energy is determined by both the magnitude and angular correlation of the various γ -rays. If the emission times are longer than the collision times, then the individual γ -rays in the cascade can be treated separately. The emission time depends strongly on the nature of the transition involved and for energetic electric dipole transitions can be much shorter than the recoil collision times. Since the necessary angular correlation data and detailed level schemes necessary to properly treat the problem are not known, we have adopted the following crude model to evaluate the recoil energies following γ -emission. In a cascade process, if the initial γ -ray has an energy between E_{\max} and $\frac{1}{2} E_{\max}$, then it must be followed by lower energy γ -rays. Neglecting angular correlation, these secondary γ -rays serve only to broaden the nuclear recoil energy characteristic of the initial high energy γ -ray. As a simplification in calculating the damage, we arbitrarily count only those captures in which such a high energy γ -ray is present. All captures which do not yield a γ -ray between $\frac{1}{2} E_{\max}$ and E_{\max} are neglected. Specifically, we assume that the concentration of defects due to the capture process is given by

$$F_t \approx (2.7 \times 10^{-4}) \frac{\varphi_t \sigma_t}{AT_d} \int_{\frac{1}{2} E_{\max}}^{E_{\max}} E^2 N(E) dE \quad (5)$$

where $N(E)dE$ represents the number of γ -rays having energies between E and $E+dE$ per neutron capture.

We wish now to calculate the damage produced by fast neutrons. In this case the elastic scattering of the incident neutrons

produces recoil atoms with large kinetic energies. In analogy to eq. (2), the fraction, F_f , of displaced atoms in a thin target is given by

$$F_f = \varphi_f \sigma_f \bar{v}_f \quad (6)$$

where σ_f is the fast neutron scattering cross section. If the energy of the bombarding neutrons is W (in MeV), then the average energy of the recoil atoms is given approximately by ²⁾

$$\bar{T} = 1.3 \frac{AW}{[1+A]^2} \approx \frac{1.3W}{A}. \quad (7)$$

Using eq. (3) this gives

$$F_f = \frac{0.65 W \varphi_f \sigma_f}{AT_d}. \quad (8)$$

In a reactor there is a wide spectrum of fast neutron energies, and the calculation of the concentration of displaced atoms becomes quite difficult. A conventional approximation (see, for example, ref.²⁾) is to use eq. (8) which is appropriate for a unique neutron energy and treat the parameters therein as appropriate average values. For example, W is typically taken as 1 MeV, and φ_f is then defined as the equivalent flux of such energy neutrons.

We consider now the relative importance of slow and fast neutron damage production in a reactor. If we define R as the ratio of defects produced by thermal neutrons to those produced by fast neutrons the foregoing discussion gives

$$R \approx \frac{(4 \times 10^{-4})}{W} \left(\frac{\varphi_t}{\varphi_f} \right) \left(\frac{\sigma_t}{\sigma_f} \right) \int_{\frac{1}{2}E_{\max}}^{E_{\max}} E^2 N(E) dE. \quad (9)$$

Both (σ_t/σ_f) and the capture γ -ray spectra vary widely, and it is necessary to consider these quantities for each element in order to decide whether thermal neutron effects are important. In table 1 we have listed rough numerical values of R . Only those elements with $R \geq 0.1$ are included. In preparing this table we took $\varphi_t/\varphi_f = 10$ and $W = 1$ MeV as "typical" reactor values. The thermal neutron cross sections were taken from the compilation by Stehn and

TABLE 1

Elements in which the amount of damage produced by the absorption of thermal neutrons is a significant fraction of the total damage in a "typical" in-pile experiment. We have assumed a value of 10 for the ratio of thermal to fast fluxes and an average energy of 1 MeV for the fast neutrons

Element	Ratio of thermal to fast cross sections σ_t/σ_f	R	P
Ag	9	0.5	0
Au	19	0.6	0
Cd	500	20	7×10^3
Ci	15	2.4*	220
Co	12	1.2	330
Cs†	5	0.2	0
Dy†	160	4.8	0
Er†	24	0.7	0
Eu†	61	1.8	5.9
Gd	5400	81	3.5×10^4
Hf	15	0.6	18
Hg	70	2.1	6
Ho†	9	0.3	0
In	30	1.0	0
Ir†	66	1.9	0
Lu†	15	0.5	0
Mn	5	0.5	0
Nd†	7	0.2	21
Os†	2	0.1	4.5
Pr	2	0.1	0
Re†	12	0.4	0
Rh	22	1.1	0
Sc	10	0.7	0
Se	2	0.2	15
Sm	1400	26	170
Ta	3	0.1	0
Tb†	6	0.2	0
Ti	2	0.3	850
Tm†	18	0.6	0
V	2	0.3	< 0.1
W	3	0.1	0.6
Yb†	5	0.2	0

R is the ratio of capture recoil displacements to those produced by fast neutrons calculated from eq. (9) of text. P is the number of captures leading to stable isotopes relative to those which lead to unstable isotopes.

* Includes 20 % contribution from the process $\text{Cl}^{35}(\text{n}, \text{p})\text{S}^{35}$.

† Detailed γ -ray data were lacking, and it was assumed arbitrarily that the spectrum was identical to Sm. This probably predicts low values of R since Sm has the lowest fraction of high energy γ -rays of any of the elements included.

Clancy³). Fast neutron data were obtained from the papers by Miller *et al.*⁴), Walt *et al.*⁵), and Okazaki *et al.*⁶). Data on the capture γ -ray spectra were taken from the compilation by Bartholomew and Higgs⁷). Values for the noble gases are not included in table 1.

We wish to emphasize the approximate nature of these calculations. Both the basic radiation damage theory and the treatment of the γ -ray recoils are of uncertain validity. The values in table 1 should therefore be regarded as rough estimates. It is well known that the theory outlined above overestimates fast neutron damage. However, in the case of electron bombardment—where small recoil energies are involved—the overestimation is not nearly so much. Since the recoil energies for the (n, γ) events are small compared to those produced by fast neutrons, the above calculation probably overestimates the fast neutron damage relative to the slow neutron damage.

3. Discussion

The results listed in table 1 indicate that there are some thirty elements in which, in either their pure states or in chemical compounds, displacement effects produced by thermal neutrons might form an important part of the damage. Whether or not they will do so in a particular experiment depends on a number of factors, such as the nature of the compound used, the actual ratio of thermal and fast fluxes, shielding, etc. Although it is not expected that these considerations will affect any of the qualitative conclusions of prior work, it seems possible that thermal neutron displacements have played a role in certain experiments. Experiments with and without a Cd shield obviously can be used to single out such thermal neutron effects.

It should be noted that the derivation of R is based on the assumption that the attenuation of the neutron fluxes is negligible throughout the sample being considered. However, many of the elements in table 1 have very high thermal cross sections. In this case the thermal neutron effects will be produced only in a shallow layer.

Therefore, the effects treated here may be important only for thin samples or for surface phenomena.

So far we have discussed the displacement of atoms by thermal neutrons in the presence of a large flux of fast neutrons. If the samples are removed to a position where the fast flux is negligible, it should be possible to isolate the thermal neutron effects and use them as a tool for radiation damage research. Such an experiment has been performed by Cleland⁸). The thermal neutron reactions have the unique advantage that they tend to produce small clusters of defects starting with a recoil nucleus of a more or less well defined energy. As such they would complement conventional methods of producing radiation damage which produce quite different defect distributions.

An important factor in considering the use of (n, γ) reactions to produce damage is the absolute magnitude of the absorption cross section. This determines whether observable effects can be achieved in reasonable irradiation times. It is particularly important if it is necessary to move samples to positions where $\varphi_t/\varphi_f \gg 10$, as this may entail a loss of absolute intensity. In general, the elements listed in table 1 are those with the highest thermal cross sections, and hence are the most suitable in which to obtain observable effects. Note, however, that Ge, in which Cleland did observe such effects, does not appear in table 1. This illustrates that presently available thermal neutron fluxes are sufficient to cause measurable damage.

Quite apart from the absolute cross sections, the utility of such experiments depend to a large extent on how well the average recoil energy can be defined. This, in turn, depends on the spectrum of the capture γ -rays. Mittleman⁹) has grouped γ -ray spectra into two major classes. In the first class the ground state transition is dominant, and one high energy γ -ray dominates. Examples given by Mittleman of such elements are Al, Be, Bi, C, Cr, Cu, F, H, Fe, Pb and Ni. In the second class many γ -rays are present. It is further

useful to divide this second class into a group (2a) in which the spectrum consists of a number of well resolved lines and a group (2b) in which the spectrum is for the most part unresolved. Group 2a may be useful if only several lines dominate the spectrum. Ti is an example in this last group where two closely spaced lines at 6.8 and 6.4 MeV have a total intensity ≈ 70 per hundred captures.

An interesting complication arises in connection with the use of thermal neutrons to study displacement damage. If the resulting nucleus decays to a new atomic number, then every absorption results in a chemical impurity. Such impurities can affect the study of radiation damage in several ways. In the first place, they contribute a constant change which does not recover upon annealing. Secondly, as shown by Blewitt *et al.*¹⁰) and Walker and Corbett¹¹), they can interact with the displaced atoms and modify both the production and recovery of the damage. It is therefore important to consider how many chemical impurities are introduced by transmutations. In table 1 we have included a parameter P which is defined as the number of captures which lead to stable isotopes (defined arbitrarily by the condition $t_{1/2} \geq 1$ year) divided by the number of captures which lead to different atomic numbers. The data were taken from the compilation by Strominger *et al.*¹²). In certain cases, as for example in Au, the decay time is such that it should be possible to study the recovery of the radiation damage under the two conditions: (a) where not many atoms have decayed and (b) where essentially all the atoms have decayed. Thus it would be possible to study the effects of a specific impurity in close proximity to a cluster of displaced atoms.

4. Conclusions

We have considered the production of displaced atoms by nuclear recoils resulting from

the emission of capture γ -rays following thermal neutron absorption. We have concluded that for a number of elements such recoils may produce a significant fraction of the total radiation damage measured in a "typical" in-pile experiment, where both fast and slow neutrons are present. The unique character of the radiation damage produced by capture γ -ray recoils has been noted, and we have briefly discussed some of the considerations attendant upon using these thermal neutron displacement effects as a tool for radiation damage research.

Acknowledgements

The author would like to acknowledge the generous assistance of J. R. Stehn in helping to locate the necessary tabulations of nuclear data. Thanks are also due J. W. Corbett and C. W. Tucker for a review of the manuscript.

References

- 1) H. C. Schweinler, J. Appl. Phys. **30** (1959) 1125
- 2) G. J. Dienes and G. H. Vineyard, Radiation Effects in Solids (Interscience Publishers, Inc., New York, 1957)
- 3) J. R. Stehn and E. F. Clancy, Chart of the Nuclides (April, 1956 edition)
- 4) D. W. Miller, R. K. Adair, C. K. Bockelman and S. E. Darden, Phys. Rev. **88** (1952) 83
- 5) M. Walt, R. L. Becker, A. Okazaki and R. E. Fields, Phys. Rev. **89** (1953) 1271
- 6) A. Okazaki, S. E. Darden and R. B. Walton, Phys. Rev. **93** (1954) 461
- 7) G. A. Bartholomew and L. A. Higgs, Compilation of Thermal Neutron Capture Gamma Rays, Atomic Energy of Canada Limited, Rept. AECL No. 669
- 8) See ref. 1)
- 9) P. Mittleman, Nuclear Development Associates, Inc., USA, Report No. NDA10-99 (1953)
- 10) T. H. Blewitt, R. R. Coltman, E. E. Klabunde and T. S. Noggle, J. Appl. Phys. **28** (1957) 639
- 11) R. M. Walker and J. W. Corbett, Bull. Am. Phys. Soc. **5** (1960) 25
- 12) D. Strominger, J. M. Hollender and G. T. Seaborg, Revs. Mod. Phys. **30** (1958) 585

PROCESSUS DES TRANSFORMATIONS DANS LES ALLIAGES URANIUM-MOLYBDENE DE FAIBLES TENEURS EN MOLYBDENE

Mme J. LEHMANN

Département de Métallurgie Service de Technologie, Centre d'Etudes Nucléaires de Saclay, Gif-sur-Yvette, (S. & O.), France

Reçu 5 décembre 1959

Dans les alliages uranium-molybdène de teneur 0,5 à 4 % en poids de Mo, deux processus de formation de la phase α ont été mis en évidence. Pour les alliages de teneurs inférieures à 0,9 %, la transformation se fait à partir de la phase β avec une très importante hystérésis. Pour les alliages de teneurs supérieures à 0,9 %, il y a précipitation lamellaire de phase α dans la matrice γ , la microstructure présente alors un grain fin.

Une corrélation a été établie avec le diagramme d'équilibre, les limites des domaines de stabilité des zones β et $(\beta + \gamma)$ du diagramme U-Mo ont été déterminées: le maximum de solubilité solide en phase β se trouve à 0,9 %.

Two mechanisms of α -phase transformation have been revealed in uranium-molybdenum alloys with a 0.5 to 4 % Mo weight content. In alloys with contents up to 0.9 %, the transformation occurs from the α phase with a very important hysteresis. In alloys

with contents higher than 0.9 %, a lamellar precipitation of the α phase occurs in the γ matrix. The microstructure shows then a small grain.

A correlation has been established with the equilibrium diagram. The limits of the areas of stability of β and $(\beta + \gamma)$ of the U-Mo diagrams were determined: the maximum of solid solubility in the β phase occurs at 0.9 %.

Bei Uran-Molybdän-Legierungen mit 0,5 bis 4 Gew. % Mo wurden zwei Arten der Umwandlung in die α -Phase aufgedeckt. Bei Legierungen mit Gehalten unter 0,9 % läuft die Umwandlung mit beträchtlicher Hysterese ab. Bei Legierungen mit mehr als 0,9 % Mo findet eine Ausscheidung von lamellaren α -Kristallen in der γ -Matrix statt. Dabei zeigt sich ein feinkörniges Gefüge.

Eine Beziehung zum Zustandsdiagramm wurde festgestellt. Die Grenzen des β -Bereichs und des $(\beta + \gamma)$ -Bereichs wurden ermittelt: die maximale Löslichkeit in der β -Phase liegt bei 0,9 %.

1. Introduction

Les alliages uranium-molybdène de faibles teneurs ont été l'objet d'une précédente étude dans laquelle nous avons déterminé les propriétés technologiques de ces alliages ainsi que les cinétiques des transformations au cours de refroidissements continus à différentes vitesses¹).

Cette étude a pour but d'établir les cinétiques des transformations isothermes (diagrammes T.T.T.) des alliages dont la teneur est voisine de 2-3-4 % en poids de Mo. Nous décrirons les différentes transformations s'effectuant par des mécanismes de germination et croissance. Un article ultérieur donnera la description des phases formées par un mécanisme de cisaillement.

Certaines limites du diagramme d'équilibre, dans la région des faibles teneurs en molybdène, ont été précisées, en particulier les limites séparant les domaines

$$\beta/\beta + \gamma, \beta + \gamma/\gamma \text{ et } \beta + \gamma/\alpha + \gamma.$$

Ceci nous a conduit à établir une corrélation entre la taille du grain des alliages bruts de coulée et le diagramme d'équilibre.

2. Matériaux utilisés

Les alliages ont été préparés, soit par fusion et coulée sous vide (chauffage en haute fréquence), soit par fusion au four à arc.

L'uranium utilisé est l'uranium ordinaire CEA contenant entre 80 et 200 ppm de Al, Fe, Ni,

Cr, Mn, environ 100 ppm de carbone et 100 ppm de silicium.

Le molybdène employé est sous forme de pastilles frittées contenant environ 150 ppm d'impuretés métalliques et 100 ppm de carbone.

Les alliages de teneur en molybdène allant jusqu'à 3 % en poids ont été préparés par fusion en haute fréquence dans un creuset de graphite brasqué avec de la thorine. La coulée en chute permet l'obtention de barreaux de diamètre: 16 ou 26 mm et de longueur: 200 mm.

L'alliage de teneur en molybdène 4 % en poids a été préparé par fusion au four à arc, avec électrode de tungstène, l'alliage est obtenu après 3 fusions, sous forme de lingotins plats d'environ 150 g. Les résultats des dosages de molybdène sont donnés au tableau 1.

TABLEAU 1
Teneur en molybdène des alliages

Désignation de l'alliage	Molybdène (poids pour cent)
U-Mo 0,5	0,54 à 0,57
0,8	0,73 à 0,81
0,9	0,9 à 0,95
1	1 à 1,15
1,7	1,7 à 1,76
2	2,02 à 2,05
3	3,04 à 3,1
4	4,2 à 4,4

La teneur en carbone varie de 110 à 650 ppm pour les alliages 0,5 à 3. Elle est d'autant plus grande que la concentration en molybdène est plus élevée. Ceci est dû au mode de fabrication des alliages. La fusion étant effectuée dans des creusets de graphite, la mise en solution du molybdène nécessite des maintiens au-dessus du point de fusion d'autant plus longs que l'alliage est plus chargé en molybdène.

Nous avons examiné quel était l'effet de cette teneur en carbone, d'une part sur de l'uranium auquel étaient ajoutés 500 ppm de carbone sous forme de monocarbure (UC), d'autre part sur les alliages uranium-molybdène.

Dans les deux cas, l'aspect micrographique montre la dispersion du monocarbure sous forme d'inclusions cubiques, et les diagrammes de

rayons X montrent deux raies caractéristiques de UC très fines et d'intensité moyenne.

Des traitements de 200 h à 950° C n'apportent aucune modification, ni dans l'aspect micrographique, ni dans les diagrammes de rayons X. Ceci s'explique par la très faible solubilité solide du carbone dans chacune des phases allotropiques α , β , γ de l'uranium.

3. Méthodes et appareillage

3.1. DIAGRAMMES T.T.T.

Nous avons établi les tracés des courbes T.T.T. en effectuant des traitements thermiques de trempes étagées.

Des échantillons de 80 g environ ont subi un traitement d'homogénéisation sous vide de 10^{-5} mm Hg, à 900 ou 950° C pendant des durées variant de 24 à 250 h, suivant la concentration en molybdène et le mode de fabrication, ils ont ensuite été trempés en bain d'huile. Le four est montré figure 1. Ce traitement d'homogénéisation a eu pour but de limiter le traitement ultérieur en phase γ à quelques minutes.

Les trempes étagées comportaient:

le traitement en phase γ de 3 à 5 min à 950° C, la trempe isotherme à chacune des températures choisies au-dessous de la température de transformation, pendant des durées échelonnées de 10 secondes à une centaine d'heures, la trempe finale en bain d'huile ou à l'eau salée glacée.

Ces trempes étagées sont effectuées sur des échantillons de 20 g environ, par passage dans des bains de sels ou d'alliages présentant un point eutectique à bas point de fusion. Ce mode opératoire est utilisé pour les alliages dont la période d'incubation est courte (quelques secondes) et pour lesquels la durée de traitement isotherme ne dépasse pas quelques heures.

Lorsque la période d'incubation est longue, nous avons utilisé un appareillage constitué par deux fours Chevenard verticaux de 2 kW, superposés (fig. 2). L'enceinte est maintenue sous un vide de 10^{-5} mm Hg, le four supérieur est à 950° C et le four inférieur à la température isotherme choisie. Le passage d'une température

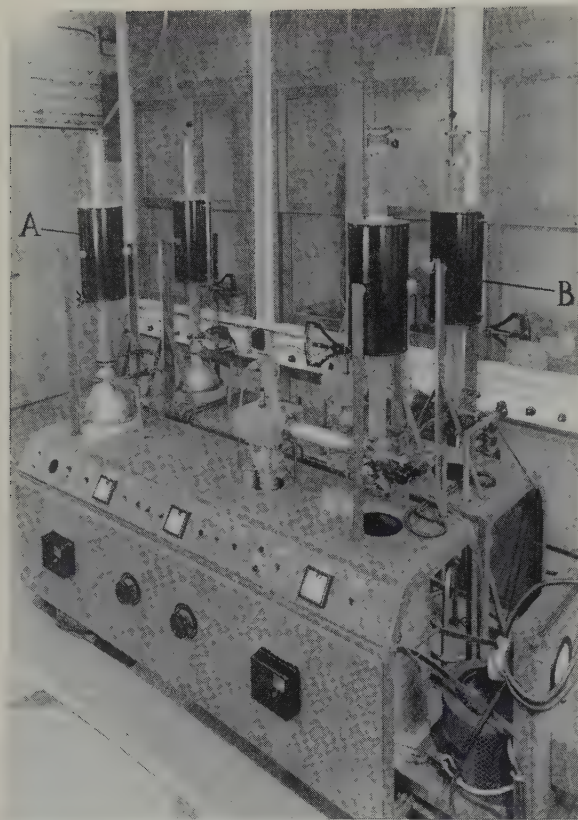


Fig. 1. A, Fours pour traitements d'homogénéisation et trempe en bain d'huile (sous vide primaire). B, Fours pour traitements d'homogénéisation et trempe eau, huile ou bain métallique (sous vide secondaire).

à l'autre se fait en une durée variant de 3 à 6 minutes, et la trempe finale se fait par ouverture d'une porte inférieure et descente du porte échantillon dans un bain d'eau ou d'huile. Cet appareil n'est utilisable que pour les alliages présentant des cinétiques lentes : cas de l'alliage 4.

3.2. DIAGRAMME D'ÉQUILIBRE

La méthode utilisée comporte des traitements thermiques en bains de sels à différentes températures, suivis de trempes en bain d'huile.

Les traitements ont été effectués soit en portant directement les échantillons de la température ambiante aux différentes températures pendant des durées de 20 h, soit par traitements de 30 min à 950° C suivis de trempe isotherme de durée 20 h.

Les deux catégories de traitements énoncées ci-dessus ont donné, dans la plupart des cas, des résultats identiques quant à la nature des phases observées sauf pour l'alliage 0,5 pour lequel une durée de 20 h n'est pas toujours suffisante pour la transformation.

Dans les deux cas les résultats des transformations ont été observés par examens micrographiques, par rayons X et par mesures de dureté.

Les méthodes d'examens micrographiques ont été préalablement décrites¹⁾.

La diffraction des rayons X a été faite au diffractomètre à compteur, avec le rayonnement polychromatique du cuivre et les examens sont effectués sur des échantillons massifs polis électrolytiquement.

Les mesures de dureté sont effectuées à la température ambiante sous charge de 40 kg (duromètre Vickers).

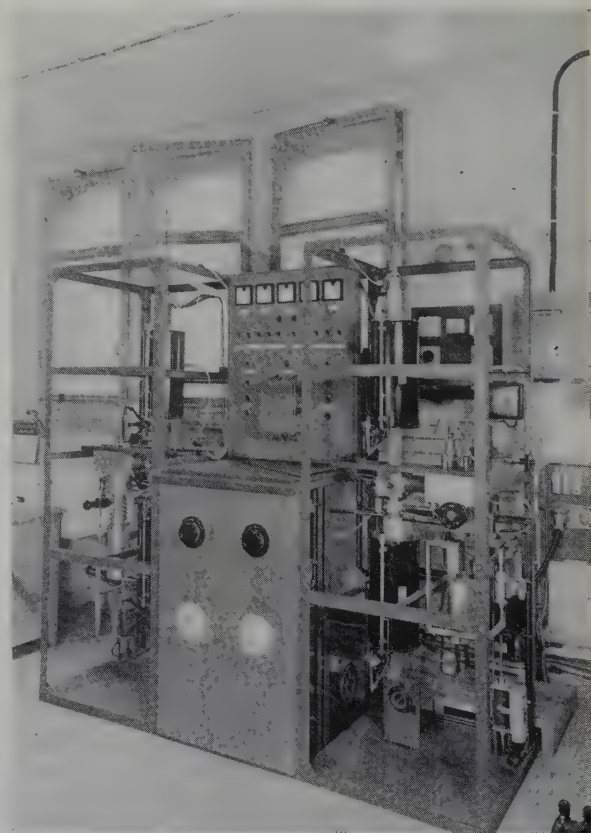


Fig. 2. Fours pour traitements isothermes de longues durées.

4. Diagramme d'équilibre

4.1. DESCRIPTION DES DIAGRAMMES D'ÉQUILIBRE PUBLIÉS

Le diagramme d'équilibre uranium-molybdène (fig. 3) a été établi par Saller, Rough et Vaughan²⁾ et Saller, Rough et Bennett³⁾.

Les solubilités solides du molybdène dans chacune des 3 phases allotropiques de l'uranium γ , β , α , ont donné lieu à beaucoup de controverses.

a. Solutions solides γ

La solubilité solide du molybdène dans la phase γ de l'uranium est très importante. Elle atteint 22,6 % en poids au point péritectique (1285° C).

A 575° C et 11,3 % de Mo se trouve un point eutectoïde correspondant à la transformation de γ en $(\alpha + \gamma')$. La phase γ' s'étend de 16 à 17 % en poids de Mo, ce qui correspond approxi-

mativement à la composition U_2Mo ; γ' est quadratique⁴⁾ et est considéré comme une phase ordonnée de γ .

D'après Konobevsky⁵⁾ le point eutectoïde se trouve à 9,8 % en poids au lieu de 11,3 % en poids et 560° C au lieu de 575° C.

Dans les teneurs en Mo voisines de la composition eutectoïde, un refroidissement rapide permet la rétention de solutions solides γ , métastables, à la température ambiante.

b. Solutions solides β et α

D'après le diagramme d'équilibre de Saller, Rough et Vaughan²⁾ la zone de stabilité de la phase β est abaissée jusqu'à 685° C pour une teneur de 0,4 % en poids de Mo, correspondant à un point eutectoïde $\beta \rightarrow \alpha + \gamma$, la solubilité solide en phase α est de 0,2 % en poids de Mo à 600° C.

Dans l'intervalle de concentration 0,4 à 2,5 % en poids de Mo et au-dessus de 658° C est située une zone de deux solutions solides ($\beta + \gamma$) et au-delà de 2,5 % il y a passage direct de γ à $(\alpha + \gamma')$.

D'après Konobevsky⁵⁾ le maximum de solubilité solide du molybdène en phase β est beaucoup plus important: 1,2 % en poids de Mo au lieu de 0,4 % en poids à une température eutectoïde de 635° C au lieu de 658° C. La solubilité en phase α est fixée à environ 0,98 % en poids de Mo.

Dwight⁶⁾ a présenté un autre tracé du diagramme d'équilibre sur lequel la limite, entre les domaines $(\alpha + \gamma)$ et $(\beta + \gamma)$ est située à $637 \pm 3^\circ$ C et le domaine $(\beta + \gamma)$ étendu jusqu'à une concentration de 4 % en poids de Mo. La solubilité solide maximum en phase β est de 0,5 % en poids et la solubilité solide maximum en phase α reste à 0,2 % en poids.

Ces résultats montrent des différences importantes et il était ainsi nécessaire pour étudier les processus des transformations et, en particulier, pour établir le tracé des courbes T.T.T. au voisinage des températures d'équilibre, de déterminer certaines limites du diagramme avec l'uranium CEA dont nous disposions et avec les alliages utilisés pour notre étude.

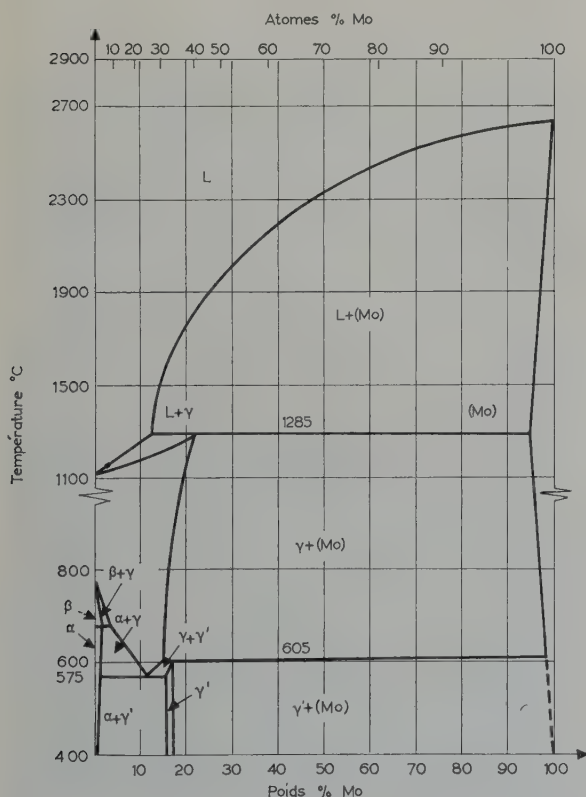


Fig. 3. Diagramme d'équilibre uranium-molybdène (Saller, Rough et Bennett³⁾).

4.2. RÉSULTATS

Les résultats obtenus ont permis d'établir le tracé de la figure 4, la limite entre les domaines $(\alpha + \gamma)$ et $(\beta + \gamma)$ se trouve entre 640 et 650° C soit $645 \pm 5^\circ \text{C}$.

La solubilité solide maximum en phase β est située à 0,9 % en poids de molybdène pour la température de $645 \pm 5^\circ \text{C}$, tandis que la limite de solubilité solide en phase α , que nous n'avons pas précisée, est considérée très inférieure à 0,5 % en poids à la même température.

La limite entre les domaines $(\beta + \gamma)$ et γ s'étend de 772° C pour l'uranium pur à 645° C pour la teneur 3,5 % en poids de Mo environ.

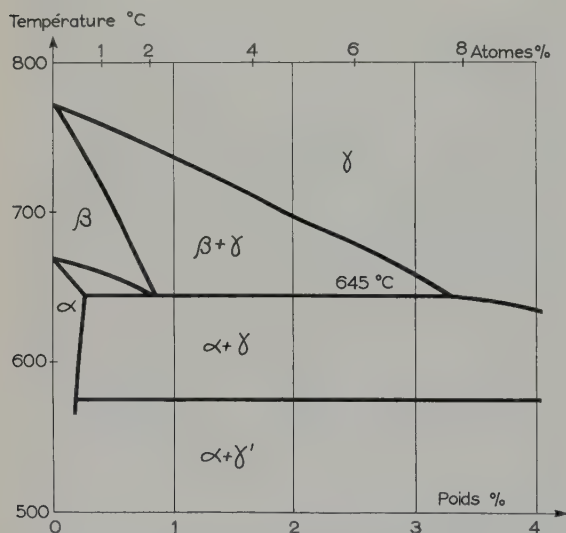


Fig. 4. Diagramme d'équilibre uranium-molybdène (Lehmann).

4.3. DISCUSSION

Ce tracé présente une certaine similitude avec celui de Dwight, en particulier en ce qui concerne le prolongement du domaine $(\beta + \gamma)$ vers des teneurs supérieures à 2,5 % en poids, cependant le maximum de solubilité solide en phase β est plus important: 0,9 % en poids au lieu de 0,5 % en poids.

La limite entre les domaines $(\alpha + \gamma)$ et $(\beta + \gamma)$ se trouve située, sur notre tracé, à 645° C soit à une valeur intermédiaire entre celle donnée par Saller, Rough et Vaughan (658° C) et celles données par Dwight (637° C) et Konobevsky

(635° C). Les conditions expérimentales des différents auteurs sont très voisines, à l'exception de celles de Konobevsky qui a déterminé la limite de solubilité en phase α par mesures des variations des paramètres cristallins.

5. Diagrammes T.T.T.

Les courbes de transformations isothermes ont été établies pour les alliages 2, 3, 4 et comparées à celles de l'alliage 0,5.

D'après le diagramme d'équilibre, jusqu'à une teneur en Mo de 3,5 % en poids environ, il y a passage de la zone γ à la zone de stabilité $(\beta + \gamma)$, mais nous avons observé que les transformations sont très lentes au voisinage de l'équilibre et les retards aux transformations sont très importants.

Les trempes étagées à partir de la zone γ aux températures comprises entre 645° C et les points M_s , produisent une transformation directe $\gamma \rightarrow \alpha$ sans passage intermédiaire par la phase β .

Les cinétiques des alliages étudiés dans cette zone montrent que les transformations peuvent s'opérer selon deux mécanismes. Dans un domaine situé entre 645° C et le point M_s , les transformations se font par germination et croissance. Nous avons déterminé dans cette zone deux domaines correspondants:

l'un à la transformation $\gamma \rightarrow \alpha + \gamma$ entre 645 et 570° C

l'autre à la transformation $\gamma \rightarrow \alpha + \gamma'$ entre 570° C et le point M_s .

Dans le domaine situé entre le point M_s et la température ambiante, la transformation s'opère par cisaillement, la microstructure martensitique observée est une structure en bandes désignée $\alpha_b' \dagger \ddagger$) nous ne décrirons pas cette structure dans cet article.

5.1. TRANSFORMATION $\gamma \rightarrow \alpha + \gamma$

a. Examens micrographiques

Des trempes étagées de 950° C aux températures 630, 620 et 600° C produisent une précipitation de phase α sous forme de lamelles

$\dagger \alpha_b''$ d'après nouvelle nomenclature.



Fig. 5. U-Mo 3 % en poids, 950° C, 3 min. Trempe à 640° C, 1 h. Trempe à l'huile. $\times 450$.



Fig. 7. U-Mo 3 % en poids, 950° C, 3 min. Trempe à 640° C, 6 h. Trempe à l'huile. $\times 450$.



Fig. 6. U-Mo 3 % en poids, 950° C, 3 min. Trempe à 640° C, 1 h. Trempe à l'huile. $\times 450$.

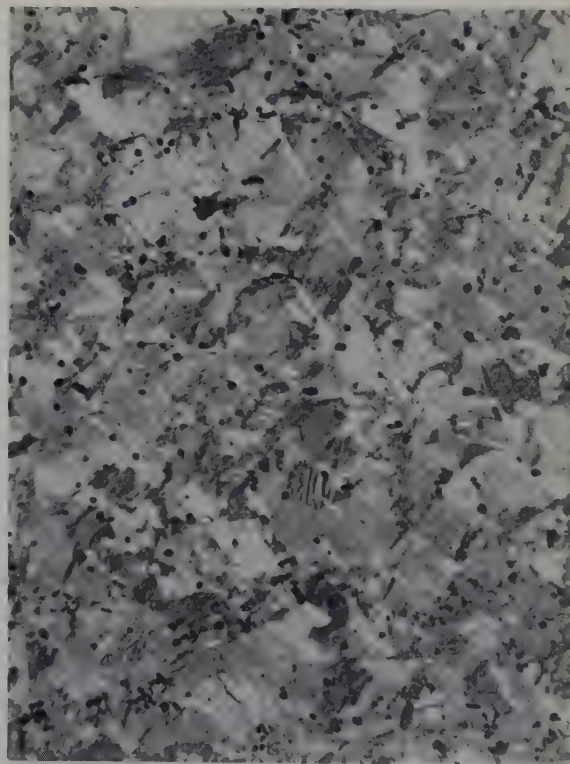


Fig. 8. Mise en évidence des grains aciculaires par examen en lumière polarisée. $\times 150$.

rectilignes orientées suivant plusieurs directions dans la matrice γ formée de gros grains polygonaux.

Des traitements isothermes de durées croissantes ont permis de suivre la progression de la transformation. La figure 5 montre le début de la précipitation des lamelles α perpendiculairement aux joints de grains γ .

Les échantillons examinés à la température ambiante montrent que la matrice s'est transformée au cours de la trempe finale par un mécanisme de cisaillement (fig. 6).

Quelques lamelles isolées sont visibles dans la matrice, elles constituent l'étape initiale de la précipitation. L'étape finale est une décomposition lamellaire constituée par les phases α et γ (fig. 7); ces lamelles parallèles sont groupées par paquets de même orientation, facilement mis en évidence par examen micrographique en lumière polarisée, si bien que l'observation à faible grossissement ($\times 150$) donne l'aspect de grains fins et anguleux de 20 à 50 μ (fig. 8).

b. Mesures de dureté

Les mesures de dureté Vickers ont été effectuées après traitements de durée croissante à 600° C. On observe un maximum de 360 qui correspond à la décomposition lamellaire complète ($\alpha + \gamma$). Lorsque les traitements sont prolongés au-delà de la fin de la transformation, on observe un faible abaissement de la dureté jusqu'à 320 (figs. 9 et 10). Cette valeur est supérieure à celle de la dureté de la solution

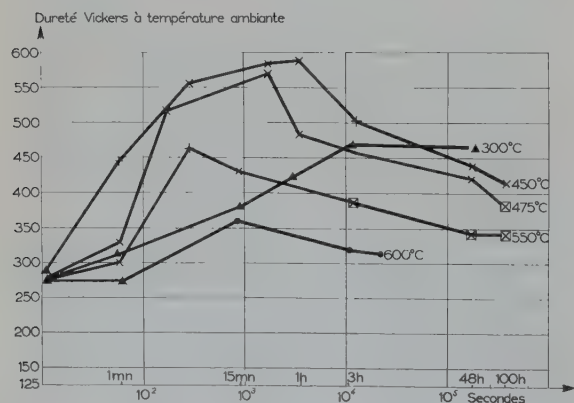


Fig. 9. Alliage U-Mo 3 % en poids. Courbes de duretés.

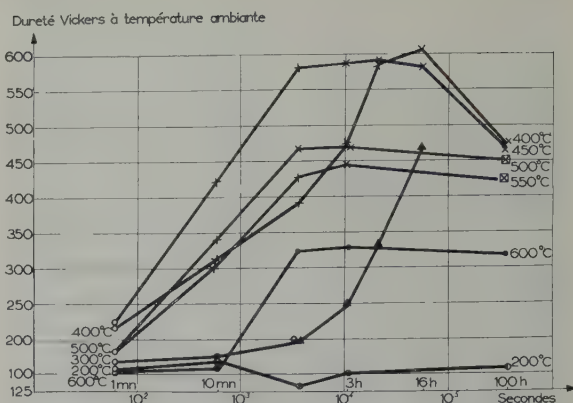


Fig. 10. Alliage U-Mo 4 % en poids. Courbes de duretés.

solide α , à gros grains, de l'alliage 0,5 qui est de 275 seulement; elle est également supérieure à celle des solutions solides γ qui est toujours très faible et ne dépasse pas 180.

c. Diffraction des rayons X

Les diagrammes obtenus avec le rayonnement K_{α} du cuivre montrent la présence de deux phases: α et γ .

5.2. TRANSFORMATION $\gamma \rightarrow \alpha + \gamma'$

a. Examens micrographiques

Dans un domaine de température s'étendant entre 570° C et le point M_s , une transformation d'un type très différent se produit. Nous l'avons étudiée plus particulièrement dans le cas de l'alliage 3 mais elle suit le même processus dans le cas des alliages 2 et 4. La transformation débute par l'apparition de phase α , qui, dans le domaine de température situé entre 560 et 500° C se distingue facilement par examen micrographique en lumière polarisée, et entre 500° C et le point M_s n'est décelée que par la diffraction des rayons X.

A 560° C, la taille moyenne des grains α est de 60 μ , entre 550 et 500° C elle n'est que de 5 μ , enfin à 475° C, on n'observe aucune action sur la lumière polarisée et il n'est pas possible de distinguer la taille des grains par micrographie.

La microscopie électronique n'apporte aucune information supplémentaire, seul, l'examen à l'aide de l'objectif à contraste interférentiel

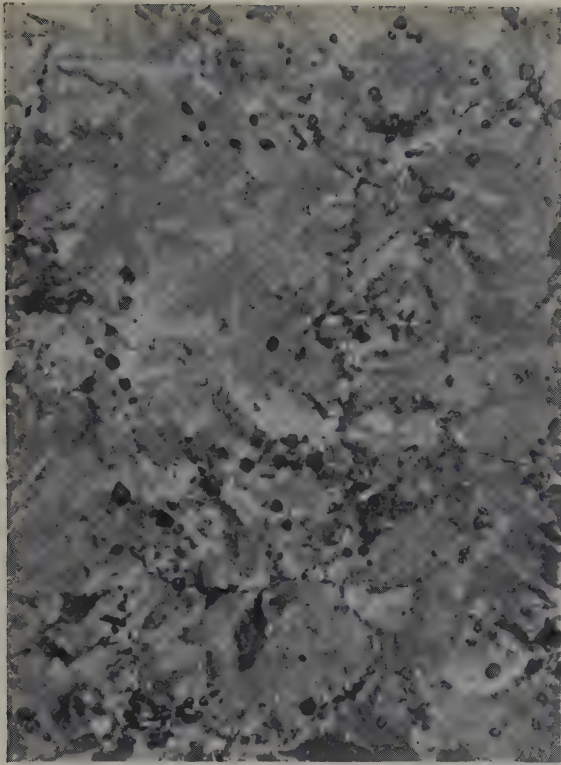


Fig. 11. U-Mo 3 % en poids, 950° C, 5 min. Trempe à 560° C, 5 min. Trempe à l'huile (lumière polarisée). $\times 150$.



Fig. 13. U-Mo 3 % en poids, 950° C, 5 min. Trempe à 475° C, 1 min. Trempe à l'huile (contraste interférentiel). $\times 150$.



Fig. 12. U-Mo 3 % en poids, 950° C, 5 min. Trempe à 550° C, 15 min. Trempe à l'huile (lumière polarisée). $\times 150$.

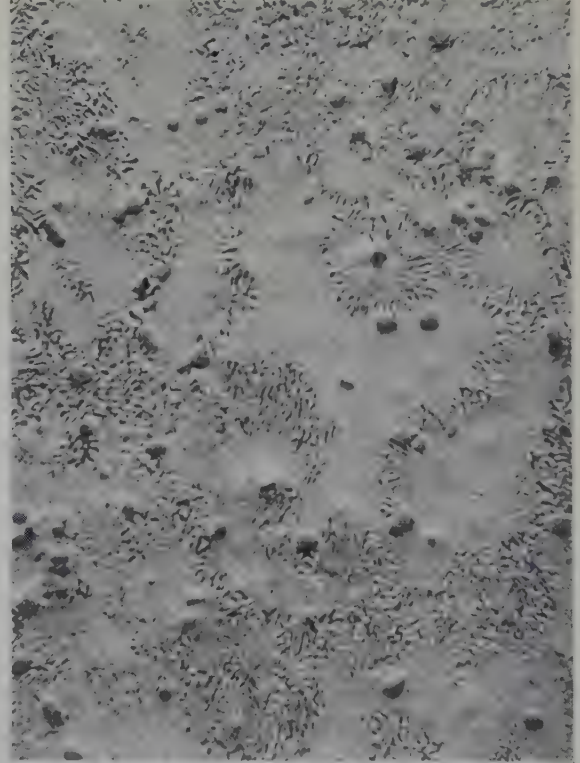


Fig. 14. U-Mo 3 % en poids, 950° C, 5 min. Trempe à 475° C, 3 h $\frac{1}{2}$. Trempe à l'huile (lumière polarisée). $\times 150$.

permet de mettre en évidence un très fin précipité. Les figures 11, 12 et 13 montrent les trois aspects de la phase α décrits ci-dessus.

Les grains polygonaux de la phase mère: γ , ont une taille moyenne de 0,5 à 2 mm et leurs joints sont bordés par une bande étroite présentant un aspect lamellaire.

Dans le domaine de température situé entre 560 et 500° C, lorsque les durées de trempes isothermes sont prolongées, on observe une décomposition en lamelles très fines d'aspect perlitique (fig. 14).

A 475° C, cette même décomposition est beaucoup plus lente à se produire, le pourcentage de phase lamellaire évalué par micrographie est de :

- 20 % après 1 h de traitement,
- 40 % après 3 h $\frac{1}{2}$ de traitement,
- 80 % après 48 h de traitement,
- 90 % après 100 h de traitement.

Dans le cas de l'alliage 4, la transformation n'est que de 20 % après 100 h à 475° C.

La transformation décrite ci-dessus correspond à une décomposition eutectoïde de la phase γ en ($\alpha + \gamma'$); la transformation de γ débute par un rejet de phase α et la décomposition perlitique n'est observable qu'après des traitements isothermes suffisamment longs, surtout aux températures très peu supérieures aux points M_s .

b. Mesures de dureté

Les mesures de dureté Vickers ont été faites après des durées croissantes de traitements isothermes correspondants pour l'alliage 3 aux températures 550, 475 et 450° C et pour l'alliage 4 aux températures 550, 500, 450 et 400° C. Sur les figures 9 et 10 sont portées les courbes de dureté comparées aux courbes obtenues pour ces mêmes alliages dans les zones de décomposition ($\alpha + \gamma$) et dans la zone de transformation martensitique.

Nous avons observé un accroissement considérable de la dureté, celle-ci est d'autant plus élevée que la température de transformation est plus basse dans la zone ($\alpha + \gamma'$); elle est de 570 dans le cas de l'alliage 3 décomposé à 450° C,

et de 610 dans le cas de l'alliage 4 décomposé à 400° C.

La dureté est un peu moins élevée aux températures de 550–500° C, le maximum est 475 pour les deux alliages.

c. Diffraction des rayons X

Nous avons observé l'évolution de la raie de diffraction (110) de la phase γ , ainsi que les positions des raies de diffraction (110), (021), (002) et (111) de la phase α . Les diagrammes ont été effectués sur des échantillons d'alliage 3 ayant subi des trempes isothermes de 950° C à 475° C pendant: 1 min, 20 min, 1 h, 3 h 30 min, 48 h et 100 h.

TABLEAU 2

Diffraction rayons X — Transformations $\gamma \rightarrow \alpha + \gamma'$

Nature de la trempé isotherme après traitement à 950° C 5 min	Raies α Cu K $_{\alpha}$		Raies γ ou γ' Cu K $_{\alpha}$	
	<i>d</i>	<i>hkl</i>	<i>d</i>	<i>hkl</i>
475° C — 1 min	2,562	(110)		
	2,473	(raie très large)		
	2,280	(111)		
475° C — 30 min	2,562	(110)	2,415	(110) γ
	2,520	(021)		
	2,479	(002)		
	2,285	(111)		
475° C — 1 h	2,565	(110)	2,390	(110) γ
	2,520	(021)		
	2,479	(002)		
	2,285	(111)		
475° C — 3 h 30	2,565	(110)	2,390	(110) γ
	2,520	(021)		
	2,479	(002)		
	2,280	(111)		
475° C — 48 h	2,565	(110)	2,415	(110) γ'
	2,520	(021)	2,366	(103) γ'
	2,479	(002)		
	2,280	(111)		
475° C — 100 h	2,565	(110)	2,415	(110) γ'
	2,520	(021)	2,366	(103) γ'
	2,479	(002)		
	2,280	(111)		

Le tableau 2 groupe les résultats et les diagrammes correspondants sont présentés figure 15.

Nous constatons:

Dès le début de la transformation isotherme, après 1 min à 475° C, la présence de la raie (110) de la phase α , ainsi que celle d'une raie très large recouvrant les positions des raies (021) et (002) α et (110) γ .

Après 30 min, la raie (110) de la phase γ est bien séparée des trois raies de la phase α . Sa position indique que la solution solide γ a une teneur en molybdène de 9 à 10 % en poids.

Après 3 h 30 min, la raie (110) γ a subi un déplacement indiquant une diminution de paramètre de la solution solide et ainsi un enrichissement en molybdène jusqu'à 15 %.

Après 48 h, le dédoublement de la raie (110) γ est observable et après 100 h, il est très net et correspond aux deux raies caractéristiques de la phase γ' .

d. Corrélation entre micrographie rayons X et dureté

La décomposition lamellaire possède une dureté Vickers maximum de 475. Cette valeur n'est jamais dépassée pour les températures de traitement de 550 et 500° C. Il en est tout autrement pour les températures situées juste au-dessus des points M_s : 450–400° C pour l'alliage 4, 475–450° C pour l'alliage 3.

Le maximum de dureté de 570–610 est atteint après des durées de traitement isothermes qui ne font apparaître ni la décomposition perlitique (par micrographie) ni la phase γ' (par diffraction des rayons X). Ce maximum coïncide avec la présence de la phase α répartie sous forme de très fine précipitation dans la matrice γ qui n'est pas à l'équilibre.

Lorsque la décomposition perlitique se développe, la dureté s'abaisse rapidement: par exemple, elle décroît de 570 à 480 dans le cas de l'alliage 3 après 1 h de traitement à 475° C, la proportion de phase perlitique est alors de 20 % environ.

Nous avons observé également des abaisse-

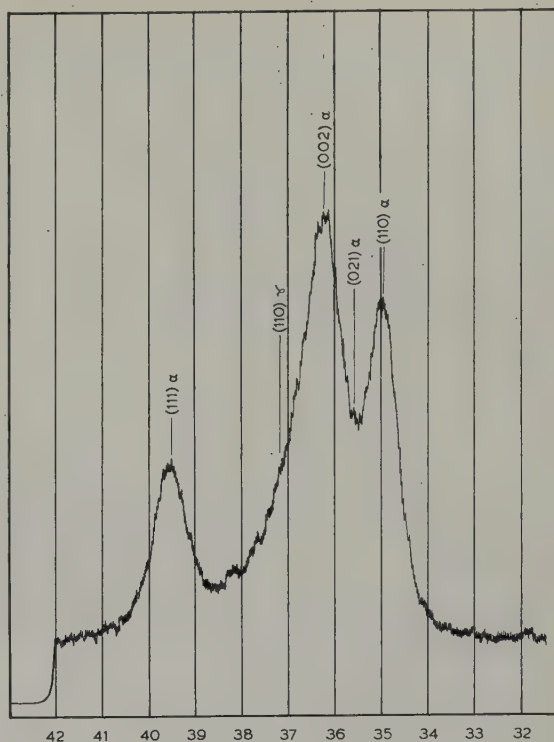


Fig. 15A. 475° C 1 min.

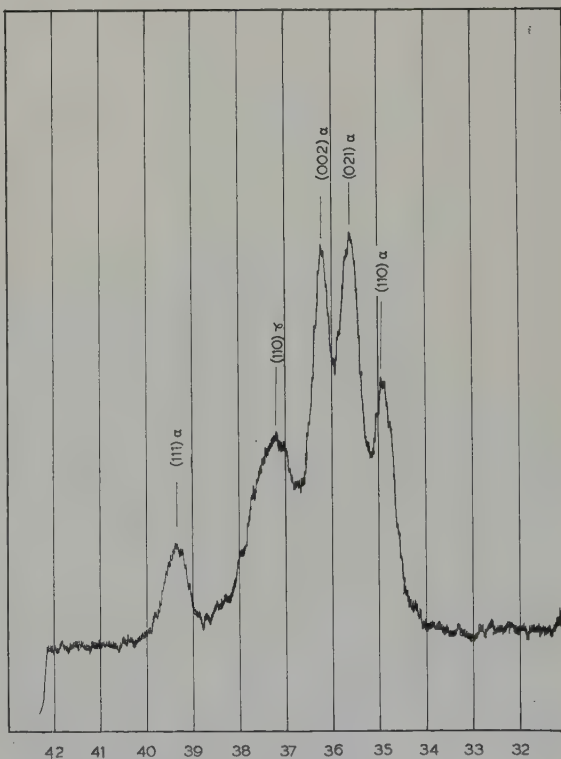


Fig. 15B. 475° C 30 min.

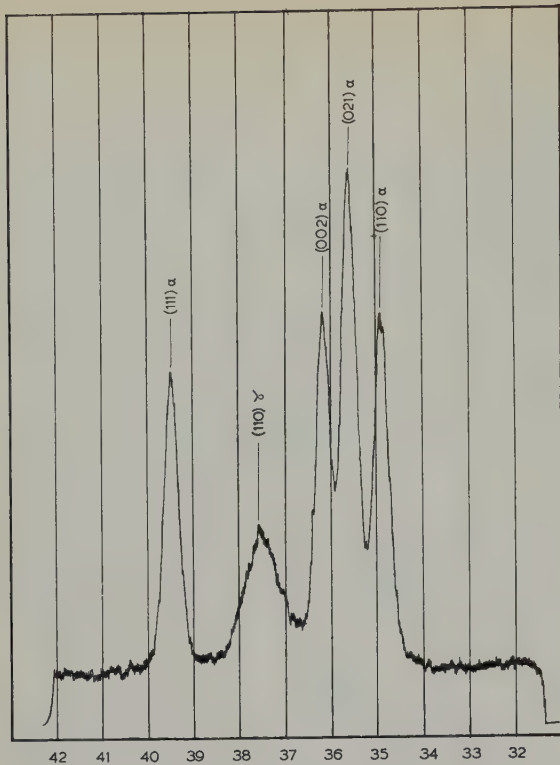


Fig. 15C. 475° C 1 h.

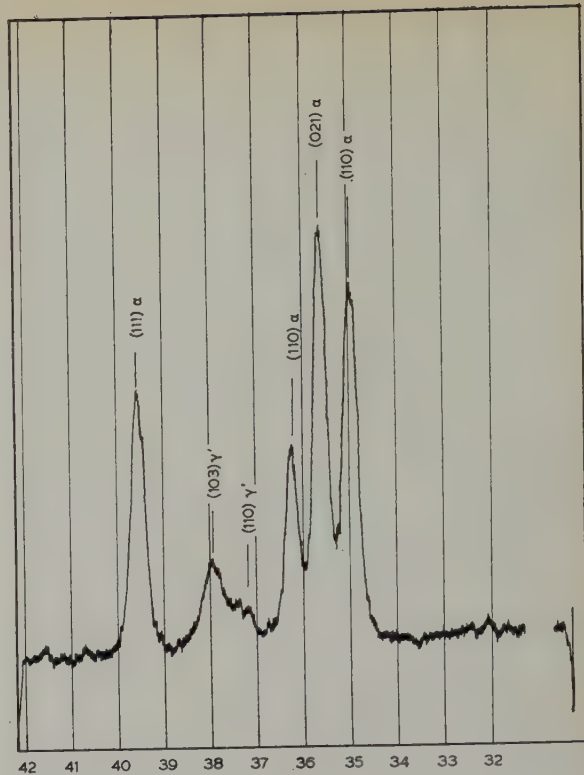


Fig. 15E. 475° C 48 h.

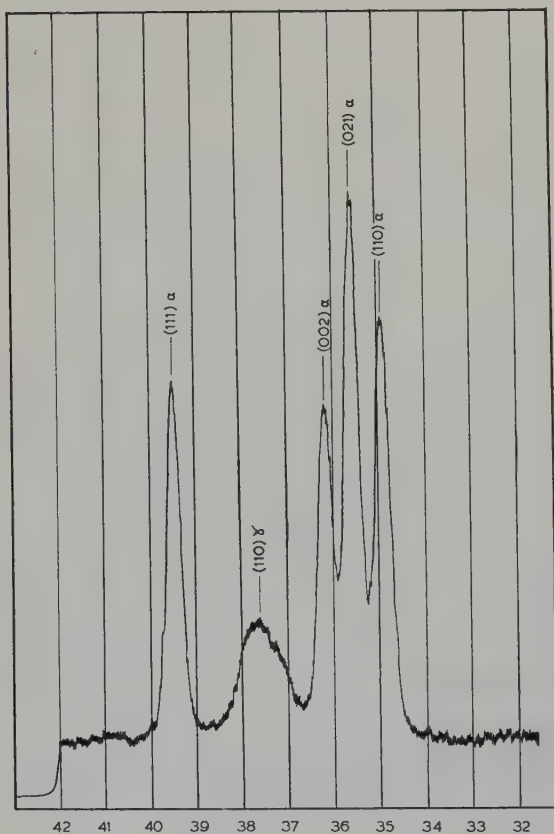


Fig. 15D. 475° C 3 h $\frac{1}{2}$.

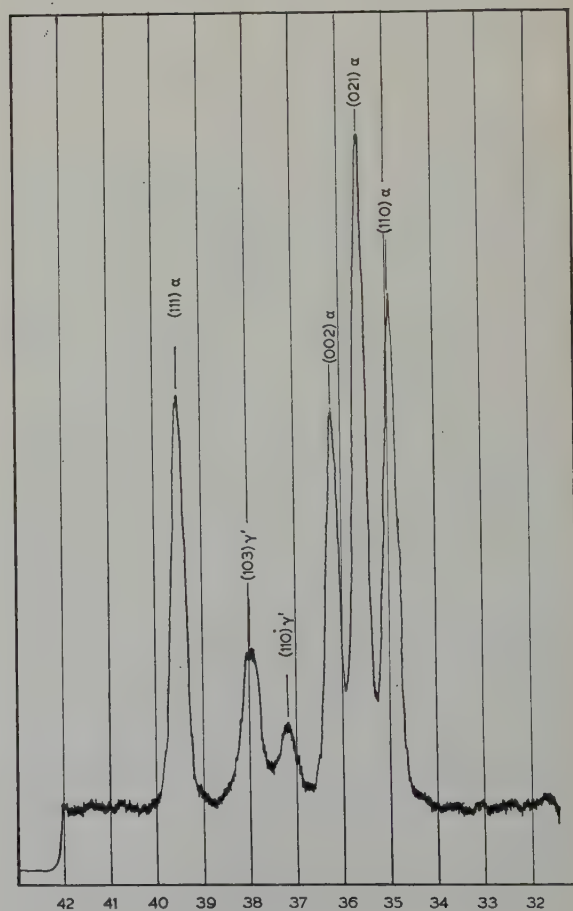


Fig. 15F. 475° C 100 h.

Fig. 15. U-Mo 3 % en poids. Trempes isothermes à partir de 950° C (rayonnement K_{α} du cuivre, $\lambda = 1.5405 \text{ \AA}$).

ments de dureté de 610 à 475 dans le cas de l'alliage 4 qui, après 100 h à 400 et 450° C ne présente que 20 % environ de décomposition.

Les diagrammes de rayons X ont montré que la décomposition perlitique observée par micrographie est en premier lieu constituée par les phases α et γ (de 30 min jusqu'à 48 h de traitement à 475° C). Après 48 h, la solution solide γ a atteint la concentration suffisante pour donner la phase ordonnée γ' et lorsque la

durée de traitement croît de 48 h jusqu'à 100 h la réaction d'ordre $\gamma \rightarrow \gamma'$ se produit lentement et n'apporte plus aucun changement à l'aspect micrographique, (figs. 16, 17, 18).

Les tracés des courbes T.T.T. ont montré que la période d'incubation est très courte: 10 s pour l'alliage 2, inférieure à 1 min pour l'alliage 3 et environ 5 min pour l'alliage 4. Les vitesses de transformation sont d'autant plus faibles que la teneur en molybdène est plus élevée.

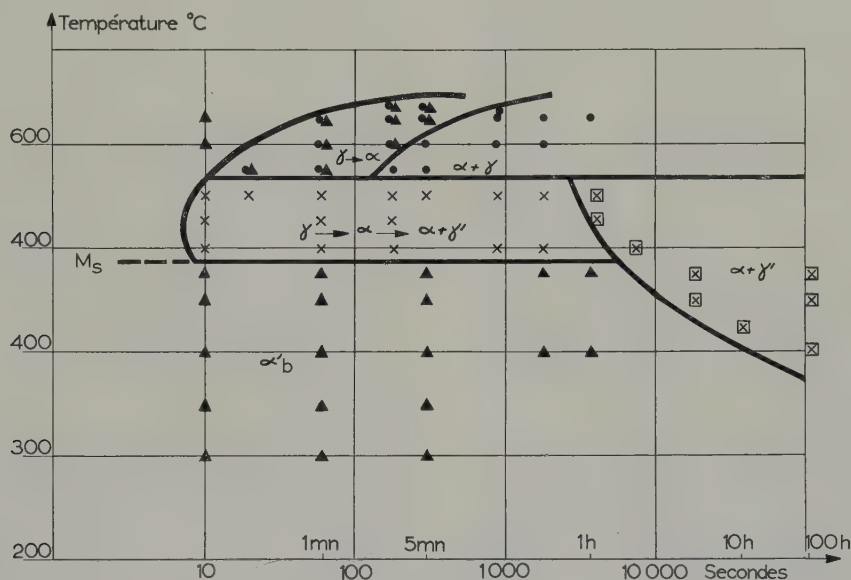


Fig. 16. Alliage U-Mo 2 % en poids. Courbe T.T.T.

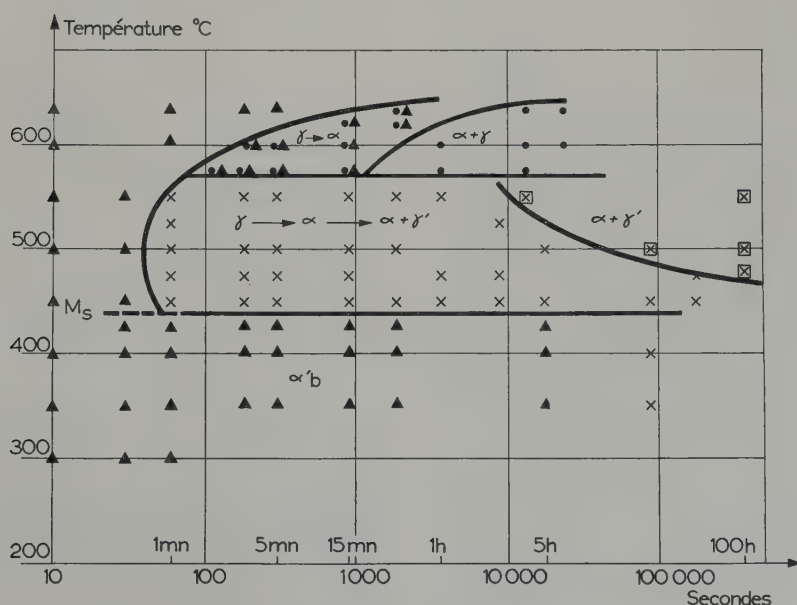


Fig. 17. Alliage U-Mo 3 % en poids. Courbe T.T.T.

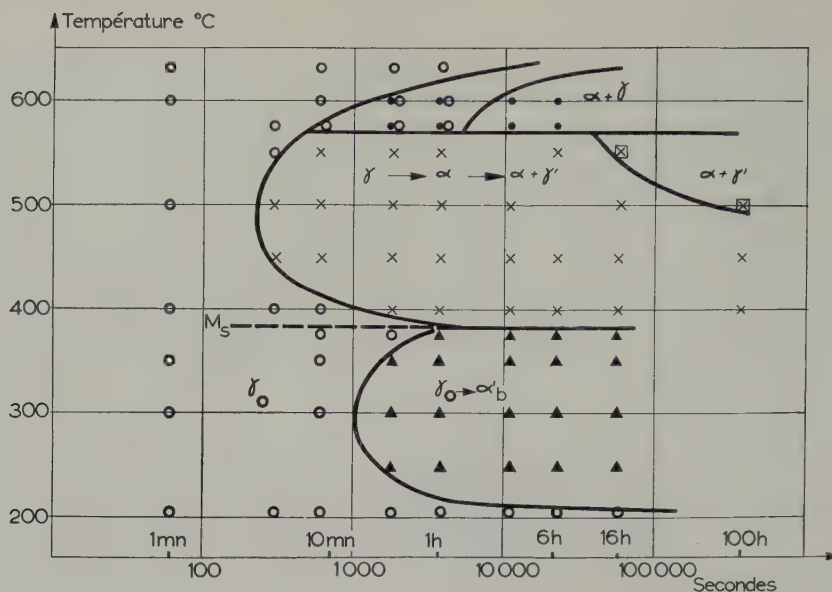


Fig. 18. Alliage U-Mo 4 % en poids. Courbe T.T.T.

Le nez des courbes en C est ainsi situé à 525° C pour l'alliage 2 et 500° C pour les alliages 3 et 4.

Les températures M_s respectives sont:

475/500° C pour l'alliage 2,

425/450° C pour l'alliage 3,

375/400° C pour l'alliage 4.

Dans le cas particulier de l'alliage 4, une phase intermédiaire γ_0 a été mise en évidence; elle se produit lors de la transformation de γ en α_b .

5.3. DISCUSSION

Différents auteurs ont étudié les mécanismes de la décomposition de la phase γ dans les alliages dont la teneur en molybdène permet la rétention de solutions solides γ par trempe^{8,9,10}.

Dans le cas des alliages de teneur 0,5 à 4 % en poids de Mo, la solution solide γ n'est jamais conservée par trempe à la température ambiante. La transformation $\gamma \rightarrow \alpha + \gamma$ est une précipitation classique, elle s'opère lors de trempes isothermes entre 645 et 570° C ou lors de refroidissements continus jusqu'à des vitesses d'environ 100° C/min.

La transformation $\gamma \rightarrow \alpha + \gamma'$ est une décomposition eutectoïde de la phase γ qui s'effectue en deux étapes:

la précipitation de la phase α très rapide,

la réaction d'ordre $\gamma \rightarrow \gamma'$ beaucoup plus lente.

Pour les alliages de forte teneur en molybdène (14 à 15 % en poids) Bostrom et Halteman¹¹) ont observé que la transformation d'ordre $\gamma \rightarrow \gamma'$ s'effectuait avec une vitesse beaucoup plus élevée que celle de la précipitation de la phase α .

Par contre, pour les alliages à 7,1 % en poids, ces auteurs ont constaté l'apparition simultanée des phases α et γ' sous forme d'un eutectoïde lamellaire.

Les alliages étudiés sont situés dans un domaine de plus faible teneur en molybdène (0,5 à 4 % en poids). Nous avons observé également le processus en deux étapes, mais la vitesse de précipitation de la phase α est très grande: elle est complète en quelques minutes, alors que, à la même température la transformation d'ordre $\gamma \rightarrow \gamma'$ est très lente et ne se termine qu'après une centaine d'heures.

Il est nécessaire d'effectuer des traitements isothermes de très longue durée aux températures où la vitesse de diffusion est faible (juste au-dessus des points M_s) pour atteindre un état d'équilibre correspondant à un appauvrissement en molybdène de la phase α . Les atomes de molybdène ainsi libérés contribuent à l'enrichissement de la matrice γ , qui lorsqu'elle atteint la concentration suffisante donne la réaction d'ordre $\gamma \rightarrow \gamma'$.

4. Comparaison des alliages 2, 3 et 4 avec l'alliage 0,5

Le diagramme d'équilibre montre que l'alliage 0,5 se trouve en phase β entre 645 et 690° C.

La trempe directe à partir de la phase γ : 900 ou 950° C permet une rétention de la phase β , il en est de même pour toutes les trempes isothermes de durée maximum 20 s aux températures comprises entre 645° C et la température ambiante.

Ainsi les courbes de transformations isothermes correspondent à la transformation d'une solution solide β ¹).

Entre 645° C et 360° C cette transformation se fait par un mécanisme de germination et croissance, c'est la décomposition eutectoïde $\beta \rightarrow \alpha + \gamma$, la microstructure est formée de grains réguliers et est comparable à celle de l'uranium pur recristallisé.

Au-dessous de 360° C la transformation se fait par cisaillement et donne une phase α martensitique α'' [†] 1).

Les courbes de transformation en refroidissement continu ont montré pour cet alliage un abaissement très important de la température de transformation qui est fonction de la vitesse de refroidissement (fig. 19).

Les examens micrographiques montrent: Après refroidissements à des vitesses de 2,5 à 10° C/min, une structure à très gros grains α , irréguliers avec une décomposition eutectoïde à lamelles très espacées ($\alpha + \gamma$).

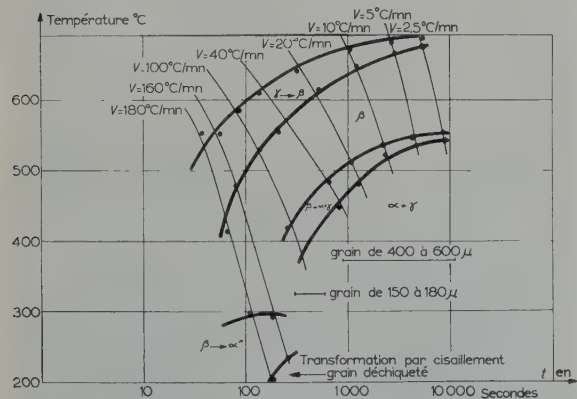


Fig. 19. Alliage U-Mo 0,5 % en poids. Courbe de transformation en refroidissement continu.

[†] α'' d'après nouvelle nomenclature.

Après des refroidissements à des vitesses comprises entre 20 et 100° C/min, la taille du grain diminue d'une manière importante et, dans ce dernier cas, la structure est à grains réguliers aux contours arrondis dont la taille n'excède pas 150 μ .

Après des refroidissements à des vitesses de 160 et 180° C/min, la structure possède des grains très déchiquetés dont la taille est très irrégulière. La différence d'aspect micrographique en corrélation avec la discontinuité dans la courbe de transformation montre que, pour les vitesses inférieures à 160° C/min, la transformation s'opère par germination et croissance et pour les vitesses voisines de 160° C/min, la transformation se fait par cisaillement.

Les hystérésis de chacune des transformations et les résultats des examens micrographiques sont groupés dans le tableau 3.

Nous observons ainsi deux processus de formation de la phase α aux températures peu inférieures à la température d'équilibre: 645° C.

Dans le premier cas (alliages 2, 3, 4) la phase α provient d'une précipitation lamellaire dans la matrice γ , la microstructure est formée de lamelles alternées α et γ formant des paquets de même orientation cristallographique, et la taille du grain est indépendante de la température et de la durée de la transformation isotherme.

La vitesse de précipitation des lamelles est supérieure à leur vitesse de croissance: cette forme de précipitation correspond généralement à des précipités dont deux dimensions sont à peu près équivalentes, et la troisième beaucoup plus faible, il existe une taille optimum, et dans le cas des alliages uranium-molybdène les lamelles ne dépassent jamais 60 μ de longueur et 2 μ de largeur.

Dans le second cas (alliage 0,5) la phase α provient de la transformation eutectoïde d'une solution solide β et la taille du grain dépend de la température et de la durée de la trempe isotherme.

Les transformations au cours de refroidisse-

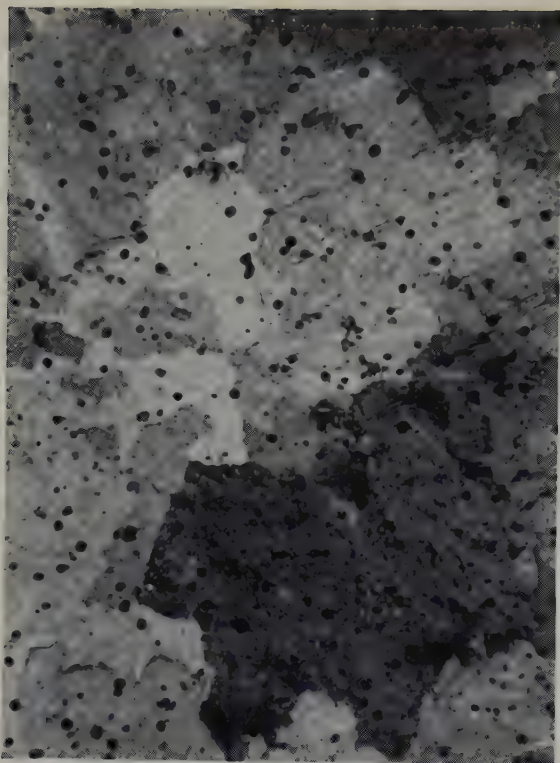


Fig. 21. U-Mo 0.5 % en poids. Brut de coulée. $\times 150$.



Fig. 23. U-Mo 1 % en poids. Brut de coulée. $\times 150$.

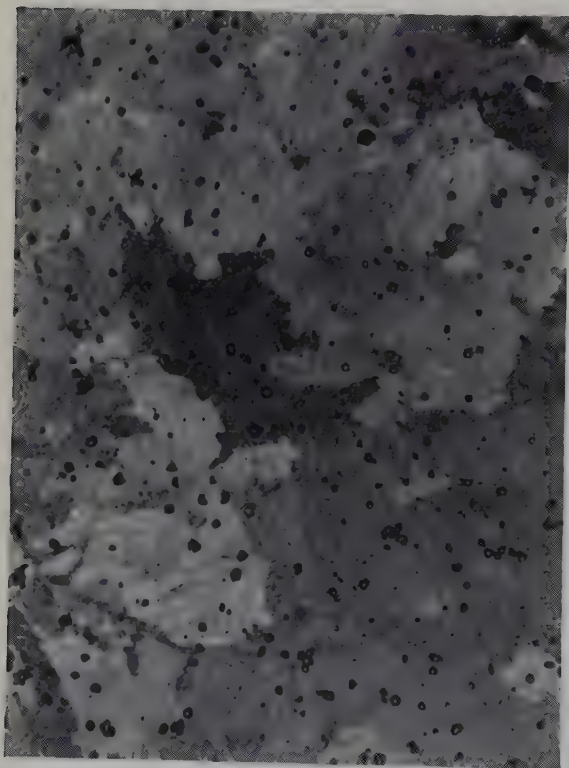


Fig. 22. U-Mo 0.8 % en poids. Brut de coulée. $\times 150$.

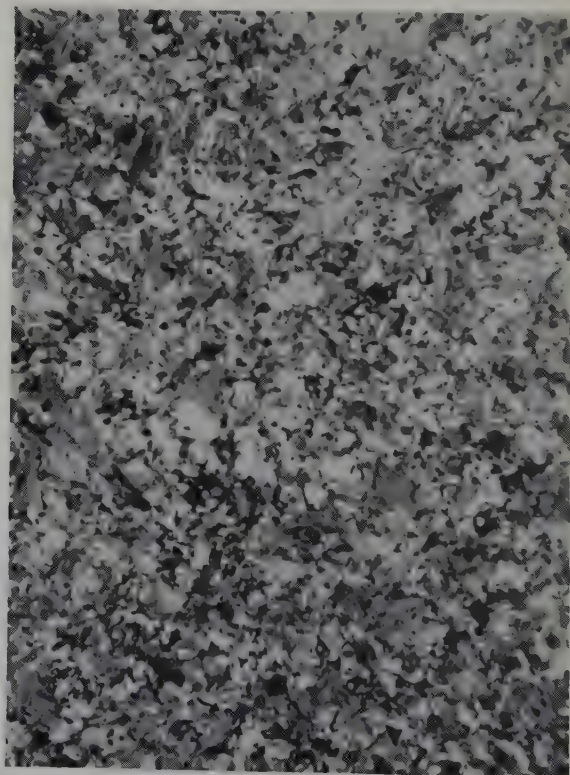


Fig. 24. U-Mo 3 % en poids. Brut de coulée. $\times 150$.

TABLEAU 3 — U-Mo 0,5 %. Transformations en refroidissement continu

Vitesse moyenne de refroidissement (° C/min)	Transformation $\gamma \rightarrow \beta$			Transformation $\beta \rightarrow \alpha$			Aspect micrographique
	Début (° C)	Fin (° C)	Retard (° C)	Début (° C)	Fin (° C)	Retard (° C)	
2,5	689	676	66	554	544	91	Gros grains: 400 à 600 μ
5	683	668	72	547	534	98	Gros grains: 400 à 600 μ
10	674	648	81	535	524	110	Gros grains: 400 à 600 μ
20	635	615	120	510	475	135	Gros grains: 400 à 600 μ
40	610	555	145	480	450	165	Gros grains hétérogènes
100	585	530	170	420	380	225	Grains de 150 à 180 μ
160	550	481	205	290	236	355	Grain déchiqueté transformation martensitique
180	554	413	201	300	200	345	Grain déchiqueté transformation martensitique

ments continus à différentes vitesses ont montré des caractéristiques identiques à celles des transformations isothermes.

Dans le cas des alliages 1, 2, 3, 4¹⁾ après des vitesses de refroidissement allant de 2,5 à 100° C/min, la microstructure présente un grain fin correspondant à une décomposition lamellaire ($\alpha + \gamma$) identique à celle qui est observée après transformation isotherme aux températures comprises entre 645 et 570° C.

Dans le cas de l'alliage 0,5, pour des vitesses de refroidissement allant de 2,5 à 100° C/min, la microstructure présente un grain α grossier de 400 à 600 μ et pour des vitesses de 100° C/min la taille du grain est d'environ 150 μ , l'affinage du grain reste ainsi faible.

Les courbes (fig. 20) montrent la taille du grain en fonction de la teneur en molybdène, elles font apparaître un très net changement de pente pour une teneur peu inférieure à 1 %.

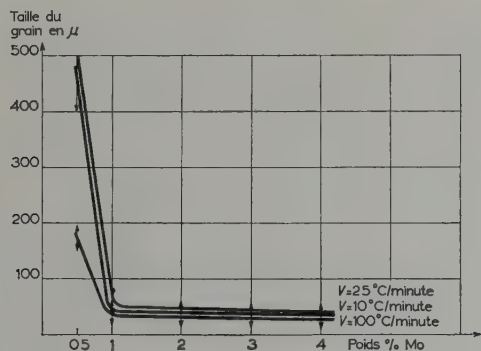


Fig. 20. Variation de la taille du grains en fonction de la concentration en molybdène.

Lors de l'élaboration d'alliages sous forme de barreaux ou de tubes coulés, pour lesquels les vitesses moyennes de refroidissement sont de 20 à 60° C/min, nous avons observé pour les teneurs en molybdène 0,5 et 0,8 % en poids, des microstructures présentant un grain grossier et irrégulier (figs. 21–22), alors que dans le cas des alliages de teneur 1, 2, 3 et 4 % en poids de Mo (figs. 23–24), la microstructure présente un grain très fin.

Par ailleurs, les résultats des transformations en refroidissement continu ont permis de tracer les courbes (fig. 25) montrant les retards de la transformation (645° C à l'équilibre) en fonction de la vitesse de refroidissement.

Dans le cas des alliages 1 à 3, l'hystérésis de la transformation est d'autant plus importante que la teneur en molybdène est plus élevée. Dans le cas de l'alliage 0,5, l'hystérésis est toujours plus importante que dans les cas

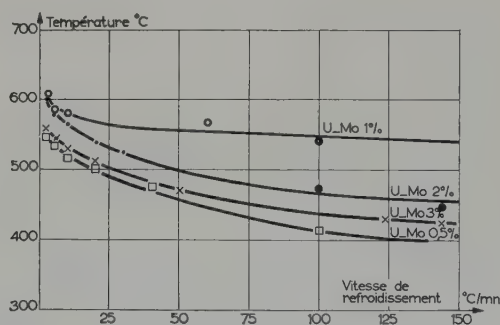


Fig. 25. Abaissement de la température de transformation en fonction de la vitesse de transformation.

précédents; le molybdène est, à cette teneur, un stabilisant de la phase β et abaisse d'une façon importante la température de transformation. L'affinage du grain qui en résulte reste faible: 150 μ .

Lorsque la vitesse de refroidissement est beaucoup plus importante (trempe), la phase β est conservée à la température ambiante. Il n'y a ainsi pas de possibilité d'obtenir un affinage du grain après refroidissement continu, même rapide à la température ambiante.

Une corrélation a pu être établie avec le diagramme d'équilibre, permettant de différencier les alliages de teneur inférieure à 0,9 % en poids de ceux dont la teneur va de 1 % en poids jusqu'à la teneur en Mo minimum permettant la rétention de solutions solides γ métastables à la température ambiante.

La limite 0,9 % en poids correspond au maximum de solubilité solide en phase β .

7. Conclusion

Nous avons établi les tracés des courbes T.T.T. des alliages de teneur en molybdène 2, 3, 4 % en poids et décrit, en particulier, les transformations s'opérant par germination et croissance.

La transformation de la solution solide γ conduit à une décomposition lamellaire ($\alpha + \gamma$) entre 645 et 570° C et à une décomposition eutectoïde ($\alpha + \gamma'$) entre 570° C et la température M_s ; cette dernière décomposition présente des caractéristiques très particulières.

Elle débute par une précipitation très fine de phase α dans une matrice γ déformée. La vitesse de réaction est très grande et la phase α métastable apporte le durcissement structural à l'alliage.

L'étape suivante, très lente, correspond à l'enrichissement de la matrice γ jusqu'à la teneur correspondant à celle de la phase ordonnée γ' .

Ces différences de vitesses considérables sont spécifiques des alliages de faible teneur en molybdène pour lesquels la trempe ne stabilise

pas de solution solide γ à la température ambiante.

Par ailleurs, la transformation des alliages de teneur inférieure à 0,9 % en poids montre la formation de phase α à partir de solutions solides β , la microstructure présente alors des grains grossiers et hétérogènes.

Pour les vitesses de refroidissement correspondant à celles des alliages coulés, la transformation présente une hystérésis très importante et la phase β est maintenue jusqu'à 450–500° C.

Ceci est un inconvénient notable pour l'élaboration d'un matériau combustible. Si la transformation $\beta \rightarrow \alpha$ prend place à une température très basse, les différences de volume qui l'accompagnent peuvent produire des fissurations (ceci pourrait être le cas avec des tubes très minces).

Dans le cas des alliages à 1, 2 et 3 % en poids, un tel inconvénient n'existe pas et une isotropie statistique est conférée à la microstructure par la décomposition lamellaire fine.

Bibliographie

- ¹⁾ J. Lehmann, Saclay (France) rapport CEA 920
- ²⁾ H. A. Saller, F. A. Rough et D. A. Vaughan, Battelle Memorial Institute (USA) Report, BMI-72 (1951)
- ³⁾ H. A. Saller, F. A. Rough et D. G. Bennett, Battelle Memorial Institute (USA) Report, BMI-730 (1952)
- ⁴⁾ E. K. Halteman, Acta Crystallographica 10 (1957) 166
- ⁵⁾ S. T. Konobevsky, Deuxième Conférence de Genève, 15/P/2230 (1958)
- ⁶⁾ A. E. Dwight, Argonne (USA) Report, ANL-5717 (1958)
- ⁷⁾ J. Lehmann, C.R. Acad. Sc. Paris 248 (1959) 2098
- ⁸⁾ R. J. van Thyne et D. J. McPherson, Trans. ASM 49 (1957) 576
- ⁹⁾ G. Donze et G. Cabane, Saclay (France). Rapport DMCA 685 (1959), à paraître dans la "Revue de Métallurgie"
- ¹⁰⁾ R. F. Hills, D. R. Harries, D. J. Hodkin et M. B. Waldron, Harwell (UK) Report, AERE M/R 2840
- ¹¹⁾ W. A. Bostrom et E. K. Halteman, Proc. 2nd Nuclear Engineering and Science Congress (USA), part II (1957) 184

THE HIGH TEMPERATURE OXIDATION OF BERYLLIUM

PART I.

IN DRY OXYGEN

D. W. AYLMOORE, S. J. GREGG and W. B. JEPSON

Department of Chemistry, University of Exeter, Exeter, UK

Received 19 January 1960

The kinetics of the oxidation of French Flake beryllium in dry oxygen have been studied for 300 hour periods at temperatures in the range 500°–700° C using a vacuum microbalance. At temperatures up to and including 650° C, the oxidation is protective and the rate decreases continuously with time, reaching a value of 0.02–0.04 $\mu\text{g}/\text{cm}^2$ h after 300 hours. At 750° C the rate first decreases and then increases with time, indicating a breakaway reaction and subsequent non-protective oxidation. The curves of weight gain against time show small discontinuities which are ascribed to cracking and healing of the oxide film.

La cinétique de l'oxydation de paillettes de beryllium français dans l'oxygène sec a été étudiée pendant des durées de 300 heures dans l'intervalle de température 500°–700° C en utilisant une microbalance sous vide. Aux températures jusqu'à 650° C inclus, l'oxydation est protectrice et la vitesse diminue de façon continue avec le temps en atteignant une valeur de 0,02–0,04 $\mu\text{g}/\text{cm}^2$ h après 300 heures. A 750° C la vitesse décroît d'abord puis augmente avec le temps, ce qui est

caractéristique d'une réaction de rupture de film ("breakaway") et d'une oxydation ultérieure non-protectrice. Les courbes d'augmentation de poids en fonction du temps montrent de petites discontinuités qui sont attribuées à une fissuration et à un colmatage alterné du film d'oxyde.

Die Kinetik der Oxydation von französischem Beryllium in trockenem Sauerstoff wurde mit Hilfe einer Vakuum-Mikrowaage während einer Dauer von 300 Stdn. im Temperaturbereich von 500°–700° C untersucht. Bei Temperaturen bis 650° C verläuft die Oxydation selbsthemmend mit stetig abnehmender Geschwindigkeit, wobei nach 300 Stdn. ein Wert von 0,02 bis 0,04 $\mu\text{g}/\text{cm}^2$ h erreicht wird. Bei 750° C fällt die Geschwindigkeit mit wachsender Versuchszeit zunächst ab und steigt dann wieder an, was auf Aufreissen der Oxydschicht und eine anschliessend ablaufende Bildung eines nicht schützenden Oxyds hinweist. Die Gewicht-Zeit-Kurven zeigen kleine Unregelmässigkeiten, die der Bildung und Ausheilung von Rissen im Oxydüberzug zugeschrieben werden.

1. Introduction

The metal beryllium is proposed as the canning material in the advanced gas-cooled reactor so that there is considerable interest in its resistance to corrosion in the gases carbon dioxide, carbon monoxide and oxygen, both dry and in the presence of small concentrations of water vapour.

This paper represents the first part of a comprehensive study of the high temperature oxidation of French Flake beryllium in the following gases, both dry and in the moist condition: oxygen, carbon monoxide, carbon

dioxide and carbon monoxide-carbon dioxide mixtures.

Published work on the kinetics of the reaction of beryllium with oxygen is very limited; Gulbransen and Andrew¹⁾ have made a systematic investigation at temperatures in the range 350° C to 950° C but with the exception of a single run at 500° C, the period of oxidation was only 2 hours. Similarly the measurements of Cubicciotti²⁾ over the temperature range 885° C to 970° C were only continued for 100 min.

In the present study, which covered periods

extending up to 300 hours and the temperature range 500°–750° C, the rate of oxidation has not, in contrast to the earlier work, been found to follow a parabolic rate law over any part of the curve, including the first few hours. Indeed, at temperatures up to and including 650° C the rate decreases rapidly with time to reach a very small value, whilst at 750° C a breakaway reaction occurs, after which the oxidation is non-protective.

2. Experimental

The beryllium was obtained from AERE, Harwell, in the form of rectangular pieces (4×1.5 cm and 3.5×1 cm) which had been machined from 0.75 mm sheet and polished with alumina; each sample had a 0.8 mm diameter hole drilled through the top of the face. The beryllium sheet had been prepared from electrolytic French flake which had been vacuum cast, turned to swarf, and ball-milled. The powder was rolled to sheet at 1000° C in a mild steel sheath and the surface finally ground.

The main impurities present were in wt per cent: BeO, ≤ 0.3 ; Fe, 0.04; C, 0.03; Al, ≤ 0.07 ; Ni, 0.005; Cr, 0.003; Si, ≤ 0.006 ; Mg, 0.002; Na, 0.002; N, 0.002 with a trace of Mn, Li, K, Sn and Cl.

In considering the choice of a suitable method of surface preparation, abrasion was rejected because the precautions necessary to combat the health hazard could not be taken, while electrolytic polishing would have required a relatively large current³⁾ (2 A/cm²) and the samples were not suitable for a screw-in electrode. Chemical polishing in a solution⁴⁾ containing 180 cc of phosphoric acid (89 %), 23 g of chromic acid and 11 cc of concentrated sulphuric acid proved satisfactory; the procedure was to immerse the sample in the polishing bath at 100° C for 30 sec and then rinse with water and then acetone; the thickness of metal removed during the polishing was about 7 μ .

The oxidation was followed by measuring the weight gain of the beryllium sample on a vacuum microbalance⁵⁾, the experimental arrangement being similar to that previously

described⁶⁾. A weight gain of 1.7 μ g could be detected, which with a sample size of 4 cm \times 1.5 cm is equivalent to an increase in film thickness of 5 Å [density of beryllium oxide = 3.025 g/cm³ ¹⁾].

For an oxidation run, the sample was first out-gassed at room temperature to a pressure of 10^{-6} mm; the furnace was then switched on and the sample allowed to reach reaction temperature in a time which varied from 45 min for 500° C to 75 min for 750° C. After an initial loss in weight corresponding to a gas content of 0.02 wt per cent there was no detectable increase in weight, due to possible gettering, neither did any evaporation of metal occur²⁾. After the sample had been at reaction temperature for about 15 min, oxygen was admitted to a pressure of 10 cm, the mercury raised into the cut-off to isolate the balance case from the pumps and readings taken at suitable intervals.

3. Results

Curves for the oxidation of beryllium over the first 300 hours are shown in figs. 1 and 2 as the weight gain of the sample w in μ g/cm² against the time of oxidation t in hours; the thickness of the oxide layer (assuming a surface roughness factor of unity) in Ångstrom units is obtained by multiplying w by 51.7. One run of 300 hours' duration was carried out at 500° C, 550° C, 600° C and 650° C and two at 700° C; at 650° C a second run was continued for 500 hours. At 750° C, the highest temperature studied, the range of the balance was exceeded

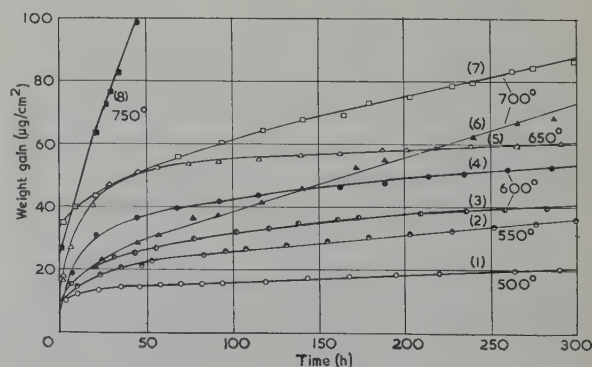


Fig. 1. Oxidation of beryllium at temperatures in the range 500–750° C.

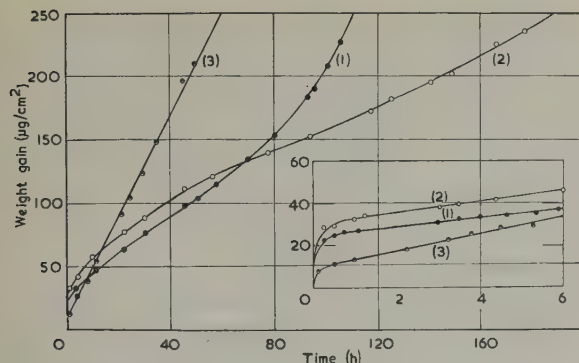


Fig. 2. Oxidation of beryllium at 750° C.

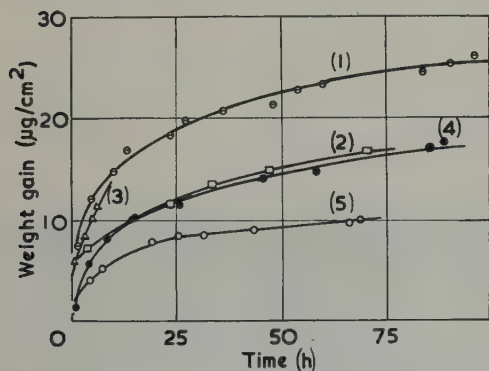


Fig. 3. Oxidation of beryllium at 550° C. Comparison of chemically polished samples (curves 1 and 2) with "as-received" sample (curves 3, 4 and 5).

for each of the three runs well before the end of the 300 hour period (fig. 2).

There was considerable divergence between the results for any one temperature (e.g. curves 3 and 4 of fig. 1) and this is brought out by a number of repeat runs at 550° C (fig. 3) for both chemically polished samples (curves 1 and 2) and "as-received" samples (curves 3, 4 and 5); the considerable spread between repeat runs makes it impossible to decide if one method of surface preparation leads to a higher rate of oxidation than the other. Since an earlier study of the oxidation of aluminium⁶), using the same apparatus and general techniques, gave good agreement between repeat runs, often within a few per cent, the poor reproducibility obtained in the present work must be attributed to variation in impurity content or physical state of the surface of the metal.

It is clear that the curves fall into two groups according to the temperature, those for the first range, 500°–650° C, being distinguished from those for 750° C by the rate falling off with time to reach a very small value after long periods (e.g. the rate at 500° C at 300 hours is 0.2 $\mu\text{g}/\text{cm}^2 \text{ h}$, corresponding to the addition of only one atomic layer of oxide every 3–4 hours). At 750° C, on the other hand, in two of the runs (curves 1 and 2, fig. 2) the rate first decreased and then increased with time, indicating a breakaway reaction, while in the third run (curve 3) the oxidation rate decreased to become constant (4 $\mu\text{g}/\text{cm}^2 \text{ h}$) after several hours. The amount of oxidation at 750° C is considerably greater than that for the 500°–650° C range of temperatures, a weight gain of 200 $\mu\text{g}/\text{cm}^2$ being reached in one run after 50 hours' oxidation. It appears that 700° C represents a transition temperature between protective and non-protective oxidation; thus one run (curve 7, fig. 1) followed the 500°–650° C pattern (though the rate at 300 hours was somewhat greater, 0.13 $\mu\text{g}/\text{cm}^2 \text{ h}$ as compared with 0.04 $\mu\text{g}/\text{cm}^2 \text{ h}$ at 550° C, 600° C and 650° C) whereas the second run (curve 6, fig. 1) was similar to that of curve 3 (fig. 2) at 750° C.

An interesting feature of the curves is the presence of small discontinuous weight changes which are shown up on plotting the experimental data on a scale commensurate with the experimental precision (fig. 4); these discontinuities are definitely in excess of experimental error and are not instrumental in origin (cf. curve 5 for the oxidation of aluminium at 500° C, obtained on the same apparatus). As far as can be judged, the jerky oxidation was a feature also of the early part of the runs although the relatively large rate of oxidation there tends to obscure it.

These discontinuities make it difficult to decide whether the oxidation is truly protective in the range 500°–650° C; in particular, it is not possible to say whether the rate of oxidation at a given temperature tends towards zero so that the oxide layer approaches a limiting thickness, or whether the rate tends to a finite value so that the oxide layer continues to thicken

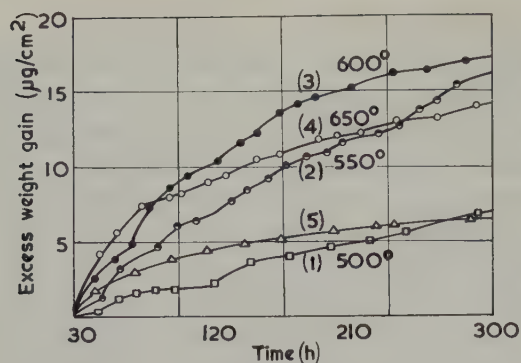


Fig. 4. Oxidation of beryllium at 500° C, 550° C, 600° C and 650° C, showing the discontinuous weight changes. The weight gain in excess of that after 30 h is plotted against time. The curves should be compared with that for the oxidation of aluminium at 500° C (curve 5) determined on the same apparatus.

indefinitely. Certainly in the one run at 600° C which was continued for 500 hours, the discontinuities were still occurring at the end of the period, but the fact that the rate fell from 0.04 $\mu\text{g}/\text{cm}^2 \text{ h}$ at 300 hours to 0.027 $\mu\text{g}/\text{cm}^2 \text{ h}$ at 500 hours suggests that the rates given above for 300 hours at the various temperatures are not limiting values.

Although 750° C was the highest temperature studied systematically, the furnace controller failed during the course of one run and the temperature rose overnight to 1100° C. The beryllium sample was twisted and covered with white oxide over part of its surface.

TABLE 1

Interference colours on oxidised metal specimens

Temp. (° C)	Interference colour
500	None. Loss of lustre
550	None. Loss of lustre
600	Blue and green
650	Straw
700	Yellow and purple
750	Dark grey and various colours

Most of the samples showed interference colours after oxidation for 300 hours at the various temperatures (table 1). These varied in colour over the sample surface, indicating an oxide layer of non-uniform thickness. Samples

oxidised at 700° C, and particularly at 750° C, frequently bent during the course of the run which again indicates non-uniform oxidation; microscopic examination of these samples indicated that the oxide surface was severely blistered (fig. 5).

4. Discussion

There is little doubt that the oxide layer on beryllium grows by the diffusion of Be^{++} ions and a corresponding flow of electrons through its thickness, so that new oxide is built up at the gas/oxide interface⁷); in addition to the diffusion itself, there are boundary processes to be considered, viz. the dissolution of metal ions in the oxide (occurring at the metal/oxide interface) and the reaction of Be^{++} ions with chemi-

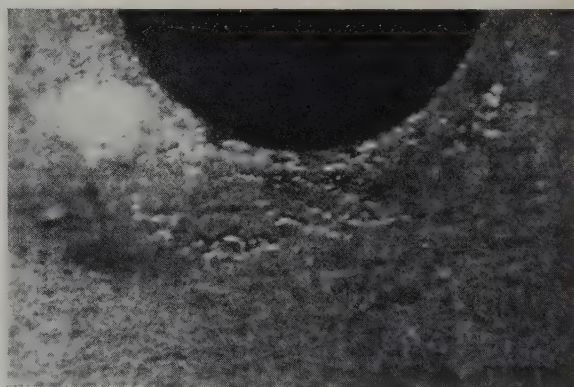


Fig. 5a

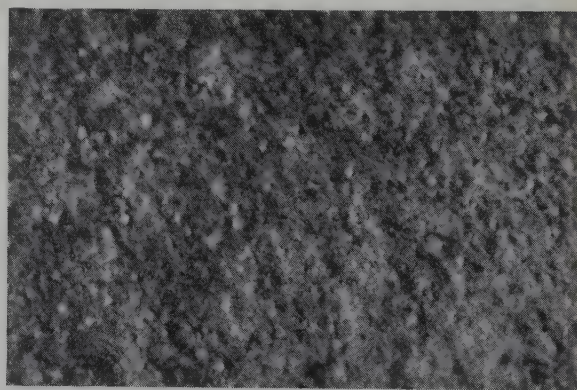


Fig. 5b

Fig. 5. Showing blistering in the oxide layer on beryllium after oxidation (a) in run 6 of fig. 1 at 700° C and (b) in run 1 of fig. 2 at 750° C.

sorbed oxygen (at the gas/oxide interface). The rate of oxidation will be controlled by the slowest of these three processes.

4.1. THE DIFFUSION PROCESS

We consider first the diffusion process which could in principle be either a "volume" diffusion of Be^{++} ions between interstitial positions or a "surface" diffusion of Be^{++} ions along grain boundaries. If the former is rate controlling the oxidation can be expected to follow two parabolic rate laws in succession^{8,9}) corresponding to migration under an electrostatic field and under a concentration gradient respectively. Gulbransen and Andrew¹) did in fact find a single parabolic law to hold over the two-hour period of their experiments with a slight deviation over the initial stages; and in longer run (55 h at 550°C) results fitting two intersecting parabolic curves were obtained. Cubicciotti²) also found that a parabolic law was obeyed over the 100 min period of his experiments, but the temperature range 885°–970°C was considerably above that of the present work.

None of the present results, on the other hand, showed conformity to a parabolic rate law over any part of the curve including the first few hours. It must be realised, however, that the presence of foreign ions in the oxide layer would profoundly modify the rate of diffusion of Be^{++} ions across its thickness by altering the concentration of interstitial Be^{++} ions and hence their gradient across the oxide layer. If, as seems highly probable, the impurity concentration in the oxide varied during the course of the run by diffusion of impurity ions either in or out of the oxide layer, the fundamental assumptions made in deriving the parabolic rate law would no longer be valid. It follows therefore, after taking into account the relatively large impurity content of the metal, that the lack of conformity to a parabolic rate law does not necessarily mean that the diffusion of Be^{++} ions across the oxide layer is not the rate controlling step.

These arguments, of course, equally apply to surface diffusion *provided* that the number of

grain boundaries per unit volume of oxide remains constant during the oxidation process; if, however, the individual oxide crystallites were to sinter together as time progressed, then the general shape of the curves up to and including 650°C could be qualitatively explained in terms of a reduction in the number of these favourable paths for diffusion. However, electron diffraction investigation¹⁰) of the oxide layer formed on beryllium after 30 minutes' oxidation at various temperatures, indicates the presence of crystallites whose diameters vary from tens of Ångströms at 300°C to some thousands of Ångströms at 800°C; comparison with the weight gains of the present work shows that the crystallite size, even after 30 minutes' oxidation, is comparable with the thickness of the oxide layer itself. Thus any explanation of the subsequent decrease in rate in terms of grain growth can be discounted.

Turning now to a process at one or other of the two interfaces as the possible slow step in the oxidation, reaction at the gas/oxide interface between Be^{++} ions and chemisorbed oxygen would appear to be excluded since it should lead to a constant rate of oxidation. The other possibility that the rate is controlled by the dissolution of Be^{++} ions in the oxide at the metal/oxide interface should, as Uhlig¹¹) has shown, lead to a logarithmic rate law

$$w = k_1 \log_{10} (1 + at) \quad (1)$$

since electron flow from metal to oxide will in its turn hold back the slower moving Be^{++} ions. (k_1 is the logarithmic rate constant and a is a second constant.) For values of a such that $a \gg 1$, eq. (1) reduces to

$$w = k_1 \log_{10} t + k_1 \log_{10} a \quad (2)$$

and reference to fig. 6 will show that the present results at any given temperature conform only moderately well to eq. (2) over the first parts of the curve, while significant deviations occur at the longer times.

It is thus seen that the arguments developed above do not permit any firm conclusion to be

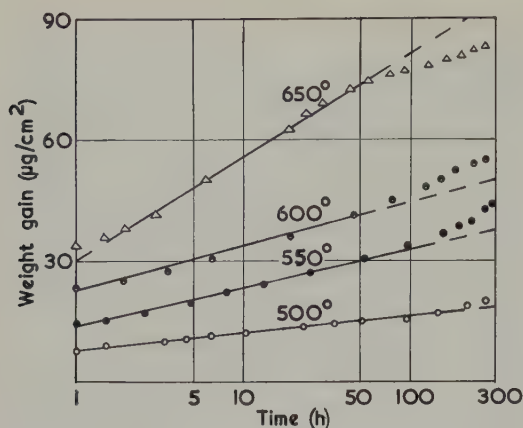


Fig. 6. Oxidation of beryllium at temperatures in the range 500° C to 650° C. The data are tested for conformity to eq. (1) by plotting w against $\log_{10} t$. (The curves at 550° C, 600° C and 650° C are displaced from that at 500° C by 7.5, 15 and 22.5 $\mu\text{g}/\text{cm}^2$ respectively.)

drawn as to the nature of the rate controlling process but on balance, the evidence would appear to suggest that the rate of oxidation is controlled by the rate of diffusion of Be^{++} ions across the oxide layer and that the marked deviations from the parabolic law occur because the chemical composition of the oxide film changes with time.

4.2. DISCONTINUOUS OXIDATION

There are few examples¹²⁾ of discontinuous oxidation in the literature and the phenomenon appears to be more common in the oxidation of alloys than of pure metals. Caplan and Cohen¹²⁾ established that the periods of accelerated oxidation encountered in the oxidation of iron-chromium alloys were due to the accumulation of silica at the metal/oxide interface, whereby the scale became isolated from the metal and the discontinuity is the result of re-oxidation after the scale has cracked.

With beryllium the discontinuities are best interpreted along lines similar to those suggested by Tylecote¹³⁾ for copper, namely that the oxide layer undergoes stress relief by blister formation with associated formation of cracks sufficiently wide to admit molecular oxygen; the abrupt weight gains thus correspond to the

formation of these cracks and their subsequent healing up. The existence of stress in the oxide layer is evidenced by the bending of the samples during oxidation at 700° C and 750° C (presumably because the stress relief is non-uniform) whilst the blistering of the layer (fig. 5) indicates that the stress is compressional. The stress may result from compositional changes in the oxide layer, particularly over the flat part of the curve when the composition of the film is presumably approaching its equilibrium value; an alternative view, which, however, is open to criticism¹⁴⁾, is that the compression derives from the fact that the oxide-to-metal volume ratio for beryllium is 1.7 and therefore greater than unity¹⁵⁾.

4.3. BREAKAWAY

It now remains to discuss the breakaway (curves 1 and 2, fig. 2) which of course marks the beginning of non-protective oxidation. Scott¹⁰⁾ has inferred that the characteristic growth of oxide needles and platelets from the oxide surface during the oxidation of beryllium in room air at 600° C and above is evidence for non-protective oxidation. It is difficult to see why the growth of needles above the surface of the oxide layer should render the layer itself non-protective: there are many cases of whisker growth from a protective oxide layer¹⁶⁾. In the opinion of the present authors, breakaway is most plausibly explained by the development of cracks in the oxide layer over a wide area.

5. Conclusions

1. Experiments of 300 hours' duration have shown that at temperatures up to and including 650° C, the oxidation of beryllium is protective: the rate of oxidation decreases continuously with time to reach a small value (e.g. 0.02 $\mu\text{g}/\text{cm}^2 \text{ h}$ at 500° C after 300 h).

2. The oxidation does not, in contrast to previous work, follow a parabolic rate law. The lack of conformity to a simple rate expression may be due to changes in the impurity content of the oxide layer as time proceeds.

3. At 750° C breakaway occurs, the rate first decreasing and then increasing with time.

4. The oxidation curves show small, sporadic discontinuities (approx. 1 $\mu\text{g}/\text{cm}^2$).

5. A combined electron microscopic and kinetic investigation would lead to a better understanding of the jerky oxidation (4) and the breakaway (3).

Acknowledgements

It is a pleasure to thank Dr. J. E. Antill for useful discussions and for supplying the beryllium specimens. We are also grateful to the U.K. Atomic Energy Authority for financial support.

References

- ¹⁾ E. A. Gulbransen and K. F. Andrew, J. Electrochem. Soc. **97** (1950) 384
- ²⁾ D. Cubicciotti, J. Amer. Chem. Soc. **72** (1950) 2084
- ³⁾ B. W. Mott and H. R. Haines, J. Inst. Metals **80** (1951-52) 629
- ⁴⁾ J. E. Antill, private communication
- ⁵⁾ E. A. Gulbransen, Rev. Sci. Inst. **15** (1944) 201
- ⁶⁾ D. W. Aylmore, S. J. Gregg and W. B. Jepson, J. Inst. Metals **88** (1959-60) 205
- ⁷⁾ I. S. Kerr and H. Wilman, J. Inst. Metals **84** (1955-56) 379
- ⁸⁾ N. Cabrera and N. F. Mott, Rep. Progress in Physics **12** (1948) 163
- ⁹⁾ C. Wagner, Z. Physik. Chem. B **21** (1933) 25
- ¹⁰⁾ V. D. Scott, Acta Cryst. **12** (1959) 136
- ¹¹⁾ H. H. Uhlig, Acta Met. **4** (1956) 541
- ¹²⁾ D. Caplan and M. Cohen, J. Metals **4** Trans. (1952) 1057
- ¹³⁾ R. F. Tylecote, J. Inst. Metals **81** (1953) 681
- ¹⁴⁾ D. A. Vermilyea, Acta Met. **5** (1957) 492
- ¹⁵⁾ N. B. Pilling and R. E. Bedworth, J. Inst. Metals **29** (1923) 529
- ¹⁶⁾ R. Takagi, J. Phys. Soc. Japan **12** (1957) 1212

LETTERS TO THE EDITORS · LETTRES AUX REDACTEURS

SINTERING OF HIGH DENSITY URANIUM DIOXIDE BODIES†

C. Y. ANG and E. W. BURKHAMMER

Corporate Research Labs., P. R. Mallory & Co., Inc., Indianapolis, Indiana, USA

Received 15 March 1960

1. Introduction

Because of its resistance to radiation damage and corrosion in high temperature pressurized water, UO_2 steadily gains recognition as an outstanding reactor fuel material. The efforts to obtain high density UO_2 bodies in recent years have been prompted by the evidence^{1,2)} that retention of fission-product gases is inversely proportional to the amount of residual porosity. Technically, UO_2 bodies with density greater than 93 % of the theoretical can be produced by powder metallurgy and other techniques such as extrusion, slip casting and swaging. However, the earlier procedures used to produce dense UO_2 bodies by the "cold press and sinter" technique, usually involved compacting pressure as high as 125 tsi¹⁾ and sintering temperature as high as 1750° C³⁾.

Recently there have been several approaches taken by different investigators to achieve the objective of lowering the sintering temperature. Glatter⁴⁾ has shown that a sintering temperature of 1600° C and a time of five hours could yield 94 % dense UO_2 pellets, provided the Natural Grade MCW (Mallinckrodt Chemical Works) powder was ballmilled 72 hours and the pellets were compacted at 80 tsi. Arenberg and Jahn⁵⁾ have demonstrated that a final sintering temperature of 1500° C was sufficiently high to achieve densification by utilizing the principles of creating lattice defects to promote diffusion.

Their techniques involved wet milling of the MCW UO_2 powder for 8 to 16 hours and stringent control of the variation of sintering atmospheres as a function of temperature. A sintering temperature as low as 1300° C has been reported by Langrod⁶⁾ to be adequate for the densification of UO_2 pellets. Langrod chose to prepare the non-stoichiometric oxide material by blending in proper proportions UO_2 and U_3O_8 powders. The sintering cycle was eight hours and the atmospheres used were wet nitrogen and hydrogen. The end product was actually $\text{UO}_{2.30}$.

Recent irradiation tests⁷⁾ indicated that the stoichiometric or near-stoichiometric (O/U ratio less than 2.15) UO_2 elements should be used for optimum performance, on the basis of cracking phenomenon and release of fission gases. These findings simply mean that if the technique used to densify UO_2 is by employing oxidizing atmospheres during sintering, the final temperature of the process must be above 1400° C in order to stabilize the oxide at the stoichiometric composition.

This report presents some recent experimental data on the sintering of high density UO_2 bodies from the as-received MCW powders. The experiments were conducted in the attempt to achieve 94 % density under the following conditions: (1) No further powder reprocessing except the addition of densification promoter and binder by blending; (2) compacting pressures not to

† This article is based on a paper presented before the Notre Dame conference on "Sintering and Related Phenomena" at the University of Notre Dame, June 15-17, 1959.

exceed 60 tsi; (3) sintering temperatures not to exceed 1600° C with sintering times as short as possible; (4) use of one type of sintering atmosphere throughout the normal densification cycle, and (5) the final product should be stoichiometric or very nearly stoichiometric in O/U ratio.

2. Materials

Initially two types of UO_2 powders, Ceramic Grade and High Fired, from Mallinckrodt Chemical Works, were used. Preliminary experimental results indicated that the sinterability of the High Fired powder was not as good as the Ceramic Grade material. Therefore, the experimental data presented in this report were obtained using the Ceramic Grade powder which had not been enriched and contained only about 0.7 wt % U-235. Since no attempt was made to alter the as-received powder characteristics, it suffices to mention here that the apparent powder density was about 1.5 g/cc and the Fisher average size of the spongy particles was in the neighborhood of one micron. The density of UO_2 is taken as 10.95 g/cc, but the theoretical densities of the experimental mixes varied somewhat, depending on the amount and type of additives used.

Three types of densification promoters were used. Preliminary results indicated that TiO_2 and CaO imparted higher compactibility and sinterability to UO_2 than did CaTiO_3 (calcium titanate). UO_2 pellets doped with TiO_2 which had the best thermal shock resistance were nevertheless quite sensitive to the dew point of the sintering atmosphere with respect to degree of densification.

Of the three types of binder or lubricant used in the preliminary studies, polyvinyl alcohol (Elvanol 51-05, DuPont) was selected for use in the subsequent investigation. The use of glyptol and calcium stearate resulted in compacts with poor green strength.

3. Procedures

Except for the precautionary measures taken to avoid health hazards, the techniques and

equipment used in this investigation were by no means unconventional. As indicated previously, the straight cold-press-and-sinter powder metallurgical technique was used. The procedures described below were established after some exploratory experimentation. The results of the exploratory or feasibility studies are not included in this report.

A mixture of 99.75 % UO_2 and 0.25 % TiO_2 or CaO was blended for one hour by tumbling in a glass jar. A water solution of polyvinyl alcohol (2 % of the weight of powder mix) was stirred into the blended powder. The water was then driven off by heating the powder at 110° C. The dried powder cakes were pulverized in a porcelain mortar.

Because of the abrasive nature of UO_2 powder, a carbide lined 1.3 cm ($\frac{1}{2}$ inch) diameter die was used for compacting. Various compacting pressures between 10 and 60 tsi were used in this investigation. Since a given amount of powder was maintained, the pressed heights of the samples varied between 0.6 cm ($\frac{1}{4}$ inch) to 1.3 cm ($\frac{1}{2}$ inch), depending on the pressed densities.

Dry dissociated ammonia gas was used as the sintering atmosphere. The sintering furnace used was a regular production type high temperature furnace with molybdenum heating elements. Although the furnace was designed for continuous operation, batch sintering was used in this investigation. The pressed compacts were loaded on either molybdenum or graphite boats lined with fine alundum sand. The experimental temperatures used were 1500 and 1600° C, with various sintering times up to 6 hours at temperature.

The sintered densities were obtained by the water displacement method. The etching procedure for the preparation of metallographic samples involved immersion for about 20 minutes in a solution of 1 H_2O - 1 HNO_3 - $\frac{1}{5}$ H_2SO_4 . The same samples were used in the X-ray diffraction study to determine the lattice parameter of the sintered oxide. All property data presented in this report are the average values of two or more samples.

TABLE 1
Experimental data on pressing and 1500° C sintering of ceramic grade UO₂
(PVA binder; TiO₂ flux; TD = 10.90 g/cc)

Compacting pressure (tsi)	Average pressed density (g/cc)	1500° C sintering					
		4 hours			6 hours		
		Sintered density (g/cc)	% Shrinkage		Sintered density (g/cc)	% Shrinkage	
			Dia.	Height		Dia.	Height
40	5.80	9.85	16.4	17.2	9.85	17.4	18.6
50	6.08	10.00	16.1	16.4	10.26	16.5	18.4
60	6.26	10.14	15.7	16.9	10.67	15.1	19.3

TABLE 2
Experimental data on pressing and 1600° C sintering of ceramic grade UO₂
(PVA binder; CaO † or TiO₂ flux)

Compacting pressure (tsi)	Average pressed density (g/cc)		3 hours sintering at 1600° C					
			With CaO flux			With TiO ₂ flux		
	With CaO	With TiO ₂	Sintered density (g/cc)	% Shrinkage		Sintered density (g/cc)	% Shrinkage	
				Dia.	Height		Dia.	Height
10	5.10		9.97					
20	5.55		9.99					
30	5.78		10.02					
40	6.08	5.80	10.27	14.9	17.9	10.48	16.3	20.1
45	6.20		10.31					
50	6.26	6.08	10.36	14.9	18.5	10.48	15.4	19.4
55	6.32		10.37					
60	6.41	6.26	10.43	13.9	18.0	10.48	14.7	18.5

† With CaO, TD = 10.88 g/cc.

4. Results and Discussion

The density and shrinkage data are presented in tables 1 and 2. The use of CaTiO₃ as a densification promoter did not produce satisfactory results; consequently, the data on samples containing this agent are not included in this report.

It is obvious from the results of this investigation that under given sintering conditions, the degree of densification of UO₂ is a function of pressed density. However, to achieve 94 % density or higher the experimental data show that it is not necessary to use compacting pressures greater than 60 tsi. The densification behaviour of pressed UO₂ pellets is more clearly

depicted in figs. 1 and 2, in which sintered density values obtained under different sintering conditions are plotted in terms of percent theoretical density as a function of degree of compaction (pressed density as % theoretical). Fig. 1 shows that the TiO₂-containing pellets can be sintered to over 94 % dense at 1500° C in 6 hours, provided the pressed density is at least 55.8 % (6.08 g/cc) of the theoretical. In fig. 2, the advantage of using TiO₂ as the densification promoter is shown by the upper curve which indicates that pellets pressed at 40 tsi (pressed density = 53.2 % of the theoretical) can be sintered to over 96 % dense at 1600° C in 3 hours. Under similar conditions

the CaO-containing pellets can only attain 94.4% density, although the pressed density may be higher than TiO_2 -containing pellets at a given compacting pressure.

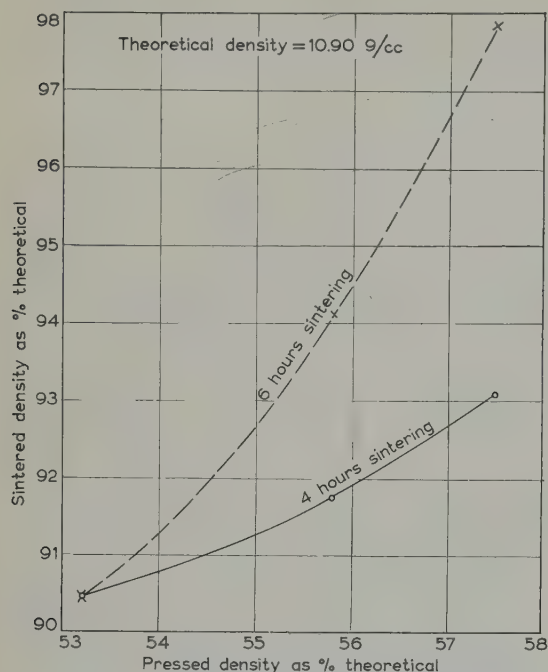


Fig. 1. 1500°C sintering of UO_2 with TiO_2 flux.

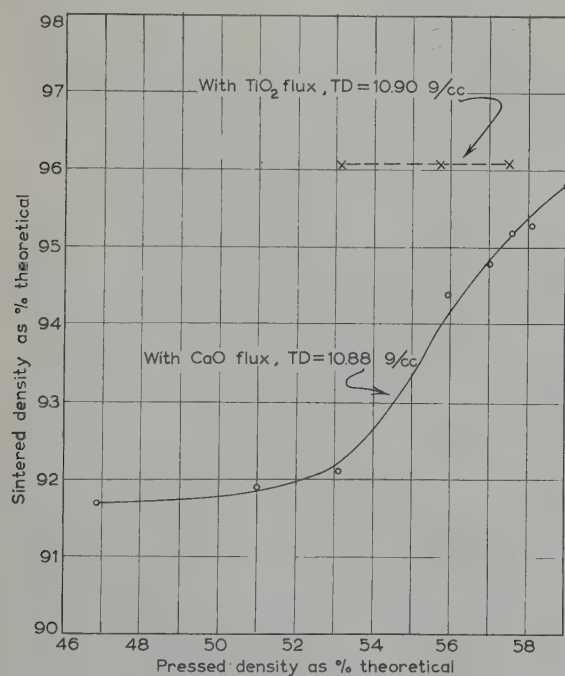


Fig. 2. 3 hours sintering of UO_2 at 1600°C .

It is possible that the principles of creating lattice defects through the variation of ratios of oxygen to uranium might have played a part in facilitating densification. On the other hand, it is not likely that the mechanism of creating lattice defects in this instance was operating in the same manner as that disclosed by Arenberg and Jahn⁵⁾. It can be shown theoretically⁸⁾ TiO_2 may be reduced by dry dissociated ammonia or hydrogen at temperatures above 1400°C . In practice a partial reduction might occur under these conditions, and the resultant H_2O from the reaction could possibly cause the temporary oxidation of UO_2 to a non-stoichiometric oxide, thus creating lattice defects. The fluctuant crossing of the metal-metal oxide equilibria lines could conceivably promote densification.

Using low compacting pressures will minimize pressure cracking of compacts and reduce tool wear and breakage. But, an important drawback of maintaining a low pressed density is the occurrence of high shrinkage upon densification. While it is true that dimensions can still be controlled if high shrinkage is uniform, the thickness of the pressed parts in the direction of pressing must necessarily be limited. The results of this investigation show that linear shrinkages as high as 20% have been encountered.

The microstructure of a dense UO_2 pellet is shown in fig. 3 at 330 magnification. This

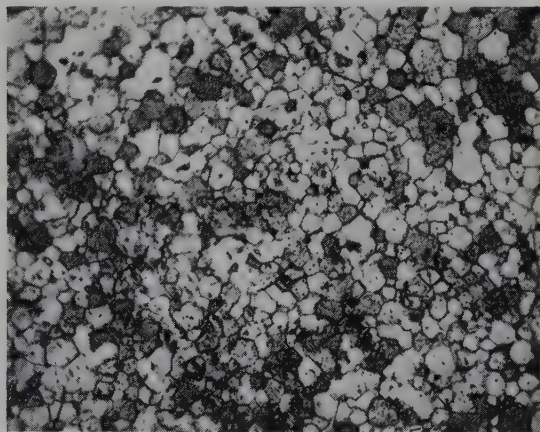


Fig. 3. Microstructure of a dense UO_2 pellet containing 0.25% TiO_2 . $\times 330$.

sample had been sintered 6 hours at 1600° C to almost 98 % density, therefore the residual porosity is very low. By X-ray diffraction the lattice parameter of the sintered material was found to be 5.47 Å, indicating that the oxide is very nearly stoichiometric in composition with O/U ratio between 2.00 and 2.03⁹).

5. Conclusions

It has been found after a limited investigation that the as-received Ceramic Grade UO₂ powder from Mallinckrodt Chemical Works could be processed by conventional powder metallurgical means into dense pellets. The as-received raw material does not have to be subjected to special treatments other than blending with small amounts of polyvinyl alcohol as a binder and TiO₂ or CaO as a densification promoter.

The pellets may be compacted at pressures of 60 tsi or lower and sintered to higher than 94 % density in a dry dissociated ammonia atmosphere. Depending on the degree of compaction, the sintering conditions required to achieve high density may involve temperatures of 1500 to 1600° C with times at heat of 3 to 6 hours. Using this process the sintered UO₂ will be very nearly stoichiometric in composition which is desirable for fuel element application. With the processing conditions and equipment used in this investigation, the chances of economically producing large quantities of UO₂ are good.

The phenomenon of rapid densification of samples containing TiO₂ under the experimental conditions suggested the possibility of creation of lattice defects through the variation

of O/U ratio during the sintering cycle. It was pointed out that TiO₂ might have been partially reduced by the sintering atmosphere under favorable conditions, releasing H₂O as an oxidizing agent which upset the metal-metal oxide equilibrium and promoted densification.

Acknowledgement

Thanks are due R. Emmert for his experimental effort which produced data for this paper, and F. Sauer and L. Gerlach for their assistance in metallography and X-ray diffraction. The authors are also indebted to H. Sigurdson, C. H. Moore and F. R. Hensel for reviewing the manuscript and offering valuable suggestions.

References

- 1) C. M. Henderson *et al.*, Nuclear Metallurgy **4** (AIME, 1957)
- 2) J. C. Danko, Nucleonics **16** (1958) 90
- 3) D. R. Stenquist, J. American Ceramic Society **41** (1958) 273
- 4) J. Glatter, Nuclear Metallurgy **4** (AIME, 1957)
- 5) C. A. Arenberg *et al.*, J. American Ceramic Society **41** (1958) 179
- 6) K. Langrod, Low Temperature Method of Sintering Uranium Oxide Pellets, presented before the 61st Annual Meeting of the American Ceramic Society, April 1959, Chicago
- 7) O. J. C. Runnalls, Nucleonics **17** (1959) 104
- 8) C. Y. Ang, E. Burkhammer and J. C. Kenny, Thermochemical Considerations of Metal-Metal Oxide Equilibria in Powder Metallurgy, to be published
- 9) W. B. Pearson, A Handbook of Lattice Spacings and Structures of Metals and Alloys (Pergamon Press, 1958) pp. 1011 and 1031

ASPECTS FRACTOGRAPHIQUES DU BIOXYDE D'URANIUM FRITTÉ

A. PORTNOFF—PORNEUF

Service de Chimie des Solides, Centre d'Etudes Nucléaires de Saclay, Gif-sur-Yvette (S & O) France

Reçu le 14 avril 1960

La présente lettre décrit les aspects microscopiques des fractures de bioxyde d'uranium, ainsi que leurs relations avec les conditions de préparation de ce produit et les traitements thermiques qu'il a subis ¹⁾.

Nous avons pratiqué les fractures à 25° C par impact et nous avons observé leurs aspects au microscope électronique en utilisant une méthode de double réplique rhodoïd-carbone avec ombrage ²⁾.

Un aspect caractéristique d'une telle fracture est représenté par la figure 1, sur laquelle on remarque :

des porosités;

des surfaces présentant des figures de rivières
telles que les régions notées A sur la figure 1;

des surfaces unies telles que la région notée B.

La figure 2 présente un autre aspect des fractures où on reconnaît des figures de rivières dans la zone A, ainsi qu'un faciès d'aspect nouveau dans la zone C.

On sait que les figures de rivières sont associées à une rupture par clivage ³⁾. C'est donc ce mode de fracture qui a prévalu dans les régions que nous avons notées A. Les figures 3 et 4 illustrent avec plus de détails ce phénomène.

L'aspect des joints de grains de la région notée C est caractéristique d'une surface polycristalline ayant évolué vers l'équilibre des joints de grains qui a conduit au gravage de ceux-ci que l'on peut noter sur la figure.

Il en résulte que les surfaces telles que C

correspondent à des cavités internes du matériau fracturé (figure 5).

Les zones telles que B, qui ne présentent aucune des caractéristiques précisées ci-dessus, peuvent très vraisemblablement être attribuées à une décohésion inter-granulaire. C'est ce que nous avons admis dans la suite de notre travail.

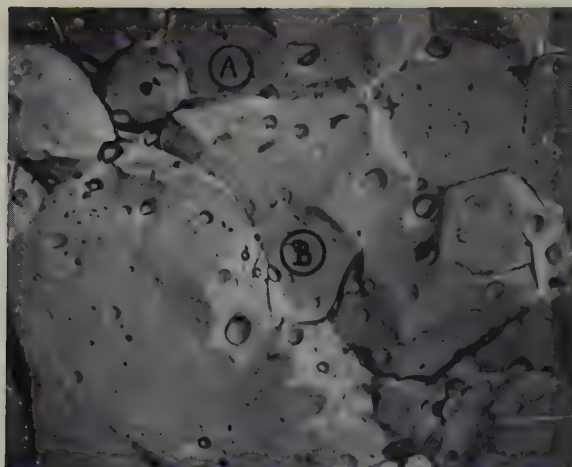
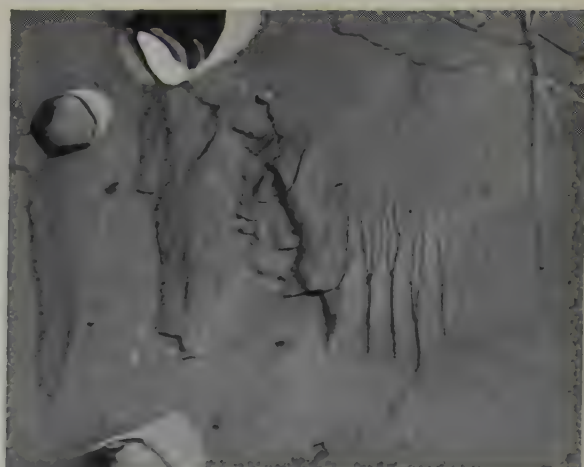
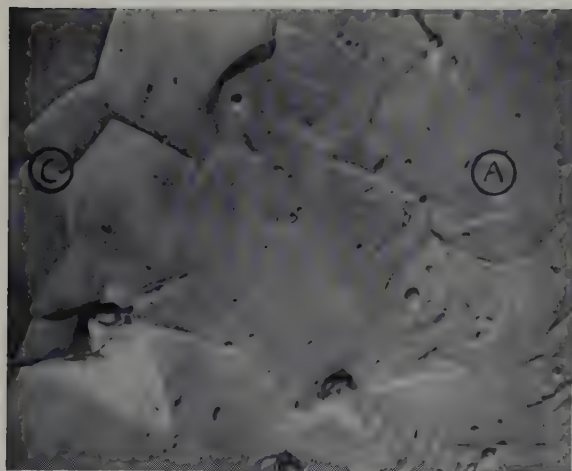
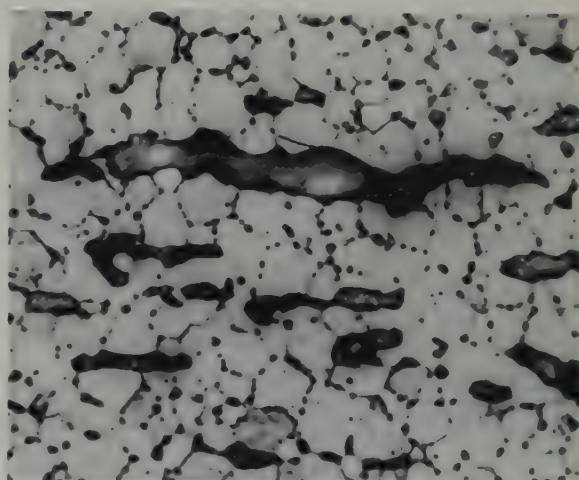
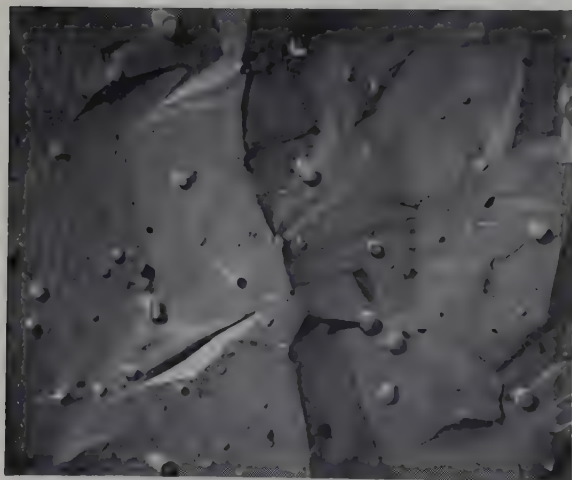
La fractographie conduit à des ruptures le long des surfaces de moindre résistance et favorise, de ce fait, la mise en évidence de surfaces internes du matériau fracturé. En particulier, elle nous a permis l'observation détaillée de cavités présentes dans le bioxyde d'uranium fritté.

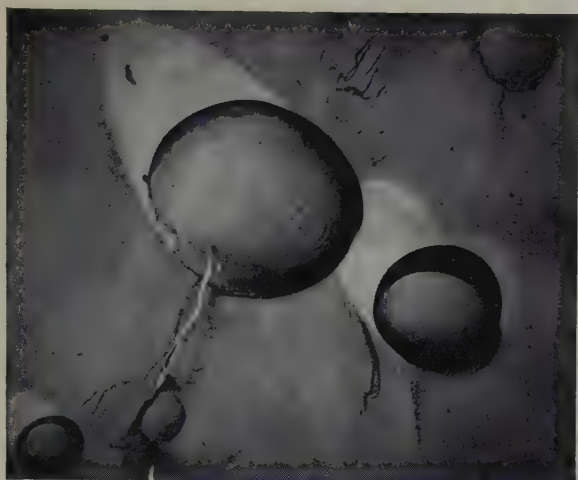
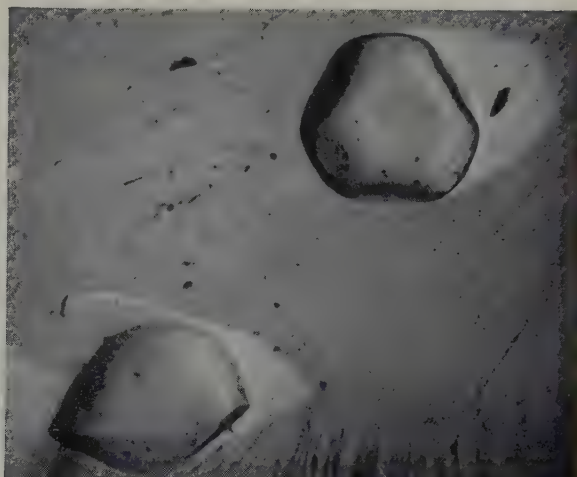
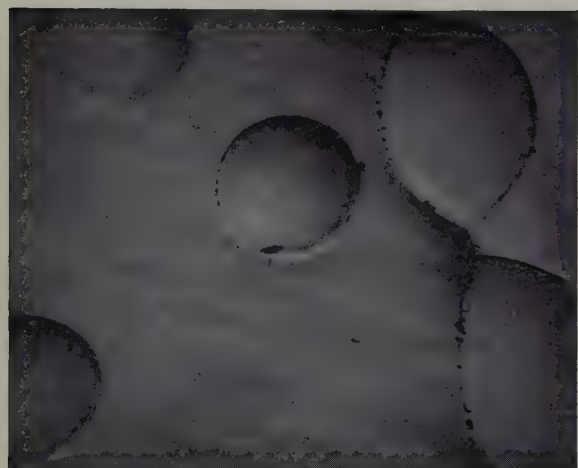
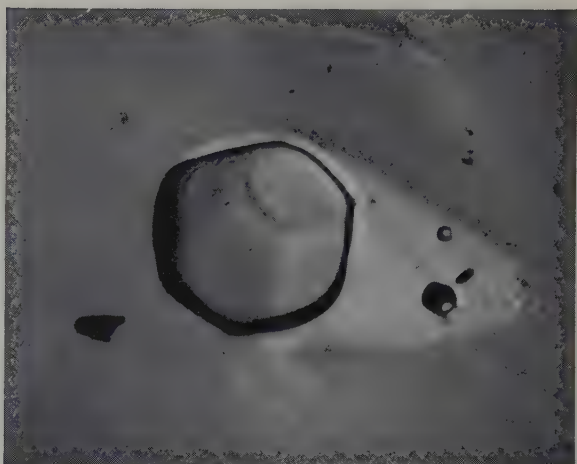
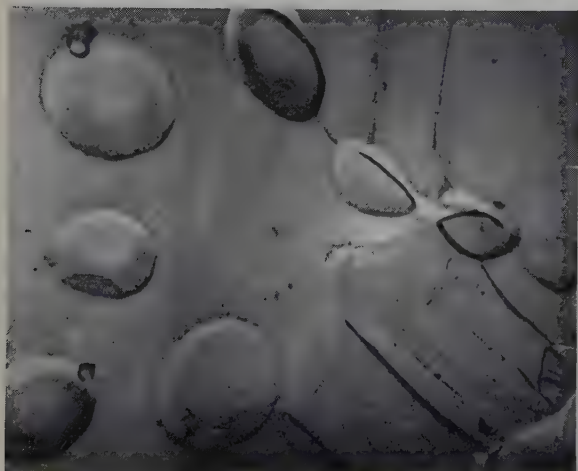
Pour la commodité de l'exposé, nous diviserons ces cavités en micropores, comme ceux visibles sur la figure 1, et macropores, comme la cavité qui était limitée par la partie notée C sur la figure 2.

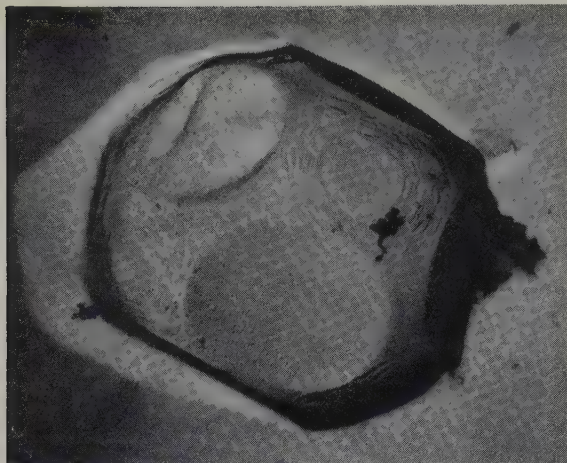
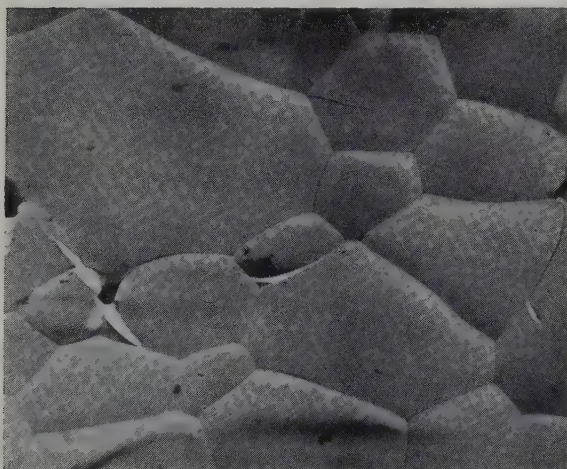
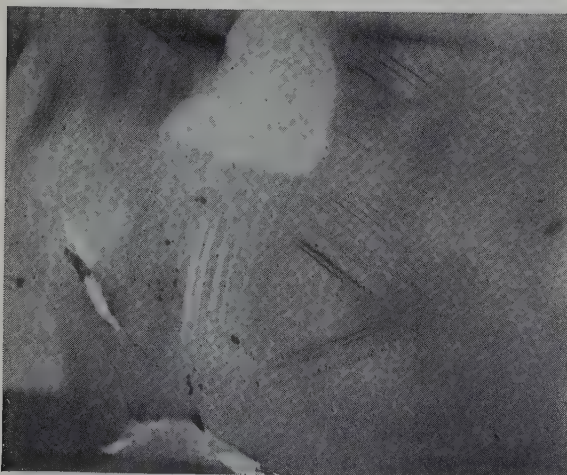
La figure 6 représente, dans leurs détails, des micropores existant dans un bioxyde d'uranium fritté à une température minimum de 1500° C. Ces micropores apparaissent sous une forme pseudo-sphérique présentant des figures polaires et des surfaces planes faiblement accusées.

Les pores visibles sur la figure 7 sont situés à l'intérieur du grain. Des pores peuvent également être situés sur une surface inter-granulaire, comme sur la figure 8, où l'on distingue des pores de forme ovoïde le long du joint de grain.

Ces pores présentent également des facettes planes et des figures polaires analogues à celles constatées sur les pores intra-granulaires.

Fig. 1. $\times 3000$.Fig. 4. $\times 10\,000$.Fig. 2. $\times 3000$.Fig. 5. $\times 500$.Fig. 3. $\times 3000$.Fig. 6. $\times 15\,000$.

Fig. 7. $\times 15\,000$.Fig. 10. $1800^{\circ}\text{C.} \times 15\,000$.Fig. 8. $\times 15\,000$.Fig. 11. $1800^{\circ}\text{C.} \times 15\,000$.Fig. 9. $1600^{\circ}\text{C.} \times 15\,000$.Fig. 12. $2000^{\circ}\text{C.} \times 15\,000$.

Fig. 13. 2000° C. $\times 15\,000$.Fig. 14. $\times 3000$.Fig. 15. $\times 15\,000$.

Les figures polaires et les facettes apparaissant sur les micropores sont plus ou moins nettes suivant la température de frittage. Pour préciser la relation entre la température à laquelle le matériau a été porté et l'aspect des micropores, nous avons recuit, pendant une même durée de 5 heures, des éprouvettes préalablement frittées à basse température⁴).

Un chauffage à 1600° C conduit à l'aspect représenté par la figure 9. A 1800° C, on obtient l'aspect illustré par les figures 10 et 11. Enfin, à 2000° C, on a des aspects semblables, tels que ceux des figures 12 et 13.

On remarque qu'au fur et à mesure que la température du recuit s'élève apparaissent d'abord les faces de l'octaèdre puis, toujours avec un développement moindre, celles du cube. Il est possible que dans certains cas apparaissent également, avec un faible développement, les faces du dodécaèdre.

Les macropores présentent un aspect illustré par la figure 14 où l'on remarque la formation de figures polaires analogues à celles constatées sur les micropores.

La surface des macropores présente aussi, quelquefois, des faciès tel que celui de la figure 15, où on voit un système de stries à symétrie ternaire développé sur la surface libre du grain.

La symétrie des facettes planes sur les micropores, ainsi que l'analogie avec ces dernières des figures de stries sur les surfaces des macropores, montre que leur formation est liée à la symétrie cristalline du bioxyde d'uranium. Elle est due à l'évolution de la surface, initialement courbe, des porosités vers une surface polyédrique limitée par des plans cristallins de faible énergie.

EN CONCLUSION

L'identification du mode de rupture qui caractérise les zones de faible résistance du bioxyde d'uranium, c'est-à-dire les zones riches en pores, permet de distinguer entre un bioxyde d'uranium fritté de porosité intergranulaire, et un bioxyde d'uranium fritté de porosité intra-granulaire.

Nous avons montré la corrélation existant

entre la température à laquelle le fritté a été porté et l'aspect des porosités qu'il contient.

Nous remercions Monsieur Bogdanovitch de sa collaboration pour la préparation des répliques et les photos au microscope électronique.

Bibliographie

- 1) A. Portnoff-Porneuf, Thèse, Paris, 1960
- 2) N. Azam, Réunion Uranium, Compte Rendu CEA no. 7 (juin 1956)
- 3) J. J. Gilman, Trans. AIME 212 (1958) 310
- 4) A. Bel, B. François, R. Delmas et R. Caillat, Comptes Rendus 249 (1959) 1045

CLIVAGE DU BIOXYDE D'URANIUM

A. PORTNOFF—PORNEUF

Service de Chimie des Solides, Centre d'Etudes Nucléaires de Saclay, Gif-sur-Yvette (S & O), France

Reçu le 14 avril 1960

L'échec des essais du clivage de l'oxyde d'uranium sur des monocristaux de grande taille¹⁾ nous a conduit à entreprendre l'étude de ce clivage sur des cristaux de plus petite taille, mais moins imparfaits, préparés dans l'état solide par grossissement des grains d'un fritté de bioxyde d'uranium.

Pour préparer nos échantillons, nous avons chauffé à 2200°C sous hydrogène, pendant 2 heures, des pastilles de bioxyde d'uranium obtenues elles-mêmes par frittage à 1350°C d'une poudre de bioxyde d'uranium de grande surface spécifique.

Ce traitement nous a conduit à des pastilles extrêmement fragiles que l'on peut briser par simple pression des doigts. Par ce moyen, on obtient des particules monocristallines de tailles généralement comprises entre 0,05 mm et 1 mm (fig. 1).

Comme on le voit, ces éclats présentent un système de faces planes le long desquelles se produit la décohésion de la pastille. L'examen (fig. 2), d'une telle surface montre l'aspect caractéristique en gradins d'une face de clivage.

Le présent travail nous a permis d'établir, par l'étude micrographique et radio-cristallographique, les caractéristiques du clivage obtenu.

La figure 3 montre trois directions différentes de gradins que nous avons notées 1, 2 et 3. On voit que les angles entre ces directions sont, aux erreurs d'expérience près, de 60°.

L'étude détaillée des portions de grains d'aspect curviligne permet de décomposer ceux-

ci en une suite d'éléments chacun parallèle à l'une des directions 1, 2, 3.

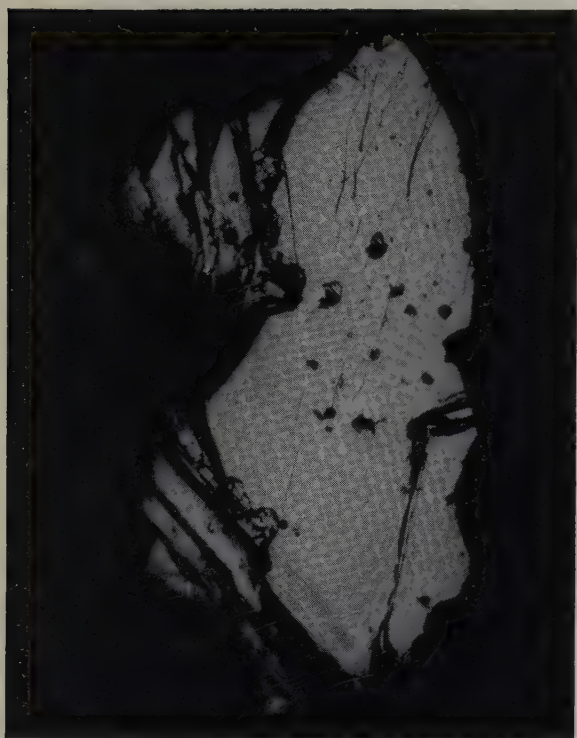
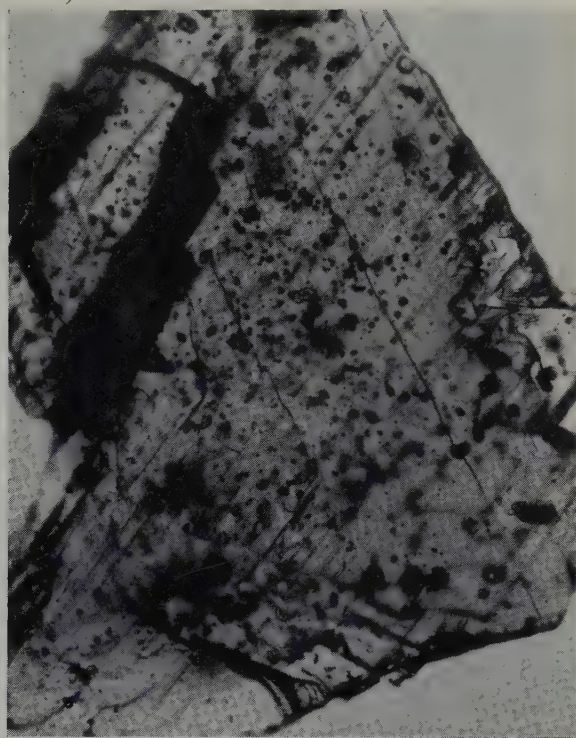
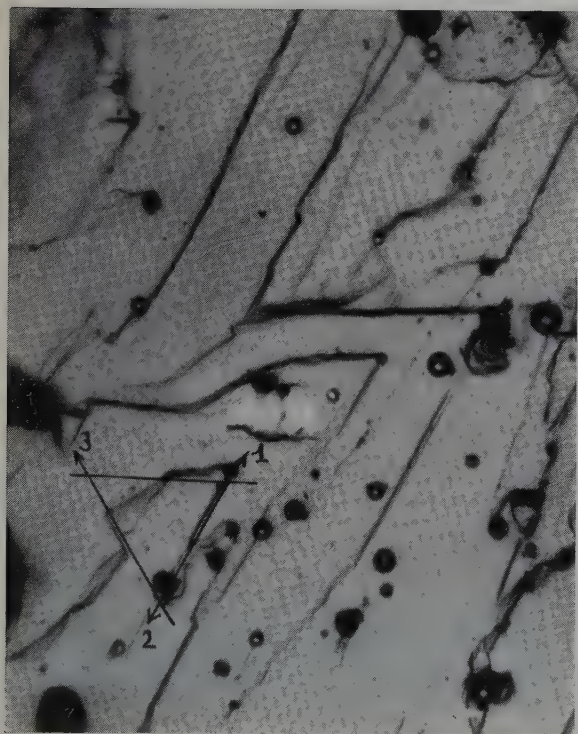
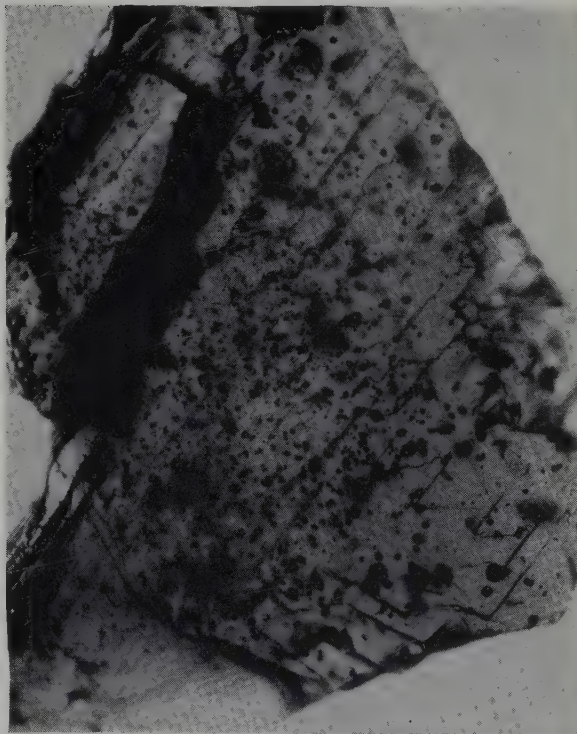
Cette caractéristique des gradins montre que le plan de clivage est perpendiculaire à un axe de symétrie ternaire du réseau cristallin du bioxyde d'uranium, ce qui établit que le plan de clivage est le plan (111).

Nous avons recoupé ce résultat en mesurant l'angle des dièdres formé par les différents systèmes de plans de clivage. Nous avons trouvé des angles de 70-71° qui, étant donné les difficultés de mesure sur les petits cristaux dont nous disposions, concordent d'une manière satisfaisante avec la valeur de 70° 32', angle de familles distinctes des plans (111) dans le système cubique.

Pour nous assurer que les gradins observés n'étaient pas dûs à la formation de bandes de glissement sur les cristaux de bioxyde d'uranium, nous avons comparé la topographie de la face inférieure (fig. 3) et de la face supérieure (fig. 4) d'un cristal mince. On constate que le dessin des gradins est très différent sur l'une et l'autre de ces faces, ce qui exclut la possibilité de glissement.

Les expériences décrites jusqu'ici établissent que l'oxyde d'uranium se clive le long des plans (111).

De manière à contrôler ce résultat, nous avons fait des diagrammes de Laue sur les faces de clivage de certains de nos échantillons en orientant le faisceau incident perpendiculairement à la face étudiée.

Fig. 1. $\times 125$.Fig. 3. $\times 400$.Fig. 2. $\times 800$.Fig. 4. $\times 400$.

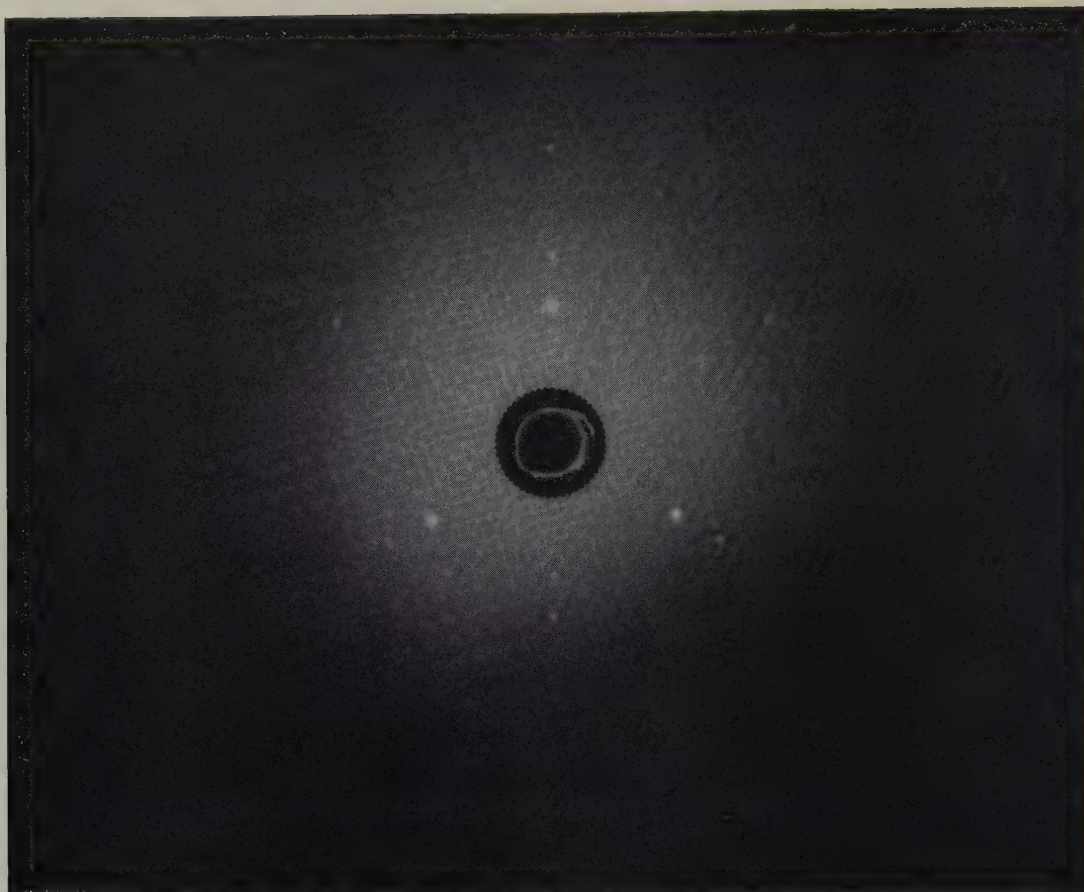


Fig. 5

Nous avons obtenu des diagrammes tels que celui représenté par la figure 5 et la détermination des zones $[10\bar{1}]$ sur le diagramme de rayons X nous a montré que chacune est perpendiculaire à l'un des systèmes de gradins du cristal irradié. Il en résulte que les directions des gradins sont les directions $[10\bar{1}]$. Or, celles-ci sont celles des intersections des plans de la famille (111).

La radiocristallographie confirme donc les résultats de la micrographie et nous permet

d'affirmer, en toute certitude, que le bioxyde d'uranium se clive parallèlement au plan (111) et uniquement suivant cette famille de plans.

Je remercie Madame Belbéoch et Monsieur Péro pour l'aide qu'ils m'ont apportée dans l'étude radiocristallographique.

Bibliographie

- 1) W. B. Campbell, V. J. Hurst et W. E. Moody, J. Am. Ceram. Soc. 42 (1959) 262

GROWTH HABIT OF ELECTRODEPOSITED URANIUM DIOXIDE
SINGLE CRYSTALS

R. G. ROBINS

UKAEA, Metallurgy Division, Atomic Energy Research Establishment, Harwell, Didcot, Berks., UK

Received 14 April 1960

An octahedral growth habit has been observed in crystals of uranium dioxide formed by vapour deposition^{1,2)} and in crystals grown from fused salts¹⁾. A cubic growth habit was observed when vapour was condensed on ionic substrates²⁾. Naturally occurring uraninite is commonly cubic, octahedral, or cubo-octahedral, sometimes modified by {520}, {114} or {335} forms³⁾.



Fig. 1. Single crystals of uranium dioxide as formed on platinum cathode ($\times 7$).

Separate single-crystals of uranium dioxide were deposited by the Author on a platinum cathode (see fig. 1) by the electrolysis of a solution of uranyl chloride in fused sodium chloride-potassium chloride eutectic at 840° C under reducing conditions (to be reported later). These crystals were grown to a size of 3 mm across, and a mass of about 50 mg. The orientation of the crystals on the platinum cathode was random both in the case of fine grained and single crystal cathodes.

The crystal habit was determined by goniometric and X-ray diffraction measurements and found to be octahedral. The $\{111\}$ faces were modified by $\{100\}$ faces developing at a crystal

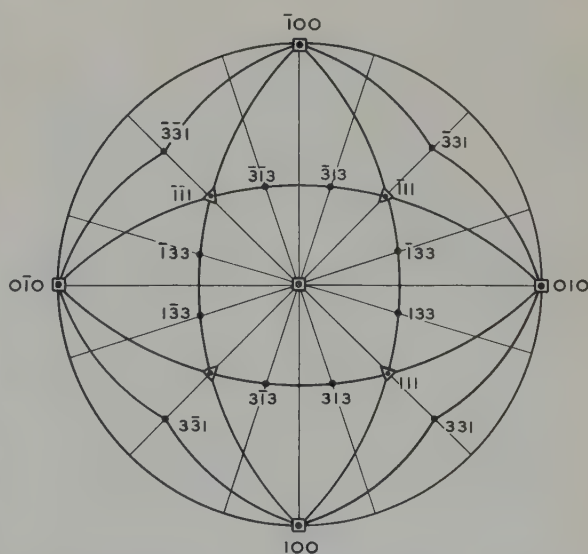


Fig. 2. Stereogram of electrolytically deposited uranium dioxide crystal.

mass of about 5 mg, and further modified by {331} faces at a crystal mass of about 10 mg. The {331} facets developed in pairs between the {111} faces of the cubo-octahedra (see fig. 2).

Variation of oxygen content up to $\text{UO}_{2.15}$ by atmosphere control did not influence the {111}, {100}, {331} habit.

Cleavage of the crystals occurred on {111} planes, and interpenetrant twins on {111} were occasionally observed. The {111} cleavage of fused uranium dioxide has previously been reported ⁴).

References

- ¹) R. J. Bard, Los Alamos (USA) Report No. LA-2076 (March 1957)
- ²) J. T. Waber, J. A. O'Rourke and R. Kleinberg, *J. Electrochem. Soc.* **106** (1959) 96
- ³) C. Frondel, *Systematic Mineralogy of Uranium and Thorium*, Geol. Surv. Bull. 1064 (US Govt Printing Off, 1958) 31
- ⁴) R. G. Robins, and P. J. Baldock, *J. Amer. Ceram. Soc.* **43** (1960) 228

α - β THERMAL CYCLING OF URANIUM

W. S. BLACKBURN

C. A. Parsons & Co. Ltd., Nuclear Research Centre, Fossway, Newcastle-upon-Tyne 6, UK

Received 17 May 1960

It has been suggested^{1,2)} that when uranium is thermally cycled into and out of the β phase, there is a contraction along the normal to the phase boundary and identical extensions in the perpendicular directions. The idea was applied to the case of a long hollow tube of inner and outer radii a and b in which the phase boundary moves radially in a symmetric manner. Further consequences of this assumption are deduced below.

We may write the radial displacement at a distance r from the axis as $f(r)$. Then the radial strain is df/dr and the hoop strain f/r . Since the motion of the phase boundary is radial, we expect equal axial and hoop strains and hence since the net deformation after a complete cycle gives rise to no change in volume ($2f/r + df/dr$) is zero. Thus we find $f = c/r^2$ where c is a constant which will in general depend on the manner of cycling. Its magnitude may be estimated if the axial strain on the outer surface, ϵ^* , or the mean axial strain ϵ is known, since

$$\epsilon^* = c/b^3, \quad \epsilon = 2c/\{ab(a+b)\}.$$

Hence the radial displacements on the inner and outer surfaces are

$$\frac{c}{a^2} = \frac{\epsilon^* b^3}{a^2} = \frac{\epsilon b(a+b)}{2a} \quad \text{and} \quad \frac{c}{b^2} = \epsilon^* b = \frac{\epsilon(a+b)a}{2b}$$

respectively. If a is small the displacement on the outer surface is small and on the inner surface large.

We note however, that if the inner radius is

too small, the deformation is inadmissible since it implies more than one point going to an identical location. Thus we require

$$R + c/R^2 > r + c/r^2 \quad \text{if } R > r > a.$$

Hence the critical condition is

$$R^3 r^2 - c R^2 - r^3 R^2 + c r^2 = 0 \quad \text{for } R > r > a.$$

This equation has roots

$$R = r, \quad \{c \pm (4cr^3 + c^2)^{\frac{1}{2}}\}/(2r^2).$$

The condition that the greatest root is r is that

$$r \geq \{c + (4cr^3 + c^2)^{\frac{1}{2}}\}/(2r^2), \quad \text{i.e.}$$

$$(2r^3 - c)^2 \geq 4r^3 c + c^2, \quad \text{i.e. } r^3 \geq 2c.$$

Thus we require

$$r^3 \geq 2c \quad \text{for } r > a, \quad \text{i.e. } a^3 \geq 2c.$$

If this criterion is not satisfied, the deformation will be restricted. We may expect also that a certain amount of restriction will apply except when $a^3/2c$ is large. Thus a , if very small, will increase with successive cycles and hence may allow much greater deformation to occur in subsequent cycles. For large a however, the changes in radii are negligible and hence equal amounts of damage should occur in each cycle.

References

- 1) S. N. Buckley, A. G. Harding and M. B. Waldron, *J. Inst. Met.* **87** (1959) 150
- 2) J. J. Stobo, *J. Nuc. Mat.* **2** (1960) 97

LE FRITTAGE DES OXYDES D'URANIUM

A. BEL, R. DELMAS et B. FRANÇOIS

*Centre d'Etudes Nucléaires de Saclay, Gif-sur-Yvette (S. et. O) France, Département du Plutonium et
Département de Métallurgie*

(Réponse à la lettre de J. Williams, J. Mat. Nucl. 2 (1960) 92)

1) Les conditions opératoires des expériences de frittage en atmosphère d'argon d'oxyde d'uranium non stoechiométrique ont été les suivantes:

Les pastilles comprimées sont placées sur des supports en molybdène.

L'expérience acquise lors de la fabrication d' UO_2 fritté pour la première charge de combustible de Zoé, en 1948, nous a montré que le contact d' UO_2 avec les réfractaires alumineux ou silico-alumineux introduisait une pollution considérable et nous avons abandonné ce type de support.

Le cycle de température est tel que l'élimination de la majorité des liants a lieu lors d'un maintien de deux heures à 400°C dans l'argon, qui précède le frittage lui-même.

En tout état de cause, quels que soient les soupçons que l'on peut avoir sur l'influence du molybdène ou de traces de produits organiques sur la consommation d'oxygène excédentaire, les dosages chimiques montrent que les oxydes frittés dans l'argon à partir de poudres hyperstoechiométriques sont eux-mêmes hyperstoechiométriques. Par exemple: lors d'un frittage à 1200°C d'une poudre de composition $\text{UO}_{2,21}$, la densité obtenue était 10,5 et la composition moyenne $\text{UO}_{2,17}$.

2) Pour répondre à la question concernant les teneurs en eau des atmosphères de frittage, l'hydrogène est purifié sur des copeaux de Ti-Zr maintenus à 800°C , et l'ammoniac craqué sur une colonne de perchlorate de Mg. Dans les deux cas, les teneurs en eau sont inférieures à 10^{-3} mg/litre à l'entrée du four.

Il n'en est pas de même, par contre, dans la zone où se trouvent les produits en cours de frittage, où l'eau produite par la réduction de l'oxyde hyperstoechiométrique en $\text{UO}_{2,00}$ modifie vraisemblablement beaucoup cette valeur.

De plus, il faut souligner que la connaissance des teneurs en humidité du gaz ne renseignerait pas pour autant sur l'influence de l'eau apparue dans le produit lui-même lors de sa réduction par l'hydrogène. Par ailleurs, les premiers résultats d'une étude en cours indiquent que l'eau peut être retenue sur l'oxyde d'uranium jusqu'à des températures voisines de la température de début du frittage.

Le tableau présenté par M. J. Williams nous semble devoir être modifié: si l'on utilise comme densité théorique la valeur 10,9, les diminutions de porosité comparées sont en bon accord sauf pour le premier échantillon, qui accuse 95,1 % de diminution au lieu de 92,9 %.

3) Le phénomène de surfrittage dans le cas de l'oxyde d'uranium a été signalé, en effet, par Murray en 1950.

Cependant, l'influence de la surface spécifique de la poudre étudiée sur la valeur de la température optimum de frittage, que nous avons mise en évidence, nous paraît constituer un résultat expérimental nouveau.

En conclusion, le travail expérimental discuté montre que l'argon ou l'hydrogène utilisés comme atmosphères de frittage pour l'oxyde d'uranium permettent l'obtention de résultats technologiques analogues, la différence essentielle entre les deux cas nous paraissant résider dans les cinétiques de recristallisation.

Par ailleurs, nous ne disposons pas de résultats permettant de confirmer l'influence mise en évidence par les chercheurs britanniques d'un très faible écart à la stoechiométrie sur l'aptitude au frittage en atmosphère neutre. Toutefois, Melle. Carteret présentera à Amsterdam (3ème congrès international sur la réactivité

des solides, juin 1960) ses résultats sur l'influence de l'écart à la stoechiométrie des poudres d'oxyde d'uranium sur leur réactivité. Ce travail nous semble apporter des indications de nature à permettre une synthèse de nos deux points de vue.

OXIDATION OF URANIUM DIOXIDE IN AIR AT 350-1000° C

K. A. PEAKALL and J. E. ANTILL

Metallurgy Division, UKAEA Atomic Energy Research Establishment, Harwell, Didcot, Berks., UK

Received 30 May 1960

Uranium dioxide is an important fuel material in reactors but oxidises to U_3O_8 in air at elevated temperatures. The kinetics of the reaction of dense compacts is important in the handling and use of the fuel and has therefore been investigated over the range 350-1000° C.

Stoichiometric uranium dioxide pellets (0.98 cm diameter \times 0.89 cm long) with a density of approximately 10.5 g/cc were prepared by firing cold pressed powder compacts in argon at 1450° C followed by firing in a hydrogen-nitrogen mixture at 1400° C. Their oxidation behaviour was determined at 50° C intervals in the range 350-1000° C, using a conventional thermal balance. A pellet contained in an alumina crucible was brought to temperature in pure argon and then oxidised in air at a flowrate of 500 std. cc/min; the weight gain was recorded at suitable intervals until about 30 % of the theoretical weight gain for complete oxidation to U_3O_8 was observed. At 900 and 1000° C the reaction was carried to completion.

Typical weight gain vs. time curves are shown in fig. 1. At 350-600° C an induction period was observed which decreased as the temperature was raised; subsequent oxidation proceeded rapidly at a linear rate, the U_3O_8 falling away as a fine powder. At 650-850° C the product appeared to become protective but breakaway to a linear rate followed after a time which increased as the temperature was raised. Above 900° C the product formed a protective shell round the specimen and no breakaway phenomena were obtained during complete oxidation of the pellet although breakaway was obtained upon thermal cycling. The phase U_3O_8 can be deficient in oxygen above 600° C and as the

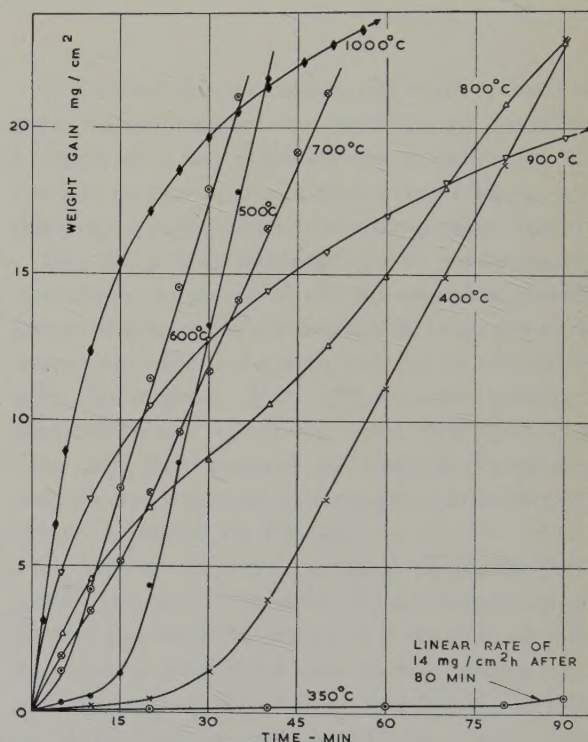


Fig. 1. Weight gain vs. time curves for 30 % oxidation of UO_2 pellets to U_3O_8 in air at 350-1000° C.

phase diagram is in doubt at high temperatures experiments were done to determine the composition of the final product at 1000° C; it was found to be $\text{UO}_{2.65}$.

One experiment was carried out at 400° C to determine whether the induction period was affected by the surface condition of the specimen after fabrication. 0.025 cm was ground off the surface of a pellet which was then oxidised as before. No detectable change occurred in the induction period or oxidation rate.

The interpretation of the results is complica-

ated by the fact that the phase diagram for the relevant composition range is in doubt and the oxides of uranium may be non-stoichiometric with UO_2 containing excess oxygen, and U_3O_8 less than the stoichiometric amount of oxygen. However, the induction period obtained at temperatures up to 600° C is consistent with the work of Aronson *et al.*¹⁾ who postulated that the nucleation of U_3O_8 could be rate-determining at 350° C; the transition from the slow to final fast rate might therefore be governed by a nucleation and growth mechanism.

The rate after the induction period is probably controlled by diffusion of oxygen ions through a thin uncracked layer of U_3O_8 , whose average thickness is constant at any particular temperature and which cracks once the stresses at the interface between the oxide phases are sufficiently great. However, at the higher temperatures (900–1000° C), when a thick scale is formed, diffusion of molecular oxygen through the outer porous part of the scale to the thin uncracked layer may be rate-determining. Table 1 shows that the final rate after 30 %

of the theoretical amount of oxygen had reacted decreases as the temperature rises from 500 to 900° C. This is thought to be due to an increase in the thickness of product through which the oxygen had to diffuse as the particle size of the product increased with temperature above 500° C. The mechanism of such thickening is probably associated with an increase in the plasticity of the product which allows the stresses in the film to be relieved by deformation rather than cracking. Sintering of the cracked product is unlikely to have been of importance as the density of the scale formed at 900° C was 7.6 g/cc (92 % of the theoretical value) whilst U_3O_8 powder does not sinter appreciably at 1000° C.

The reaction is further complicated by the diffusion of oxygen ions into the body of the pellet to form non-stoichiometric UO_2 . The process may facilitate the thickening of the uncracked film of U_3O_8 as it will decrease the rate of growth and hence allow more time for deformation. In addition it may well be responsible for the breakaway type of curve obtained at 650–850° C, the transition to a linear rate being the point at which the diffusion becomes slow and of little importance due to the build-up of oxygen in the centre of the pellet.

Work by Livey and Murray²⁾ using hot pressed $\text{UO}_{2.13}$ of bulk density 10 g/cc showed a peak rate of 160 mg/cm² h at 700° C compared with 52 mg/cm² h at 500° C in the present work. The difference is most likely due to differences in the method of manufacture or density of the compacts. Diffusion of oxygen would occur more readily into the lower density material and internal oxidation would be expected to break-up the pellet and expose a greater surface area to the gas.

TABLE 1

Rates of attack after 30% of the theoretical amount of oxygen had reacted

Temperature (° C)	Rate † (mg/cm ² h)
350	14
400	22.5
450	51.0
500	51.7
550	47.3
600	40.7
650	33.5
700	27.7
750	36.0
800	16.8
850	21.0
900	≈ 4.0

† The rates are expressed as weight gain per unit of geometric surface area per unit of time (mg/cm²h).

References

- ¹⁾ S. Aronson *et al.*, J. Chem. Phys. **27** (1957) 137
- ²⁾ D. T. Livey and P. Murray, Progress in Nuclear Energy, Series V, **1** (Pergamon Press, 1956) 473

BOOK REVIEW

COLLOQUE SUR LA DIFFUSION A L'ETAT SOLIDE.
(SYMPOSIUM ON SOLID STATE DIFFUSION)
(Saclay 3, 4, 5 juillet 1958). (Centre d'Etudes
Nucléaires de Saclay—North-Holland Publish-
ing Cy, Amsterdam. iv+178 p. Guilders 30).

This book is a collection of the twenty-one papers read at a conference at the "Centre d'Etudes Nucléaires de Saclay" in July 1958. Its scope is less wide than the title suggests, since all the articles are concerned with diffusion in metals, with a strong emphasis on the problems of intermetallic chemical diffusion and the diffusion of gases in metals. Both of these problems have considerable application in present day technical metallurgy, particularly in the field of reactor technology where metal components are required to operate at high temperatures and under the influence of damaging radiations. Our understanding of diffusion in metals has as yet reached a stage at which only rather idealised cases such as self-diffusion in pure metals, the effects of impurities at vanishingly small concentration on self-diffusion, and the diffusion of impurities at similar concentrations in a pure solvent metal can be treated theoretically with much success. Diffusion in alloys and more complex systems involving concentration gradients and phase boundaries is considerably less well understood. Experimental work on such systems is therefore necessary not only to provide the empirical knowledge for special applications but also to further our general understanding of diffusion processes.

The book will perhaps be of greatest value to those concerned with the technical aspects of diffusion in metals, but readers more interested in the purely physical aspect of the subject will find a number of topics of fundamental importance included. The first paper, for example, illustrates the phenomenological approach to the problem of diffusion in a concentration gradient and shows that some measure of agreement can be obtained between calculation and experiment regarding the mean displacements of atoms in chemical diffusion.

A group of articles follow in which many of the methods now used for analysing diffusion zones are described and illustrated by reference to particular experimental work. These methods include a variety of radioactive tracer techniques, micro-hardness measurements and a method applied to α -brass depending on the rates

of evaporation and condensation of zinc. In addition two articles deal with the observation of atomic migration over short distances. The clustering of dissolved atoms into zones with linear dimensions of the order of 50 Å when certain alloys are cold-worked is examined as a diffusion process and diffusion coefficients evaluated from X-ray analysis of the zones. Electron diffraction studies allow the interdiffusion of metals in thin evaporated films to be followed at temperatures very much lower than those required for more conventional macroscopic diffusion experiments. With these methods it becomes possible to observe the effects of quenched-in defects, and the results are of interest not only from the point of view of establishing a mechanism for the diffusion process, but also for the information they may provide on the physical metallurgy of the systems studied.

The behaviour of the inert gases in metals is of particular importance in reactor technology since these elements are formed within fuel elements as fission products, and their subsequent behaviour may seriously affect the mechanical properties of these components, quite apart from the danger of the escape of radioactive gases. The inclusion of a number of papers in the conference on the solubility and diffusion of inert gases in metals is therefore very appropriate. A second gas diffusion problem arises in reactors because of the need to prevent the oxidation of uranium and other structural metals. The diffusion of oxygen through protective envelopes, together with the efficiency of methods available for enveloping or "canning", and interdiffusion between the metal requiring protection and the envelope, are accordingly the subjects of further articles.

The book is beautifully produced, with excellent reproduction of metallographs, electron micrographs and photographs; it is a pity that some of them are without legends. Graphs and drawings are clearly reproduced on a generous scale, a feature which adds to the pleasure of reading the book. There are few typographical errors, though a notable one occurs on page 33 where the diffusion coefficient has been placed on the wrong side of Fick's equation, one of the basic equations in diffusion theory. It is curious that the term "three dimensional diffusion" has been used consistently as a translation of "diffusion en volume".

D. H. TOMLIN